

Development of Nanowire Surface Fastener for Room-Temperature Electrical Bonding

Peng WANG

Contents

Contents.....	I
1. Introduction	1
1.1 Surface mount technology (SMT).....	1
1.1.1 Brief history of SMT.....	1
1.1.2 Pb-Sn solders.....	2
1.1.3 Pb-free solders.....	3
1.1.4 Challenge of SMT.....	4
1.2 Biomimetic adhesives.....	5
1.2.1 Gecko toe pads.....	5
1.2.2 Biomimetic adhesives.....	7
1.3 Contents of this research.....	14
1.4 Organization of this dissertation.....	16
2. Room-Temperature Bonding Technique Based on Copper Nanowire Surface Fastener	26
2.1 Introduction.....	26
2.2 Experimental section.....	26
2.2.1 Anodized aluminum oxide template.....	26
2.2.2 Pattern design and fabrication.....	30
2.2.3 Template-assisted electrodeposition.....	32
2.2.4 Testing of adhesive strength and electrical resistance.....	35
2.3 Experimental results.....	36
2.4 Van der Waals force theory.....	46
2.4.1 Hamaker constant.....	47
2.4.2 Van der Waals expressions.....	47
2.5 Theory analysis of Cu nanowire surface fastener.....	49
2.6 The perfect states of copper interconnection.....	50
2.6.1 The determination of adhesive strength.....	50
2.6.2 The determination of electrical resistance.....	53
2.7 Tilted copper nanowire surface fastener.....	57
2.8 Summary.....	62
3. Copper-parylene Core-shell Nanowire Surface Fastener Used for Room-Temperature Electrical Bonding	68
3.1 Introduction.....	68

Contents

3.2 Experimental section	68
3.2.1 Pattern design and fabrication	68
3.2.2 Polycarbonate template	69
3.2.3 Electrodeposition of copper nanowire.....	71
3.2.4 Parylene conformal coating.....	74
3.2.5 The electrical testing of thin parylene film.....	76
3.2.6 Testing of adhesive strength and electrical resistance	77
3.3 Experimental results	77
3.3.1 The performance of thin parylene film.....	77
3.3.2 The performance of copper-parylene core-shell NSF.....	82
3.4 Theory analysis.....	94
3.4.1 Calculation of Hamaker constant	94
3.4.2 The van der Waals force between two core-shell nanowires	95
3.4.3 Determination of maximum adhesive strength.....	101
3.5 Summary	103
4. Copper-polystyrene Core-shell Nanowire Surface Fastener	107
4.1 Introduction	107
4.2 Polystyrene chemical bonding	108
4.3 Template wetting method	109
4.4 Copper-polystyrene core-shell nanowire array	110
4.4.1 Anodize alumina oxide template	112
4.4.2 Surface modification of the substrate	113
4.4.3 The formation of PS nanotube in AAO template	114
4.4.4 Electrodeposition of Cu nanowires	115
4.5 SEM image of copper-polystyrene core-shell nanowire.....	116
4.6 Adhesive strength measurement	117
4.7 Electrical resistance measurement.....	119
4.8 Summary	120
5. Conclusions	124
Acknowledgements.....	128

1. Introduction

1.1 Surface mount technology (SMT)

1.1.1 Brief history of SMT

Compared with conventional insertion assembly in which the leads of electrical package are inserted into holes of the print wiring board (PWB), surface mount technology (SMT) leads to smaller components, much higher component density and faster assembly. SMT is composed of three main processes: applying solder paste, placing chip components and reflow soldering. Reflow soldering involves heating and cooling the assembly of board plus components held by solder paste through successively high temperature and it is the core process of SMT.

During the reflow soldering process, both heating and cooling steps are crucial for the final result (**Fig. 1-1**). The heating mainly affects the function of the flux, the solder melting, metallurgical properties, and void formation, while the cooling is deemed to be mainly responsible for the evolution of the solder microstructure [1, 2]. Moreover, the circuit boards and the placed components are often subjected to reflow soldering in many times in the electronics assembly line, which also affects the properties of solder joint [1]. The whole electronics assembly will be heated during the reflow soldering and then all parts have to withstand high temperature heating, which is not good to temperature-sensitive components. Many methods have been applied to achieve uniform heating which can reduce possible danger of thermal shock caused by non-uniform heating. However, the heating temperature applied on the lower side of the assembly is still lower than that applied on the upper side because main heaters are usually placed on the top side of the conveyor.

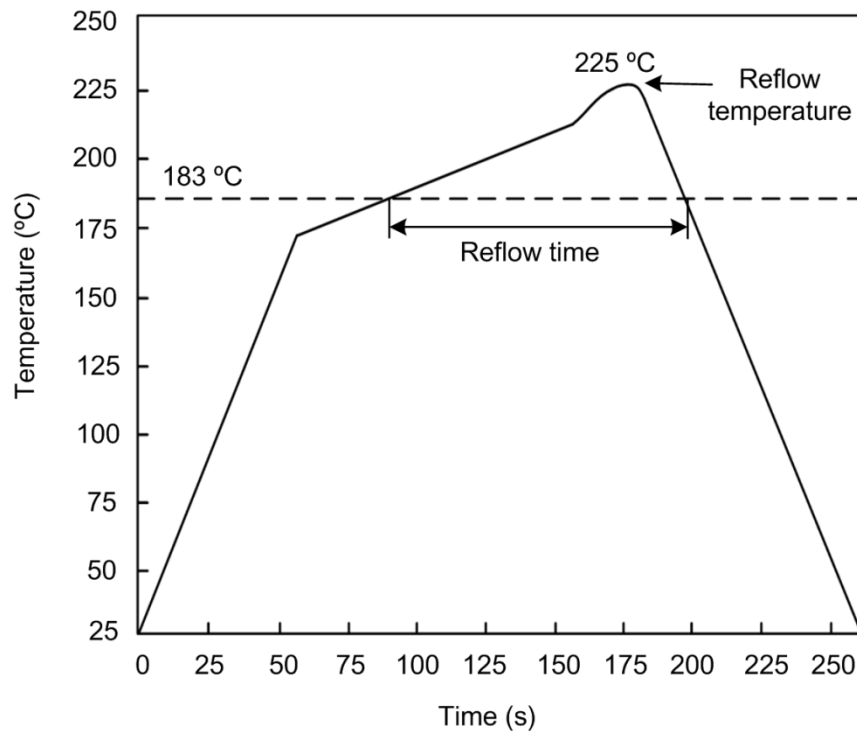


Fig. 1-1 A simplified time-temperature profile during reflow soldering [2].

1.1.2 Pb-Sn solders

Soldering technology plays a crucial role in almost all the levels of electronic packaging, such as flip-chip connection, solder-ball connection in ball-grid-arrays (BGA), or IC package assembly to a PWB. In SMT soldering, solder paste is placed on the PWB by screen printing. Solder paste is mainly composed of fine solder powder and flux. The characteristics of solder paste in relation to soldering and solder joint reliability have been extensively studied [3]. During the reflow process, solder particles are first melted. Then, the flux is activated. Third, the solvent materials are evaporated, and the molten solder coalesces simultaneously. Finally, the solder is solidified at the process of cooling. Pb-Sn solders have been widely used in different levels of the electronic assembly, where strict electrical, mechanical and thermal properties of solder alloys are essential [4]. Pb-Sn solders exhibit many merits, like low melting temperatures, good workability, ductility, ease of handling and excellent

Chapter 1. Introduction

wetting on Cu and its alloys [4]. Particularly, the Pb–Sn eutectic solder with a composition of 62wt% Sn and 38wt% Pb has a melting point of 183 °C and it is compatible with most substrates and components [5]. Pb, the main component of eutectic solders, has many technical advantages such as: (1) Pb can reduce the surface tension of pure tin and then facilitates wetting [6]. (2) Pb helps to prevent the transformation of beta (β) Sn to alpha (α) Sn, and then reduces the structural integrity of the Sn [7]. (3) Pb is a low cost and readily available metal [4]. The above-mentioned factors make Pb an ideal alloying element with Sn. However, the toxicity of traditional Sn-Pb solder has led to a trend of worldwide legislation that mandates the removal of Pb from electronics. The Waste Electrical and Electronic Equipment (WEEE), Restriction of Hazardous Substances (RoHs), and European Commission's (EC) draft directives have approved banning the use of Pb in electronics effective in July 2006 in European Union countries [8, 9].

1.1.3 Pb-free solders

Due to the excellent performance of Pb-Sn solders such as ease of manufacturing, finding suitable alternatives is a challenging issue. The Pb-free alternatives should not only meet environment, health and safety requirements, but also fulfills solder joint reliability and performance expectations [4]. The Pb-free solder should be comparable to or superior to Pb-Sn solders in order to guarantee its manufacturability, reliability, and overall usefulness in modern electronics assembly lines and products [1].

The melting point of the solder alloys is a very important factor [10]. Most current components are designed for Pb-Sn processes and their thermal endurance is limited [1]. Moreover, too high process temperatures may damage the board. Hence, the melting point of the Pb-free solder alloy should be close to that of Pb-Sn solder

[11]. The alloy should preferably be binary or ternary [5]. Alloys consisting of more than three metals tend to be more difficult to control. Sn remains a base element in most current lead-free alloy [12]. Lastly, the solder alloy should be used in a wide range of application, such as a paste, wire, or a bar.

1.1.4 Challenge of SMT

Recently, with the development of micro-/nano-systems technologies, the size of electrical components is shrinking continuously and then leads to an increase in the number of input/output terminals [13]. Hence, the numbers of solder joints per package are continuously increasing while the dimensions of the solder joints are decreasing (Fig. 1-2).

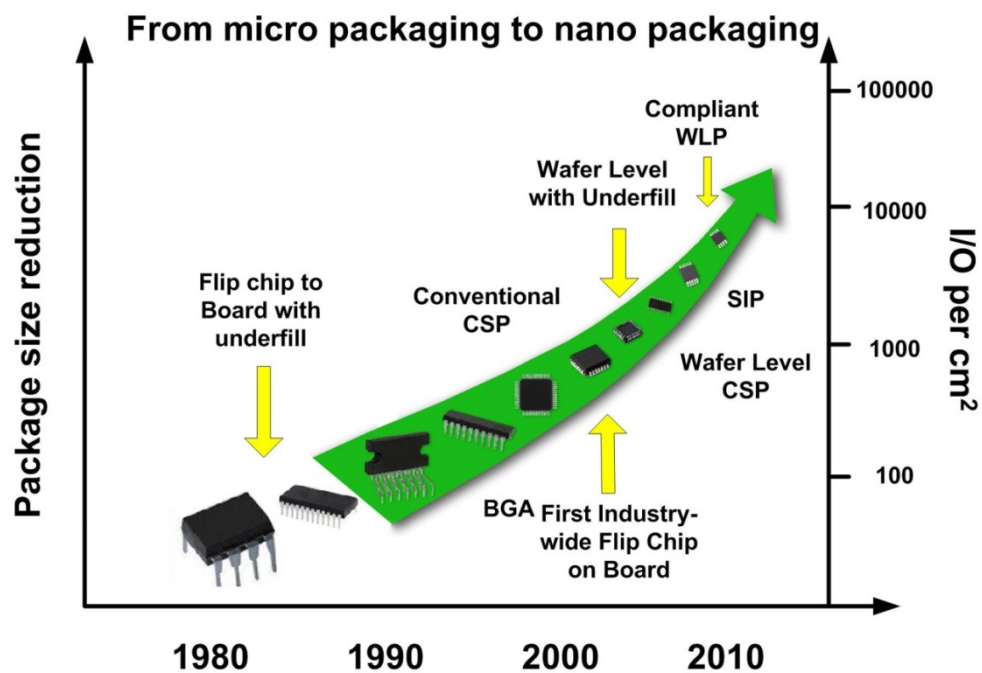


Fig. 1-2 The trend from micro packaging to nano packaging [4].

However, as the solders are miniaturized to small scales, a number of shortcomings (such as low bonding strength, fabrication challenges, and the lack of reliability) are presented that limit their successful application. In addition, the

recycling of rare metals in the surface mount components and the printed circuit boards is not easy due to the difficulties in detaching the components, circuit boards and solder materials. Therefore, there is an increasingly urgent need for a nontoxic, reusable and low-temperature bonding technique with good mechanical and electrical properties simultaneously, especially for micro/nano electronic circuits and flexible electronic devices.

1.2 Biomimetic adhesives

1.2.1 Gecko toe pads

The unusual ability of gecko lizards to climb on any vertical surface and hang from a ceiling with toe pads has inspired scientific research for decades [14]. As can be seen in **Fig. 1-3**, gecko toe pad has a hierarchically structure from macro- down to nano- levels [15, 16]. Microscopy has shown that a gecko's foot possesses nearly five hundred thousand keratinous hairs or setae [14]. Each seta has a length of 30-130 μm and a diameter of $\sim 5 \mu\text{m}$ (**Fig. 1-3**). Each single seta further branches out at the tip and splits into hundreds of nanohairs named spatulae (**Fig. 1-4**), which function as the ultimate contacting elements. These terminals are tapered spatula pads, $\sim 200 \text{ nm}$ wide and 5-10 nm thick [17].

After applying a proper preload, a single seta shows maximum adhesive forces of $\sim 200 \mu\text{N}$ in shear and $\sim 20 \mu\text{N}$ in normal directions against a clean and smooth glass substrate [14]. Normal pull-off force of $\sim 10 \text{ nN}$ was also obtained for an individual spatulae by using atomic force microscopy (AFM) [18]. The researchers further found that a single foot of geckos could generate an adhesive force of $\sim 100 \text{ N}$,

Chapter 1. Introduction

which could support ~ 10 times of their averaged body weight [19]. However, it should be noted that these good experiment results were obtained from rather idealistic substratum (e.g. glass or silicon wafers) and static measurements, and the adhesive force of gecko toe pad tended to fall drastically when the geckos are set free in their natural environments and in motion [20-23]. Van der Waals interaction has been proven to be the main reason for this phenomenon [24]. On the other hand, some evidences show that humidity also has a strong effect of altering the measured forces [25, 26]. Recently, based on experimental evidences and theoretical analysis, the researchers found that the change of humidity tended to lead the change of material property (Young's modulus), which would further affect the adhesive strength of gecko toe pad [27-29].

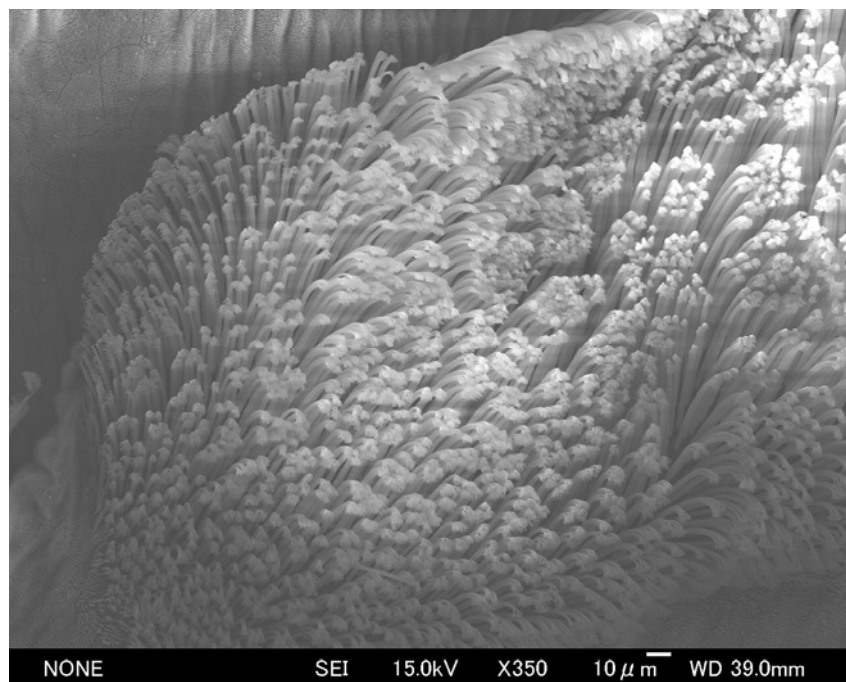


Fig. 1-3 Side view SEM image of setal array in Gecko toe pads.

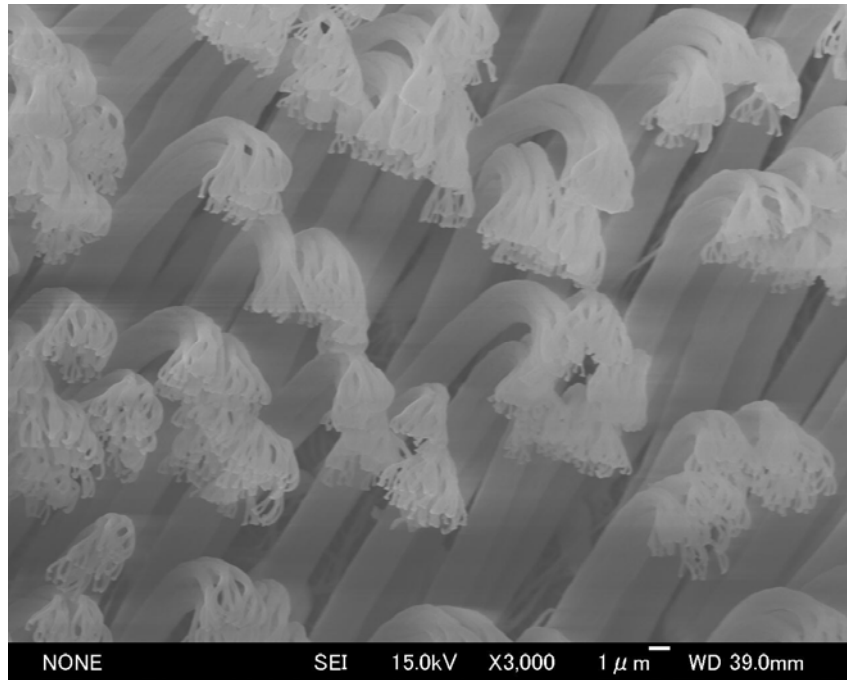


Fig. 1-4 SEM image of the finest terminal branches of seta.

1.2.2 Biomimetic adhesives

Many researches have been carried out to fabricate biomimetic gecko toe pads. Template method and gas phase growth method are the two widely used techniques. Following discussion will give a description of these two techniques in more detail and then make a summarization.

1.2.2.1 Template method

1.2.2.1.1 Aluminum anodic oxide (AAO) template

AAO template can be prepared by the well-known two-step anodization process and it has hexagonally distributed straight nanopores. The diameter, interpore distance, and the thickness of AAO template could be adjusted by changing the anodization parameters. AAO template has been widely used to fabricate nanowire array and some researchers tried to apply it to biomimetic the gecko's foot. Cho et al. [30] used the AAO templates to fabricate polydimethylsiloxane (PDMS) nanowires. After

Chapter 1. Introduction

carefully peeling off, the nanowire structured PDMS exhibited super hydrophobicity. Chen et al. [31] created free standing high aspect ratio polymethyl methacrylate (PMMA) nanopillars by capillary driven AAO template molding method and PMMA nanotubes by AAO template wetting method. Kim et al. [32] invented a UV nano embossing machine which can be used to fabricate the high aspect ratio nanopillar arrays of UV curable polymer resin. Moreover, this embossing machine has the advantage of time efficiency. Kunstandi et al. [33] fabricated high aspect ratio freestanding PMMA nanowires with a two-level hierarchy structure. An AAO template was selectively etched out by photolithography method to form micro-channels and another thin AAO membrane was prepared by two-step anodization process to form nanopores. Then the two membrane was bonded together to form hierarchy structure. Another method to fabricate hierarchy AAO template was adopted by Ho et al. [34] through sequentially stepping down the anodization potential. They further used the hierarchy template to fabricate polycarbonate (PC) nanowire arrays which shows the macroscopic adhesive strength of 6.5 N/cm^2 .

However, the aforementioned polymer nanowire or nanotube arrays are nonconductive so that they are hard to be applied into room-temperature bonding. Metal nanowires, which exhibit excellent electrical properties, can also be fabricated with the help of AAO template. Many works have tried to apply a metal nanowire into the electrical bonding technology in microelectronics, but it seemed that no adhesive strength was obtained [35-38]. Ju et al. [39] presented a room-temperature technique based on Au nanowire array, which shows a macroscopic adhesive strength of $\sim 5 \text{ N/cm}^2$ and an electrical resistance of $\sim 6.28 \times 10^{-2} \Omega \cdot \text{cm}^2$. However, compared with those of traditional electrical bonding technologies, the mechanical and electrical properties of this new bonding technique still needed improvement.

1.2.2.1.2 Polycarbonate template

Radiation track-etched PC membranes are another kind of widely used template. PC membranes are made by bombarding a nonporous polycarbonate sheet, typically 6 to 20 μm in thickness, with nuclear fission fragments to create damage tracks, and then chemically etching these tracks into pores [40]. In these radiation track etched membranes, pores have a uniform size as small as 10 nm, but they are randomly distributed. Pore densities can be as high as 10^9 pore/ cm^2 [41].

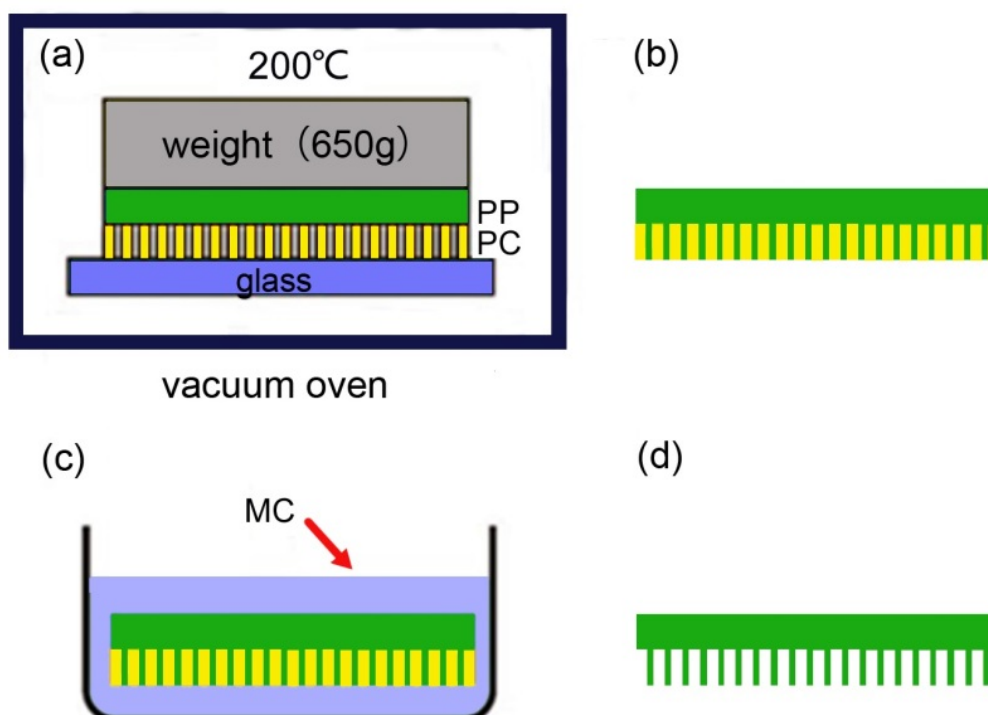


Fig. 1-5 Schematic illustration of the fabrication process of PP fibrillar adhesives [44].

Many kinds of polymer (e.g. polypropylene (PP) and polyethylene) nanorod array can be obtained through PC template [42, 43]. As shown in **Fig. 1-5**, the nanorod array was fabricated by casting a single layer of polymer film in a vacuum oven into a PC membrane filter containing nanopores. Samples were molded in a

Chapter 1. Introduction

hydraulic press at 171 °C for 300 s and allowed to cool for 45 min before being released. The PC filter was then etched in methylene chloride (MC) to release the molded fibers. The resulting samples were rinsed in isopropyl alcohol and air dried [42]. The fabricated stiff polymer nanowire array not only demonstrates high adhesive strengths but also shows self-cleaning properties with microspheres (radius $\leq 2.5 \mu\text{m}$) [44].

1.2.2.1.3 Etched silicon master

Although AAO and PC template have the advantage of cost-efficiency and easy fabrication, regularly ordered nanoholes in large area are still a challenge for them. On the other hand, a silicon master consists of regularly order nanoholes was proposed by K. Suh et al. [45, 46]. Polyurethane (PU) or polyurethane acrylate (PUA) was chosen as the replica mold over SU-8 or PDMS, since it offers not only better mechanical strength, flexibility and stability, but also small shrinkage and UV light transmittance [45]. The master mold with nanoholes could be prepared by photolithography and subsequent reactive ion etching. The surface of the master was treated with a self-assembled monolayer (SAM) of (tridecafluoro-1,1,2,2-tetrahydro-ctyl) trichlorosilane [$\text{CF}_3(\text{CF}_2)_5\text{CH}_2\text{CH}_2\text{SiCl}_3$] (FOTCS) for easy release of replicated polymer structures from the master. Then, a small amount of PU or PUA (~5ml) was drop-dispensed onto the master and a flexible poly ethylene teraphthalate (PET) film (~50 μm thickness) was lightly pressed against the liquid drop for it to be used as a supporting backplane. After preparing a polymer replica by UV exposure and moldremoval, the replicated PU or PUA was additionally exposed to UV for 10 h to remove trapped polymer radicals and any remaining solvent or unsaturated prepolymer. Regularly ordered micro- or nanohairs array with different radius and aspect ratio could be obtained from this kind of silicon master.

1.2.2.2 Gas phase growth method

1.2.2.2.1 Carbon nanotube based dry adhesives

Carbon nanotube arrays have been widely studied for the application of mimicking gecko toe pad structures to achieve high adhesive, mainly because of the extremely high aspect ratio and the exceptional mechanical properties. Vertically aligned carbon nanotubes (VA-CNTs) arrays are usually grown on silicon substrates through chemical vapor deposition (CVD) process by flowing a mixture gases of Ar, H₂ and C₂H₂ under high temperature ($> 500\text{ }^{\circ}\text{C}$), just as shown in **Fig. 1-6**.

Fig. 1-7 shows the SEM image of CNT array grown under the following conditions: H₂=50 sccm, C₂H₂=100 sccm and $\sim 750\text{ }^{\circ}\text{C}$. Here sccm is a flow measurement term which refers to standard cubic centimeters per minute. The length of the VA-CNTs can be controlled by the CVD time, the packing density can be controlled by the gas composition and the heating temperature [19].

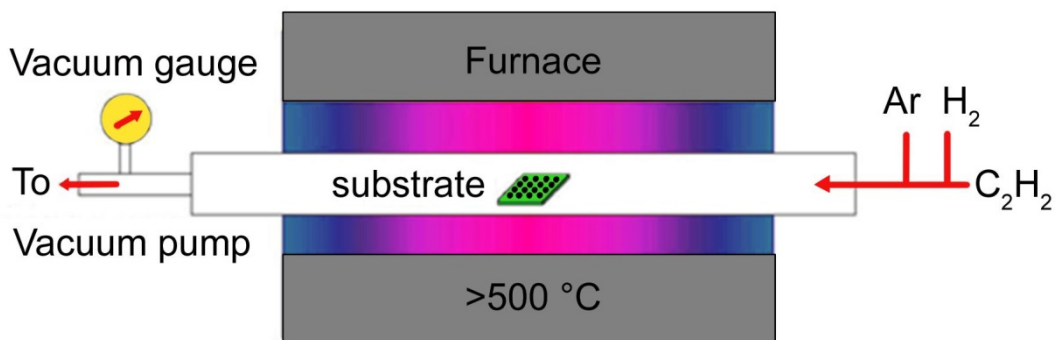


Fig. 1-6 A schematic diagram of the CVD system for the growth of CNT arrays.

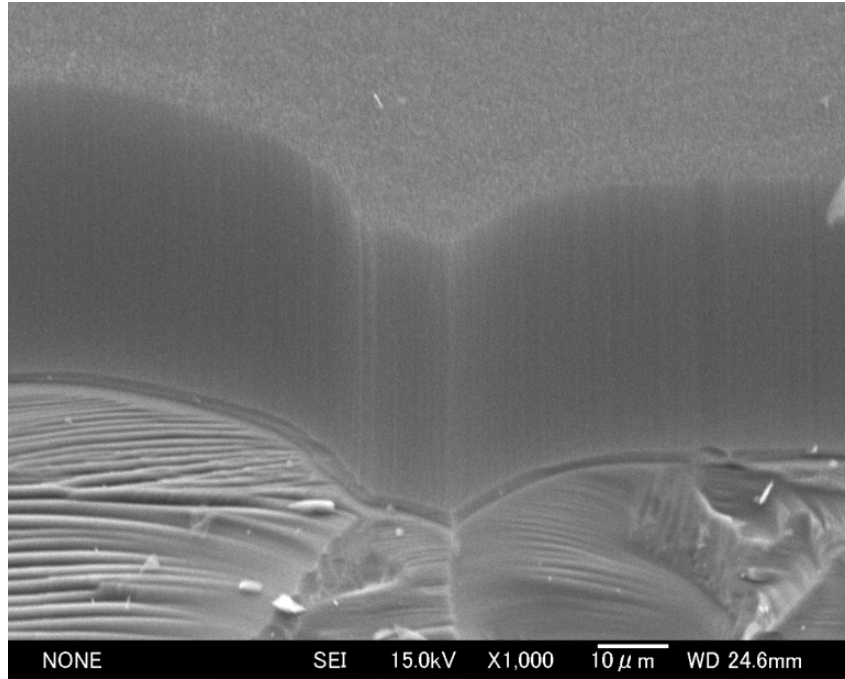


Fig. 1-7 SEM image of CNT array.

Zhao et al. [47] synthesized high aspect ratio multi-walled CNT arrays, and tested the according macroscopic adhesive properties. 5-10 μm height CNT arrays exhibit a normal adhesive strength of 11.7 N/cm^2 and a shear strength of 7.8 N/cm^2 under $\sim 2 \text{ kg}$ weight of preload. Ge et al. [48] created vertically aligned patterned multi-walled CNT arrays on flexible 3M Scotch tapes which show a shear adhesive strength for a 36 N/cm^2 under a preload of $25\text{-}50 \text{ N/cm}^2$. In that experiment, photolithography was utilized to define different square patterns, $50\text{-}500 \mu\text{m}$ in width. Then vertically aligned multi-walled CNT arrays with curly entangled end segments at the top were synthesized by Qu et al. [49] through a low-pressure CVD process. Under shear adhesive strength testing, the sidewall contact between the entangled segment and the target surface led to high adhesive strength of $\sim 100 \text{ N/cm}^2$. On the other hand, normal pulling led to the peeling of each entangled tip at the interface which reduced the normal adhesive strength to $\sim 10 \text{ N/cm}^2$. However, electrical connection was not realized or reported in the aforementioned CNT arrays. Qu et al.

[50] fabricated high quality vertically aligned single-walled CNT arrays via plasma enhanced CVD method, which show a macroscopic adhesive strength of 29 N/cm^2 and a electrical resistance of $\sim 12.8 \text{ } \Omega \cdot \text{cm}^2$. Tong et al. [51] tested the performance of interconnected CNT and carbon nanofiber arrays, which exhibits a macroscopic adhesive strength of $4.38 \times 10^{-2} \text{ N/cm}^2$ and a electrical resistance of $1.6 \text{ } \Omega \cdot \text{cm}^2$. Park et al. [52] measured the electrical resistance of multi-walled CNT arrays under continuous preload, and a electrical resistance of $\sim 1.24 \times 10^{-2} \text{ } \Omega \cdot \text{cm}^2$ was obtained.

1.2.2.2.2 Ge nanowire based dry adhesives

Because Ge and C are groupelement, Ge nanowires can also be synthsize by the CVD method. The detailed synthesize process is similar with that of CNTs and can be found in literature [53]. Briefly, Ge nanowires can be grown at $280 \text{ }^\circ\text{C}$ and 45 torr using germane (12 sccm , 10% balanced in H_2) as the precursor gas. Although pristine Ge nanowires can only generate a weak adhesive strength of 0.8 N/cm^2 , Ko et al. [53] further found that the adhesive strength would be drastically enhanced by the application of the parylene coating. Because of the high surface compliance of the parylene shell, the Ge-parylene core-shell forests could generate a maximum adhesive strength of $\sim 163 \text{ N/cm}^2$. Kapadia et al. [54] further sputtered a thin film of Ag onto the Ge-parylene core-shell nanowire forests, and then applied it into electrical connector. The Ge-parylene-Ag core-multishell nanowire forests could generate a macroscopic adhesive strength of $\sim 30 \text{ N/cm}^2$ and a electrical resistance of $\sim 6.25 \text{ } \Omega \cdot \text{cm}^2$ [54].

1.2.2.3 Comparison of biomimetic adhesives and traditional solders

A comparison of typically biomimetic adhesives and traditional solders is made in **Table 1.1**, where NW is the abbreviation of nanowire. As can be seen in **Table**

Chapter 1. Introduction

1.1, the traditional solders still show better performance than the biomimetic adhesives. Hence, to achieve high adhesive strength and low electrical resistance at the same time to replace the traditional solder is still a challenge, which will be the research goal of this study.

Table 1.1 Comparison of biomimetic adhesives and traditional solders.

Material	Shear adhesive strength (N/cm ²)	Normal adhesive strength (N/cm ²)	Electrical resistance ($\Omega \cdot \text{cm}^2$)
PC NWs [34]	6.5	NA	NA
PP NWs [43]	1		NA
PUA NWs [46]	40		NA
CNTs [49]	~100	~10	
CNTs and CNFs [51]		4.38×10^{-2}	1.6
CNTs [50]	15	29	~12.8
CNTs [52]			$\sim 1.24 \times 10^{-2}$
Ge/parylene NWs [53]	163		NA
Ge/parylene/Ag NWs [54]	30		~6.25
Ni NWs [37]			6×10^{-5}
Cu NWs [38]			$\sim 2.75 \times 10^{-5}$
Au NWs [39]	5.5	5	6.28×10^{-2}
Pb-Sn solder	1000-5000 [55]	2000-6000 [55]	$\sim 1.28 \times 10^{-7}$ [56]
Pb-free solder	1000-4000 [57]	3000-4000 [58]	$\sim 15.6-62.5 \times 10^{-7}$ [57]

1.3 Contents of this research

The main objective of this work is to achieve room-temperature mechanical and electrical bonding through nanowire surface fastener.

The research contents of this dissertation are therefore:

Content #1: Fabrication of uniform nanowire array on the substrate directly.

The template-assisted electrodeposition method would be used to fabricate copper nanowire array. However, some challenges for this method still existed because it was

Chapter 1. Introduction

difficult to fabricate freestanding nanowire array on the substrate directly. Traditionally, a thin conductive metallic layer was deposited on one side of the template through sputter or electron-beam evaporation, which is difficult to get free-standing nanowire array after the template is fully removed. Moreover, there is an urgent need to fabricate copper nanowire array on the substrate directly so that it can be used for the application of microelectronics. Here, some experimental modifications would be investigated to achieve this project goal. Effect of various parameters would be investigated to understand how they affect the nanowire growth.

Content #2: Development of Copper-polymer core-shell nanowire surface fastener. The copper exhibits good electrical properties but low adhesive strength. The polymer exhibits good adhesive strength but poor electrical properties. Copper-polymer core-shell nanowire surface fastener would show a possibility that the core-shell nanowire surface fastener has the advantage of copper and polymer at the same time. The method to fabricate core-shell nanowire structure would be investigated. Copper-parylene core-shell nanowire surface fastener would be fabricated based on the unique properties of parylene which can be conformal coated on the various kinds of substrates. Copper-polystyrene core-shell nanowire surface fastener would also be fabricated based on the unique properties of polystyrene which can form nanotube in the AAO templates.

Content #3: Analysis of adhesive mechanism. The mechanism why the interconnected nanowire arrays generated adhesive strength would be further investigated by the observation of interconnected copper nanowires at nanoscale. Recently, many works have been done to study the mechanism of nanoscale adhesive and the van der Waals force theory has been shown to be a good method to explain such a phenomenon [46, 49]. By understanding the mechanism, the optimization of

Chapter 1. Introduction

the nanowire surface fastener would be given so that its performance could be further improved.

Content #4: Estimate of maximum adhesive strength. Besides van der Waals forces, there are several other factors which may affect the adhesive strength of the nanowire surface fastener, such as interfacial shear strength of polymer shell, tensile strength of polymer and adhesive strength of nanowire tearing at the base from the substrate. Here, the maximum adhesive strength of the nanowire surface fastener would be estimated by the limit forces of them, which may cast light on the further research. In this study, only the room-temperature or relative low temperature was considered. For working at high temperature, the creep of Cu nanowires and the dissolution of polystyrene or polystyrene nanoshells should be studied.

Content #5: Estimate of electrical properties of nanowire surface fastener. The transmission line model would be used to determine both the contact resistance and copper resistance. Through this model, the specific contact resistance together with the copper resistance would be determined, and then the smallest electrical resistance of nanowire surface fastener could be estimated.

1.4 Organization of this dissertation

The main text of this dissertation is organized into five chapters, as follow:

Chapter 1 is a general introduction of the research background, current research challenge, and research goals and contents.

In chapter 2, a room-temperature bonding technique based on copper nanowire surface fastener was presented. Two additional immersion methods were introduced, and then the freestanding copper nanowire array could be fabricated on the substrate directly with the help of rigid aluminum anodic oxide (AAO) template. Although the

Chapter 1. Introduction

two additional immersions were quite easy, these innovative processes were found to be crucial to achieve uniform contact in the experimental process. SEM observation shows that a copper nanowire array was fabricated in the entire fastener area and the fabricated copper nanowire array had uniform length in most areas. TEM images further show that the copper nanowire was single-crystalline. This room-temperature bonding technique was realized through pressing two copper nanowire arrays against each other. The van der Waals forces between the interconnected nanowires contributed to the room-temperature bonding. The copper nanowire surface fastener exhibited a macroscopic adhesive strength of 8.17 N/cm^2 and an electrical resistance of $0.69 \times 10^{-2} \Omega \cdot \text{cm}^2$. Furthermore, by observing the SEM images of interconnected nanowire arrays, the upper and lower nanowire arrays were found to be interconnected at an arbitrary angle. Here, the adhesive strength was estimated from two extreme conditions (parallel-contacting mode and perpendicular-contacting mode), and the estimated value showed that a much higher adhesive strength can be obtained if most copper nanowires could interconnect with each other. Furthermore, the adhesive strength and electrical resistance of the nanowire surface fastener in the perfect states were predicted and the predicted values show similar orders with those of traditional solders. Moreover, tilted copper nanowire array could be obtained through applying directional shear force onto the freestanding copper nanowire array. In terms of pressing the straight copper nanowire array against the tilted array, the van der Waals forces between the interconnected nanowires contributed to electrical bonding. This tilted nanowire surface fastener exhibited low electrical resistance ($\sim 0.94 \times 10^{-2} \Omega \cdot \text{cm}^2$). In addition, anisotropic adhesive properties were obtained, and the shear adhesive strengths were 9.36 and 1.56 N/cm^2 , respectively, for the two

Chapter 1. Introduction

opposite directions that are parallel and antiparallel to the tilted direction of the nanowires.

In chapter 3, a room-temperature electrical surface fastener based on copper-parylene core-shell nanowire arrays were presented. The van der Waals forces between the two sets of identical core-shell nanowire arrays led to strong adhesive strength. Interestingly, the thin parylene film was found to be conductive as the thickness shrunk to nanoscale. Here, a new cell for electrodeposition was adopted so that copper nanowires from polycarbonate template could grow on substrate directly. The porous glass plate and a peculiar cell was introduced to achieve the uniform contact between the flexible polycarbonate membrane and the substrate. After coating a thin parylene film on the copper nanowires, this electrical surface fastener exhibited an adhesive strength of $\sim 25 \text{ N/cm}^2$ and an electrical resistance of $\sim 4.22 \times 10^{-2} \Omega \cdot \text{cm}^2$. In addition, a new model based on the assumption of additivity was developed to analyze the van der Waals forces between the core-shell nanowires, which can explain the adhesive mechanisms of core-shell nanowire surface fasteners.

In chapter 4, an innovative fabrication method to fabricate core-shell nanowire array was described in detail. At first, PS nanotube array was formed within the AAO nanochannels through spin-casting method. Second, copper nanowires were fabricated into PS nanotubes through template-assisted electrodeposition method. Finally, after the fabrication of copper-polystyrene core-shell nanowire array on the Au/Cr/glass substrate, selective etching was carried out to remove the AAO template. In addition, polystyrene shows viscosity after the treatment of volatile toluene solution. Based on this phenomenon, a new kind of surface nanowire fastener consisting of copper-polystyrene core-shell nanowire array was prepared. This kind of copper-polystyrene nanowire fastener showed adhesive strength of $\sim 23.52 \text{ N/cm}^2$ (in

Chapter 1. Introduction

normal direction) and $\sim 47.04 \text{ N/cm}^2$ (in shear direction). Four-point probe electrical measurement showed that the electrical resistance of the interconnected nanowire array on the fastener is $\sim 0.78 \times 10^{-2} \Omega \cdot \text{cm}^2$ under the preload of $\sim 9.8 \text{ N}$.

Finally, the conclusions of this thesis are summarized and discussed in chapter 5.

REFERENCES:

1. S. Nurmi. Reliability of SnAgCu Solder Joints under Thermo-Mechanical Stress. Doctor Thesis, Tampere University of Technology **2005**, 4-11.
2. C. E. Ho, Y. M. Chen, and C. R. Kao. Reaction kinetics of solder-balls with pads in BGA packages during reflow soldering. *J. Electron. Mater.* **1999**, 28, 1231-1237.
3. D. Reiff and E. Bradley. A novel mechanical shock test method to evaluate lead-free BGA solder joint reliability. Proc. 55th IEEE Electron. Compon. Technol. Conf. **2005**, 1519-1525.
4. P. Babaghorbani. Development of lead-free nanocomposite solders for electronic packaging. Master Thesis, National University of Singapore **2008**, 1-4.
5. T. B. Massalski. *Binary Alloy Phase Diagrams*, AMS International, Materials Park, OH, **1987**, 1st ed., 1847-1848.
6. P. Vianco, J. Rejent, and R. Grand. Development of Sn-based, low melting temperature Pb-free solder alloys. *Mater. Trans.* **2004**, 765-775.
7. R. E. Reed-Hill. *Physical Metallurgy Principles*, PWS Publishing Company, Massachusetts, **1994**, 287-311.
8. J. Cannis. Green IC packaging. *Adv. Packag.* **2001**, 8, 33-35.

Chapter 1. Introduction

9. Refer to website at <http://www.rohs.eu/english/index.html> for information on Restriction on use of certain Hazardous Substances (RoHS) regulations.
10. S. K. Kang and A. K. Sarkhel. Lead (Pb)-free solders for electronic packaging. *J. Electron. Mater.* **1994**, *23*, 701-707.
11. J. S. Hwang, Z. Guo, and H. Koenigsmann. A high-performance lead-free solder-the effects of In on 99.3Sn/0.7Cu. *Solder. Surf. Mount Technol.* **2001**, *13*, 7-13.
12. S. K. Kang et al.. Interfacial reaction studies on lead (Pb)-free solder alloys. *IEEE Trans. Electron. Packag. Manuf.* **2002**, *25*, 155-161.
13. M. Abtewa and G. Selvaduray. Lead-free solders in microelectronics. *Mater. Sci. Eng. R* **2000**, *27*, 95-141.
14. K. Autumn, et al.. Adhesive force of a single gecko foot-hair. *Nature* **2000**, *405*, 681-685.
15. K. Autumn. How gecko toes stick. *Am. Sci.* **2006**, *94*, 124-132.
16. H. J. Gao, X. Wang, H. M. Yao, S. Gorb, and E. Arzt. Mechanics of hierarchical adhesive structures of geckos. *Mech. Mater.* **2005**, *37*, 275-285.
17. B. N. J. Persson and S. Gorb. The effect of surface roughness on the adhesive of elastic plates with application to biological systems. *J. Chem. Phys.* **2003**, *119*, 11437.
18. G. Huber, S. N. Gorb, R. Spolenak, and E. Arzt. Resolving the nanoscale adhesive of individual gecko spatulae by atomic force microscopy. *Biol. Lett.* **2005**, *1*, 2-4.
19. S. Hu. Gecko and bio-inspired hierarchical fibrillar adhesive structures explored

Chapter 1. Introduction

- by multiscale modeling and simulation. Doctor Thesis, The University of Akron **2012**, 6-30.
20. B. Vanhooydonck, A. Andronescu, A. Herrel, and D. J. Irschick. Effects of substrate structure on speed and acceleration capacity in climbing geckos. *Biol. J. Linnean Soc.* **2005**, *85*, 385-393.
21. G. Huber, S. N. Gorb, N. Hosoda, R. Spolenak, and E. Arzt. Influence of surface roughness on gecko adhesive. *Acta Biomater.* **2007**, *3*, 607-610.
22. B. N. J. Persson. Biological adhesive for locomotion: basic principles. *J. Adhes. Sci.* **2007**, *21*, 1145-1173.
23. N. M. Pugno and E. Lepore. Observation of optimal gecko's adhesive on nanorough surfaces. *Biosystems* **2008**, *94*, 218-222.
24. K. Autumn, et al.. Evidence for van der Waals adhesive in gecko setae. *Proc. Natl. Acad. Sci. USA* **2002**, *99*, 12252-12256.
25. G. Huber, et al.. Evidence for capillarity contributions to gecko adhesive from single spatula nanomechanical measurements. *Proc. Natl. Acad. Sci. USA* **2005**, *102*, 16293-16296.
26. W. X. Sun, P. Neuzil, T. S. Kustandi, S. Oh, and V. D. Samper. The nature of the Gecko Lizard Adhesive Force. *Biophys. J.* **2005**, *89*, L14-L17.
27. J. B. Puthoff, M. S. Prowse, M. Wilkinson, K. Autumn. Changes in materials properties explain the effects of humidity on gecko adhesive. *J. Exp. Biol.* **2010**, *213*, 3699-3704.
28. M. S. Prowse, M. Wilkinson, J. B. Puthoff, G. Mayer, K. Autumn. Effects of

Chapter 1. Introduction

- humidity on the mechanical properties of gecko setae. *Acta Biomater.* **2011**, *7*, 733-738.
29. B. Chen, H. J. Gao. An alternative explanation of the effect of humidity in gecko adhesive: stiffness reduction enhances adhesive on a rough surface. *Int. J. Appl. Mech.* **2010**, *2*, 1-9.
30. W. K. Cho, and I. S. Choi. Fabrication of hairy polymeric films inspired by geckos: wetting and high adhesive properties. *Adv. Func. Mater.* **2008**, *18*, 1089-1096.
31. G. Chen, S. A. Soper, and R. L. McCarley. Free-standing, erect ultrahigh-aspect-ratio polymer nanopillar and nanotube ensembles. *Langmuir* **2007**, *23*, 11777-11781.
32. D. S. Kim, et al.. Replication of high-aspect-ratio nanopillar array for biomimetic gecko foot-hair prototype by UV nano embossing with anodic aluminum oxide mold. *Microsys. Technol.* **2007**, *13*, 601-606.
33. T. S. Kustandi, V. D. Samper, W. S. Ng, A. S. Chong, and H. Gao. Fabrication of a gecko-like hierarchical fibril array using a bonded porous alumina template. *J. Micromech. Microeng.* **2007**, *17*, N75-N81.
34. A. Y. Y. Ho, L. P. Yeo, Y. C. Lim, and I. Rodríguez, Fabrication and analysis of gecko-inspired hierarchical polymer nanosetae. *ACS Nano* **2011**, *5*, 1897-1906.
35. S. Fiedler, et al.. Evaluation of metallic nano-lawn structure for application in microelectronic packaging. Proc. IEEE Sys. Integr. Technol. Conf. **2006**, 886-891.
36. R. J. Lin, Y. Y. Hsu, Y. C. Chen, S. Y. Cheng, and R. H. Uang. Fabrication of nanowire anisotropic conductive film for ultra-fine pitch flip chip interconnection.

Chapter 1. Introduction

- Proc. IEEE Electron. Compon. Technol. Conf. **2005**, 66-70.
37. S. S. Baek and R. S. Fearing. Reducing contact resistance using compliant nickel nanowire arrays. *IEEE Trans. Compon. Packag. Technol.* **2008**, 3, 859-868.
38. J. Xu, K. M. Razeeb, S. K. Sitaraman, and A. Mathewson. The fabrication of ultra long metal nanowire bumps and their application as interconnects. Proc. IEEE Nano 2012 Conf. **2012**, 1-6.
39. Y. Ju, M. Amano and M. Chen. Mechanical and electrical cold bonding based on metallic nanowire surface fasteners. *Nanotechnology* **2012**, 23, 365202.
40. R. L. Fleisher, P. B. Price, and R. M. Walker. *Nuclear Tracks in Solids: principles and applications*, Berkeley University of California Press, **1975**, 23-25.
41. G. Cao and D. Liu. Template-based synthesis of nanorod, nanowire, and nanotube arrays. *Adv. Colloid Interface* **2008**, 136, 45-64.
42. A. G. Gillies and R. S. Fearing. Shear Adhesive Strength of Thermoplastic Gecko-Inspired Synthetic Adhesive Exceeds Material Limits. *Langmuir* **2011**, 27, 11278-11281.
43. J. Lee, C. Majidi, B. Schubert, and R. S. Fearing, Sliding-induced adhesive of stiff polymer microfiber arrays. I. Macroscale behavior. *J.R. Soc.Interface* **2008**, 5, 835-844.
44. J. Lee and R. S. Fearing. Contact self-cleaning of synthetic gecko adhesive from polymer microfibers. *Langmuir* **2008**, 24, 10587-10591.
45. T. Kim, H. E. Jeong, K. Y. Suh, and H. H. Lee. Stoooped nanohairs: geometry-controllable, unidirectional, reversible, and robust gecko-like dry

Chapter 1. Introduction

- adhesive. *Adv. Mater.* **2009**, *21*, 2276-2281.
46. C. Pang, et al.. Bioinspired reversible interlocker using regularly arrayed high aspect-ratio polymer fibers. *Adv. Mater.* **2012**, *24*, 475-479.
47. Y. Zhao, et al. Interfacial energy and strength of multiwalled-carbon-nanotube-based dry adhesive. *J. Vac. Sci. Technol. B.* **2006**, *24*, 331-335.
48. L. Ge, S. Sethi, L. Ci, P. M. Ajayan, and A. Dhinojwala. Carbon nanotube-based synthetic gecko tapes. *Proc. Natl. Acad. Sci. USA* **2007**, *104*, 10792-10795.
49. L. Qu, L. Dai, M. Stone, Z. Xia, and Z. Wang, Carbon nanotube arrays with strong shear binding-on and easy normal lifting-off. *Science* **2008**, *322*, 238-242.
50. L. Qu and L. Dai. Gecko-foot-mimetic aligned single-walled carbon nanotube dry adhesives with unique electrical and thermal properties. *Adv. Mater.* **2007**, *19*, 3844-3849.
51. T. Tong, Y. Zhao, L. Delzeit, A. Kashani, and A. Majumdar. Multiwalled carbon nanotube/nanofiber arrays as conductive and dry adhesive interface materials. *Proc. ASME 2004 3rd Integr. Nanosys. Conf.* **2004**, 1-5.
52. M. Park, et al.. Effect of a carbon nanotube layer on electrical contact resistance between copper substrates. *Nanotechnology* **2006**, *17*, 2294-2303.
53. H. Ko, et al.. Hybrid core-shell nanowire forests as self-selective chemical connectors. *Nano Lett.* **2009**, *9*, 2054-2058.
54. R. Kapadia, et al.. Hybrid core-multishell nanowire forests for electrical connector applications. *Appl. Phys. Lett.* **2010**, *94*, 263110.
55. J. Glazer. Microstructure and mechanical properties of Pb-Free solder alloys for

Chapter 1. Introduction

- low-cost electronic assembly: a review. *J. Electron. Mater.* **1994**, *23*, 693-700.
56. B. A. Cook, I. E. Anderson, J. L. Harringa, R. L. Terpstra. Effect of heat treatment on the electrical resistivity on near-eutectic Sn-Ag-Cu Pb-Free solder alloys. *J. Electron. Mater.* **2002**, *31*, 1190-1194.
57. S. K. Kang, W. K. Choi, M. J. Yim, and D. Y. Shin. Studies of the mechanical and electrical properties of Lead-free solder joints. *J. Electron. Mater.* **2002**, *31*, 1292-1303.
58. S. M. L. Nai, J. Wei, and M. Gupta. Effect of carbon nanotubes on the shear strength and electrical resistivity of a Lead-free solder. *J. Electron. Mater.* **2008**, *37*, 515-522.

2. Room-Temperature Bonding Technique Based on Copper Nanowire Surface Fastener

2.1 Introduction

Recently, nanowires have quickly become the focus of worldwide research owing to their unique properties. Vertically aligned and freestanding nanowire arrays are expected to have high performance in microelectronics, optics, catalysis, and biomedicine [1, 2]. In this chapter, the possible application of copper nanowire array in room-temperature bonding was explored. A room-temperature bonding technique was realized by pressing two copper nanowire arrays against each other. The van der Waals forces between the interconnected nanowires contributed to the room-temperature bonding which exhibited good mechanical and electrical properties. Moreover, scanning electron microscopy (SEM) observation showed only a small portion of nanowires interconnected, and if most nanowires could interconnect with each other, much better mechanical and electrical properties could be obtained.

2.2 Experimental section

2.2.1 Anodized aluminum oxide template

The anodized aluminum oxide (AAO) templates can be prepared by the well-known two-step anodization process [3] and they have hexagonally distributed straight nanopores. The special structural features and the thermal and chemical stability make it suitable to produce nanowire or nanotube structures. The diameter

Chapter 2. Copper Nanowire Surface Fastener

and depth of the highly ordered holes could be adjusted by changing the anodizing solutions, voltage or current density, solution temperature, and pore widening [4]. Due to these advantages, nanowires or nanotubes of a variety of materials including metal [5], semiconductor materials [6], and polymer materials [7, 8] have been fabricated by using AAO template [9].

In the previous research [10], three types (20 nm, 100 nm and 200 nm in diameter) of AAO membrane were used and the template with 20 nm nominal pore diameter was shown to be the most efficient one in increasing the mechanical and electrical properties of nanowire surface fastener. In this study, Whatman anodized alumina oxide (AAO) membranes with a nominal pore diameter of 20 nm were utilized as templates. As can be seen in **Fig. 2-1**, it is a translucence membrane with a diameter of 13 mm.

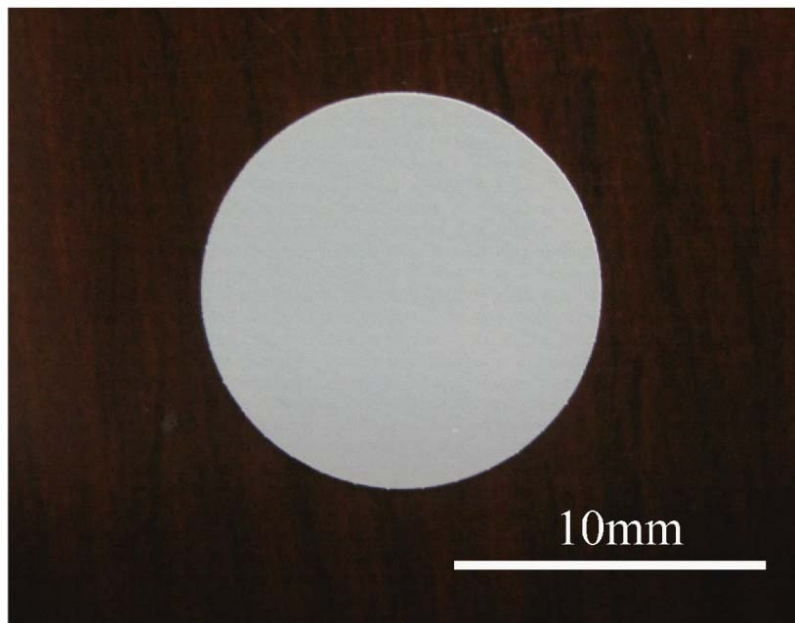


Fig. 2-1 Overall image of the commercial AAO template.

Chapter 2. Copper Nanowire Surface Fastener

The texture of AAO template was investigated by a JEOL JSM-7000K high resolution thermal field emission scanning electron microscope (SEM) (**Fig. 2-2**). Whatman AAO membranes had a thickness of 60 μm and a pore density of 10^9 pores/ cm^2 . It is found that the two surfaces of this kind template are different. This kind template consists of a support layer and an active layer [11]. As can be shown in **Fig. 2-3** and **2-4**, The active layer is composed of 20 nm pores (branched side), and has a thickness of 2-3 μm . The support layer is composed of straight, cylindrical pores of ~ 180 nm average diameter, and has a thickness of 57-58 μm (**Fig. 2-3** and **2-5**).



Fig. 2-2 Image of JSM-7000K.

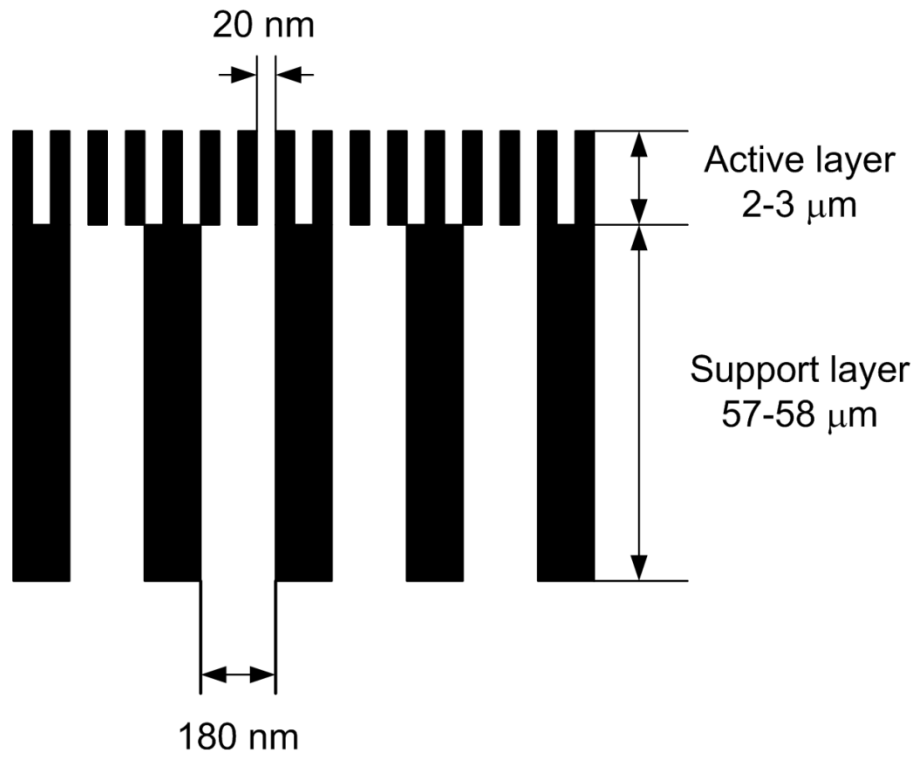


Fig. 2-3 Scheme of the pore structure and dimensions of Whatman template [11].

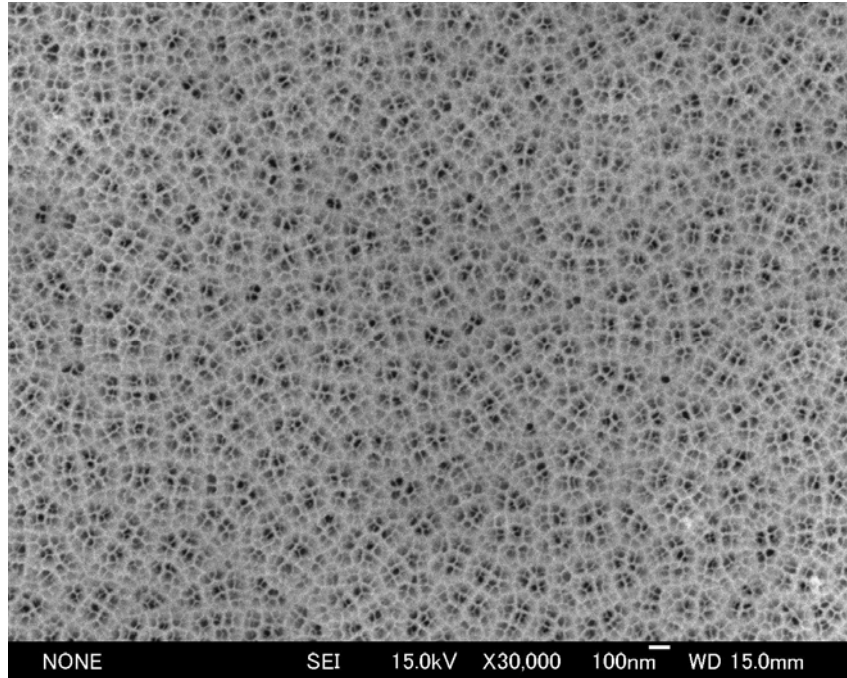


Fig. 2-4 SEM image of active layer of Whatman Template.

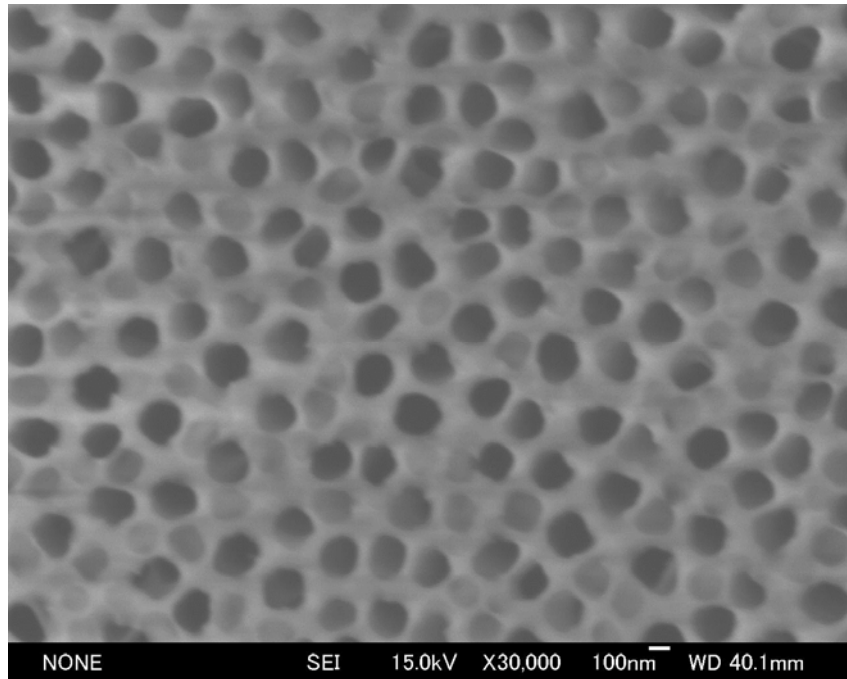


Fig. 2-5 SEM image of support layer of Whatman template.

2.2.2 Pattern design and fabrication

The sample which has specific pattern for the fastener areas and printed wires, as shown in **Fig. 2-6**, was designed to facilitate the mechanical and electrical testing. A mask fabricated by wire-electrode cutting was used to facilitate the formation of the pattern, and its relative design data was shown in **Fig. 2-7**.

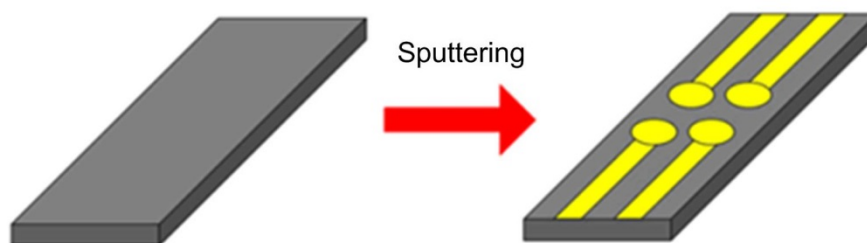


Fig. 2-6 Schematic of specific pattern on the substrate.

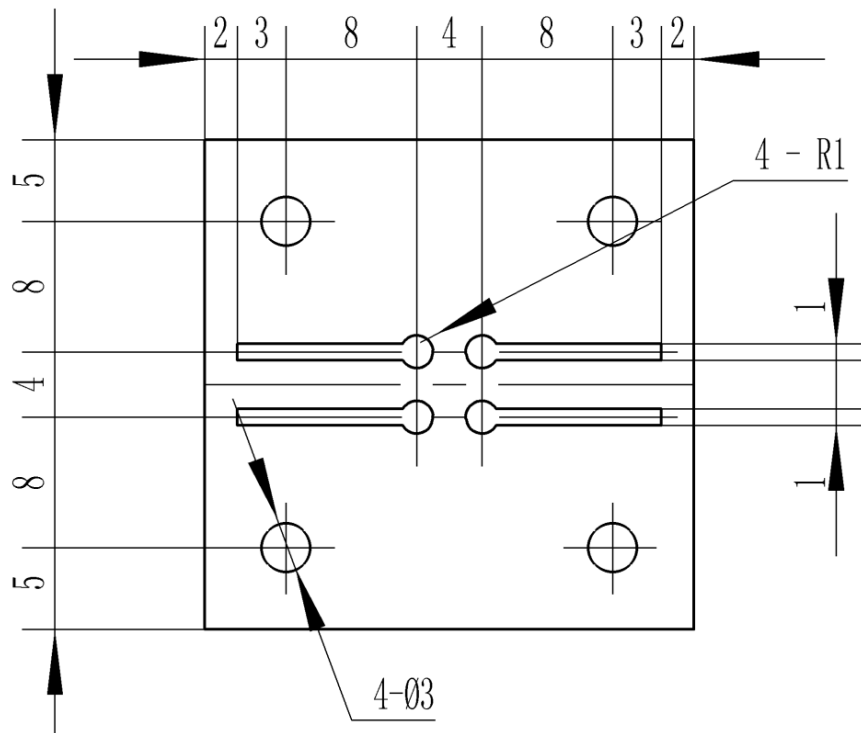


Fig. 2-7 Image of the mask used.



Fig. 2-8 Photo of sputtering machine, E-200S.

With the help of mask, the pattern was fabricated through depositing 50 nm Cr

Chapter 2. Copper Nanowire Surface Fastener

film and 100 nm Au film. Cr has been considered as a most favorable diffusion barrier for Au. Moreover, Cr demonstrates enhanced Au texture and strengthened adhesive between the Si or glass layer and the subsequently deposited Au film. Au film served as the seed layer for the subsequent electrodeposition. The deposition was carried out in sputter system (sputter machine E-200S, as shown in **Fig. 2-8**). Argon gas was used as the sputtering gas and the working pressure was set to be around 10 Pa.

2.2.3 Template-assisted electrodeposition

Electrodeposition has been widely used to make thin films and coating for a long period [12, 13]. Through the reduction of the desired metal cations by an electric current, electrodeposition can form a coherent metal film on an electrode. If electrodeposition was performed on some non-conductive substrates, some pretreatments were needed to be applied first on the surface of the non-conductive substrates, such as electroless chemical deposition, sputtering, and EB vapor coating etc. The electrolyte could be aqueous solution of salts or fused salts [12]. Electrolyte composition, applied potential, electrical current, electrolyte pH value and temperature are five main processing parameters of this electrodeposition technique [14].

The electrodeposition electrolyte used was a 0.4 M $\text{CuSO}_4 \cdot 5\text{H}_2\text{O}$ solution, adjusted at pH=2 with sulfuric acid. The electrodeposition was performed at room temperature and without stir. A copper disk was used as a sacrificial electrode (anode). The inter-electrode distance was kept 40 mm and a current of 5 mA was applied (**Fig. 2-9**).

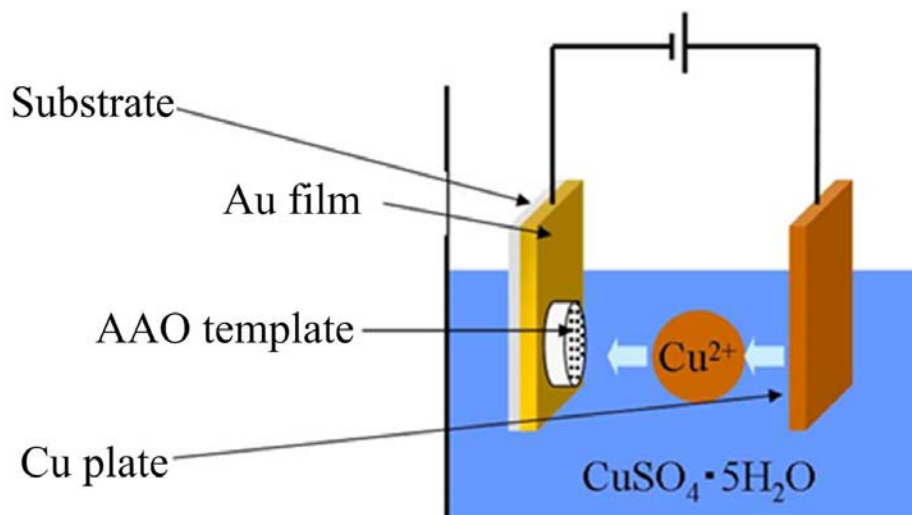


Fig. 2-9 Image of AAO electrodeposition.

In order to fabricate Cu nanowire array on the Au coated substrate directly, we try to let the AAO template contact with the substrate directly. Then, how to achieve the even contact between the substrate and the template becomes the biggest problem in our research. After trials and errors, some valuable tips were obtained and shown in the following [15, 16]. Before assembly of the stacked cell (**Fig. 2-10(c)**), the template was immersed into deionized water for 30 minutes. Then the wet template was fixed above the substrate directly, which will reduce the air bubbles and dry pores effectively. The long immersion period (30 minutes) could help the water permeate the membrane thoroughly. After the assembly (**Fig. 2-10(d)**), the stacked cell was immersed in aqueous electrolyte for 3 hours, which was aimed to let the Cu ions permeate the membrane uniformly.

Although the twice immersions before and after the assembly were quite easy, these innovative processes were crucial. In our experiment, no copper would be electro-deposited in the central area without the first immersion because a big bubble will be formed in that area; the contrast of the electro-deposition rate between the

Chapter 2. Copper Nanowire Surface Fastener

border and central area became smaller when the period of the second immersion became longer. Through introducing twice additional immersions, the method to place the membrane on the substrate directly was hopeful to be utilized in many applications which need the support of the substrate.

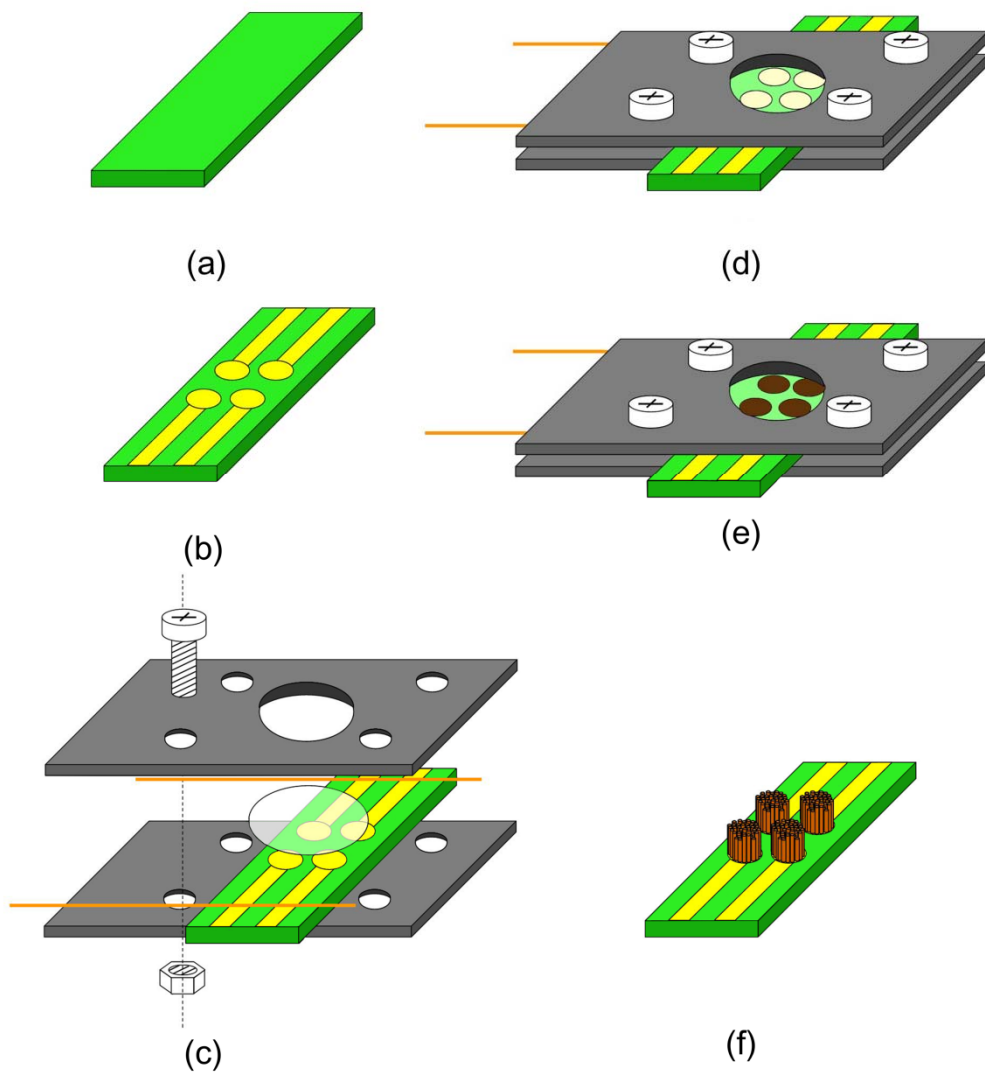


Fig. 2-10 Schematics of the method of Cu NSF fabrication: (a) Si substrate. (b) patterned Au film; (c) Fixing Si wafer and AAO template; (d) Before electrodeposition; (e) After electrodeposition; (f) Cu NSF [16].

After deposition, the stacked cell was etched in 2M NaOH solution for 6 hours to remove the AAO template. Then, the cell was dismantled, and resulting samples were soaked in 10% (v/v) hydrochloric acid for 2 hours to dissolve the surface copper oxide.

2.2.4 Testing of adhesive strength and electrical resistance

To better understand the adhesive performance of the nanowire surface fastener (NSF), we carried out macroscopic measurement of adhesive strength, which is defined as the force acted to the NSFs to separate their bonding divided by the bonding area, in directions of normal and shear. As shown in **Fig. 2-11**, two NSF samples which had patterned Cu nanowire arrays on the substrate were brought into connection with a preload. Then a gradually increasing shear or normal force, which is parallel or perpendicular to the surface of the NSF, was applied until a separation occurred.

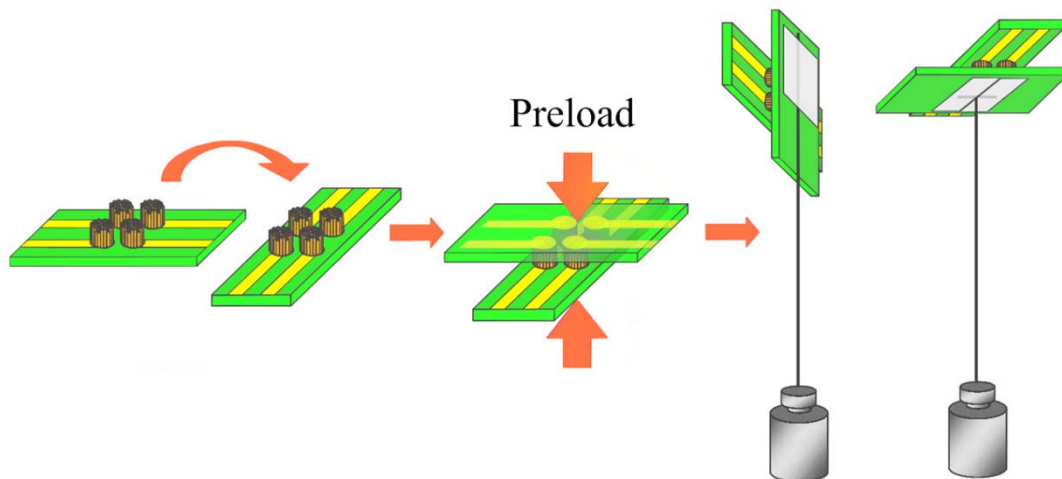


Fig. 2-11 Schematic of adhesive strength testing [15].

To measure the electrical resistance, the four-point probe method shown in **Fig.**

2-12 was used. The current in the range from 0 to 2 mA was applied using the current source and the corresponding voltage was extracted from the voltmeter. Through the least square method, the resistance was obtained. Because the thickness of sputtered Au film is in nanoscale, the electrical resistance of it is relatively high. Hence, the effect of Au film's electrical resistance was removed in order to guarantee the accuracy of measurement result. In the experiment, the total electrical resistance was measured at first as shown in **Fig 2-12(a)**. Then the electrical resistance of the Au film was measured as shown in **Fig. 2-12(b)**. The electrical resistance for the interconnected nanowire fasteners was obtained after removing the electrical resistance of Au film.

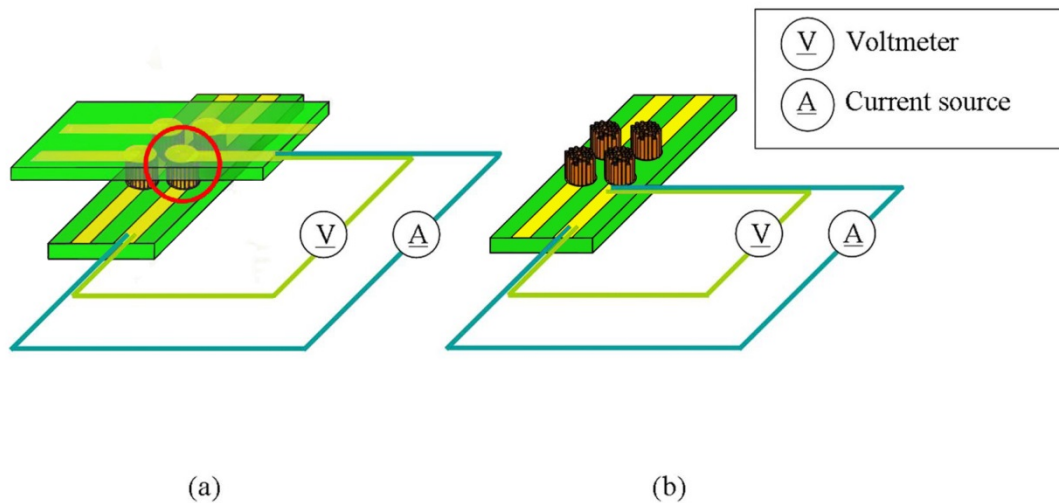


Fig. 2-12 Schematic of four-point probe measurement of interconnected NSF's [16].

2.3 Experimental results

As can be seen in **Fig. 2-13**, it was easy to distinguish the fastener area from the printed wire because the former became red due to the copper nanowires. Scanning electron microscopy (SEM) observation indicated that a copper nanowire array grew

Chapter 2. Copper Nanowire Surface Fastener

in the entire fastener area and the length of the nanowire array was uniform in most areas. The SEM observation (**Fig. 2-14**) further showed that the diameter of the fabricated nanowires is much larger than the nominal diameter. Similar results were also reported by other researchers [11, 17]. The diameter of nanowires was irregular. The nanowires were measured through ImageJ (an image analysis software), and their mean diameter was found to be around 180 nm.

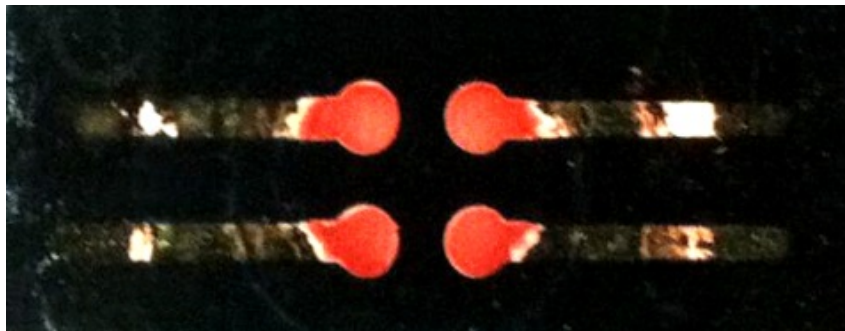


Fig. 2-13 Photograph of the sample after synthesis of Cu nanowire.

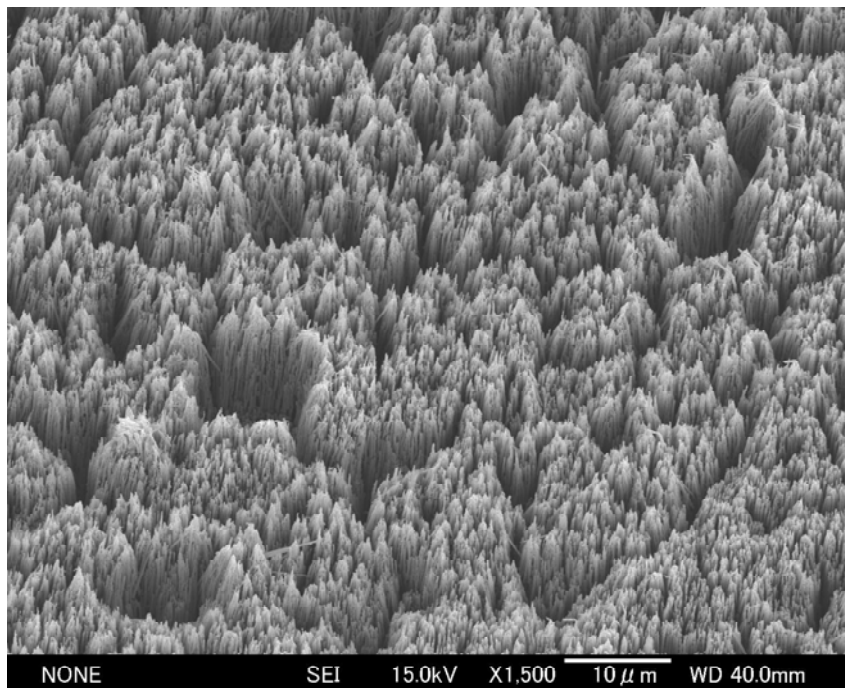


Fig. 2-14 SEM image of the fabricated Cu nanowire array.

As shown in **Fig. 2-15**, the surface of the copper nanowire was straight and

Chapter 2. Copper Nanowire Surface Fastener

smooth. The lattice fringe spacing shown in **Fig. 2-16** was measured to be approximately 0.208 nm, which corresponded to the {111} plane of the Cu crystal. It was also noticed from **Fig. 2-16** that no grain boundaries were formed along the Cu nanowire, which indicated that the Cu nanowire was single-crystalline.

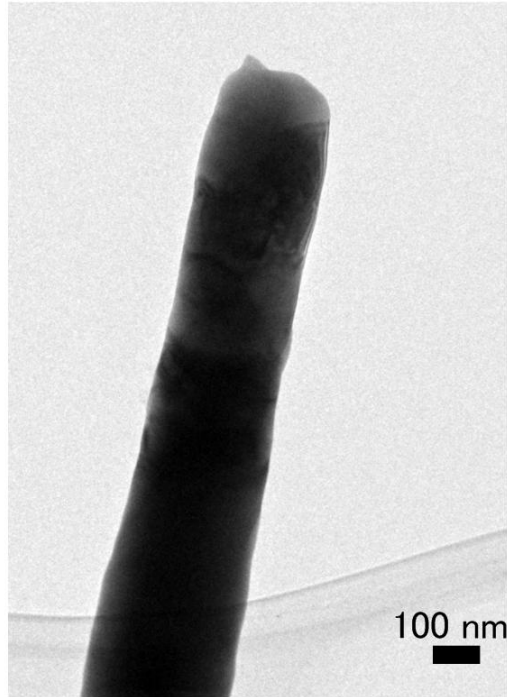


Fig. 2-15 TEM image of a fabricated Cu nanowire.

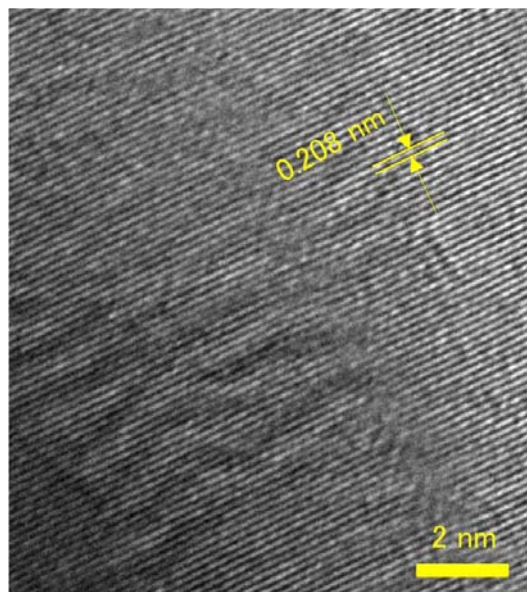


Fig. 2-16 High resolution TEM image of a part of the nanowire shown in **Fig. 2-15**.

Chapter 2. Copper Nanowire Surface Fastener

To better understand the adhesive performance of the nanowire surface fastener (NSF), we carried out macroscopic measurement of adhesive strength, which is defined as the force acted to the NSFs to separate their bonding divided by the bonding area, in normal and shear directions. As shown in **Fig. 2-11**, two NSF samples which had patterned Cu nanowire arrays on the silicon substrate were brought into interconnection at the preloads of 4.9, 9.8 and 19.6 N. Then, a gradually increasing shear or normal force, which is parallel or perpendicular to the surface of the NSF, was applied until a separation occurred. An example of the strong bonding achieved is shown in **Fig. 2-17** in which a copper NSF with a surface area of $\sim 12.56 \text{ mm}^2$ enables 100 g ($\sim 0.98 \text{ N}$) of weight to be hung with the shear direction without failure.



Fig. 2-17 Photo showing a weight of 100g hanging on the interconnected Cu NSF.

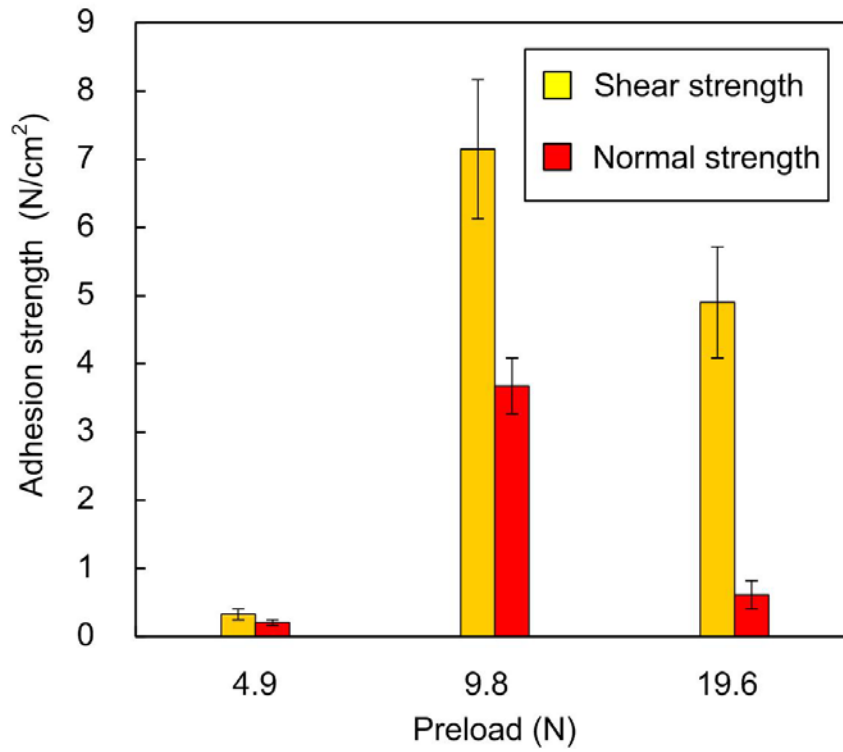


Fig. 2-18 Shear and normal adhesive strengths at the preloads of 4.9, 9.8 and 19.6 N.

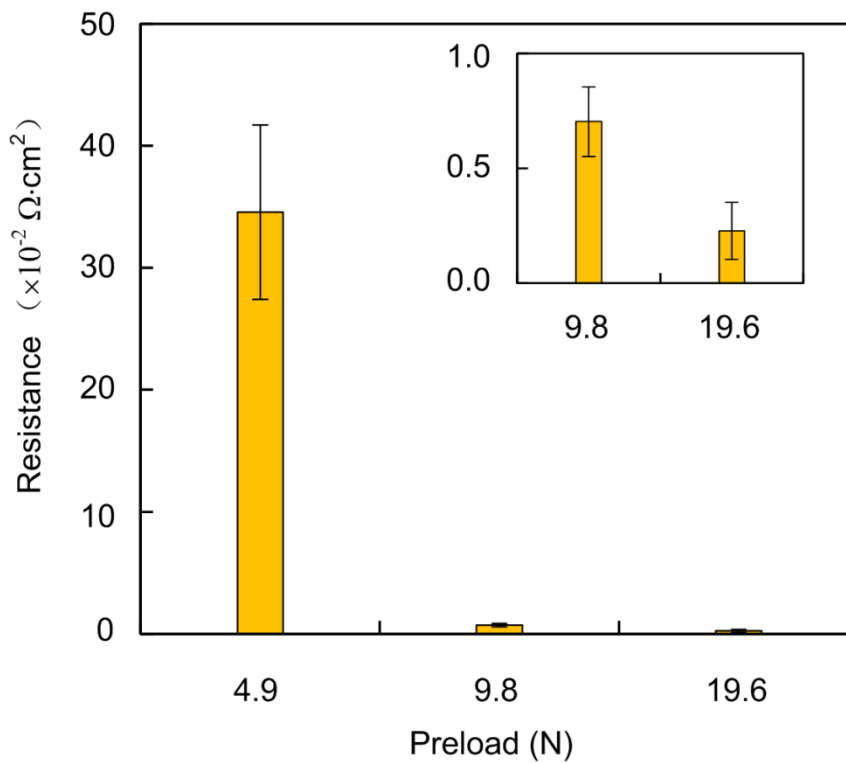


Fig. 2-19 Electrical resistances of Cu NSF at the preloads of 4.9, 9.8 and 19.6 N.

As shown in Fig. 2-18, the maximum shear and normal strengths were obtained

Chapter 2. Copper Nanowire Surface Fastener

when the preload was 9.8 N. The maximum adhesive strength of 8.17 N/cm^2 is comparable to the adhesive strength of a gecko's foot (10 N/cm^2) [18], and is much higher than that of Au NSF (5 N/cm^2) [10]. The electrical resistance measurement was performed by the four-point probe method, which has been shown in **Fig. 2-12**. The current in the range from 0 to 2 mA was applied using the current source and the corresponding voltage was extracted from the voltmeter. **Fig. 2-19** shows the electrical resistances of one interconnected pattern of NSF (2 mm diameter) at different preloads. With the increase of preload, the electrical resistance decreased dramatically just as expected. This phenomenon could be explained as that the larger preload could bring better interconnection between the upper and lower nanowire arrays. It should be noted that when the preload was 9.8 N the average electrical resistance was $0.22 \text{ } \Omega$ for one interconnected pattern of Cu NSF. After the normalization by the contact area, the electrical resistance is $0.69 \times 10^{-2} \text{ } \Omega \cdot \text{cm}^2$, which is almost ten times better than the previous result of Au NSF ($6.28 \times 10^{-2} \text{ } \Omega \cdot \text{cm}^2$) [10]. The reason may be that the copper nanowire arrays fabricated by the improved electrodeposition method are straight and uniform in length, which contributes to better interconnection.

In order to further investigate the mechanism, the SEM images of the interconnected copper nanowire arrays with different preloads (4.9, 9.8 and 19.6 N) were observed in **Fig. 2-20**, **2-21**, **2-22** and **2-23**. **Fig. 2-20** shows the overall image of two interconnected nanowire arrays without a preload; the length of the fabricated nanowire was measured to be around $45 \text{ } \mu\text{m}$. As shown in **Fig. 2-21**, when the preload was 4.9 N, only a small portion of nanowire arrays interconnected with each other. This explains why the adhesive strength was relatively low and the electrical resistance was large. When the preload was 9.8 N (**Fig. 2-22**), much larger

Chapter 2. Copper Nanowire Surface Fastener

interconnection was achieved so that both the adhesive strength and electrical properties improved dramatically. However, when the preload increased to 19.6 N (**Fig. 2-23**), a certain nanowires were bent to 90° and the interconnection portion fell down, which reduced the adhesive properties of the NSF.

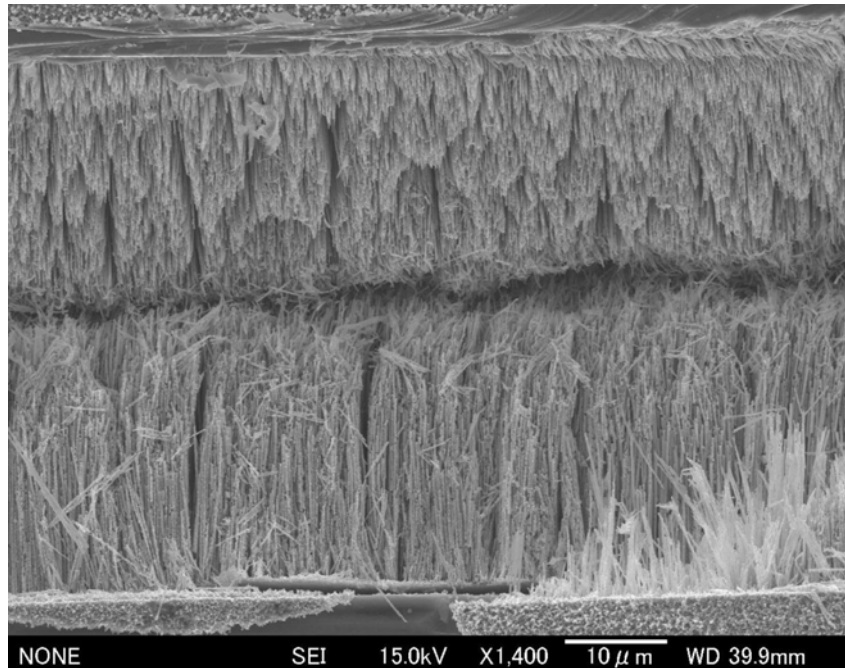


Fig. 2-20 Overall SEM image of interconnected nanowire array without preload.

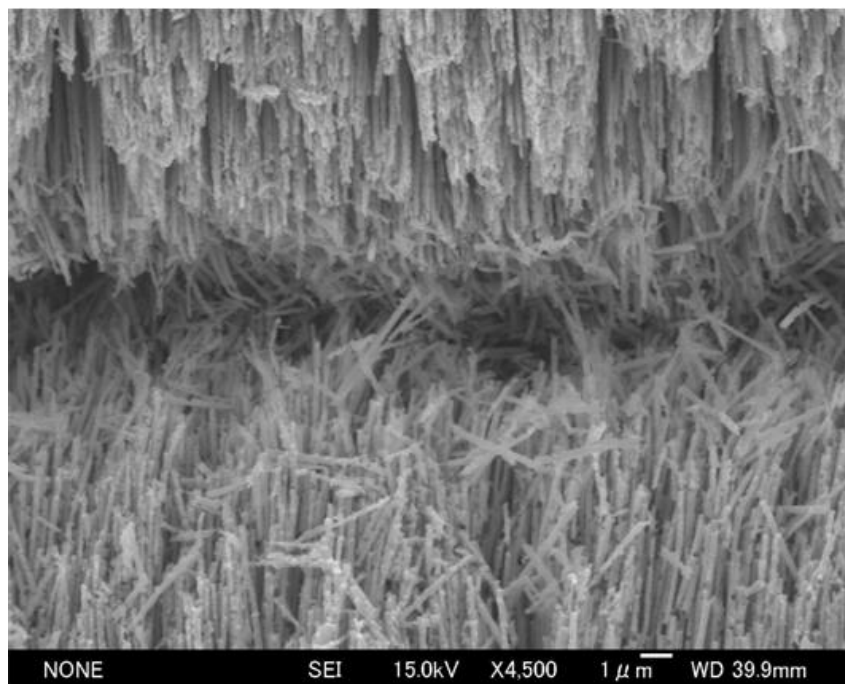


Fig. 2-21 SEM images of interconnected nanowire arrays at the preloads of 4.9 N.

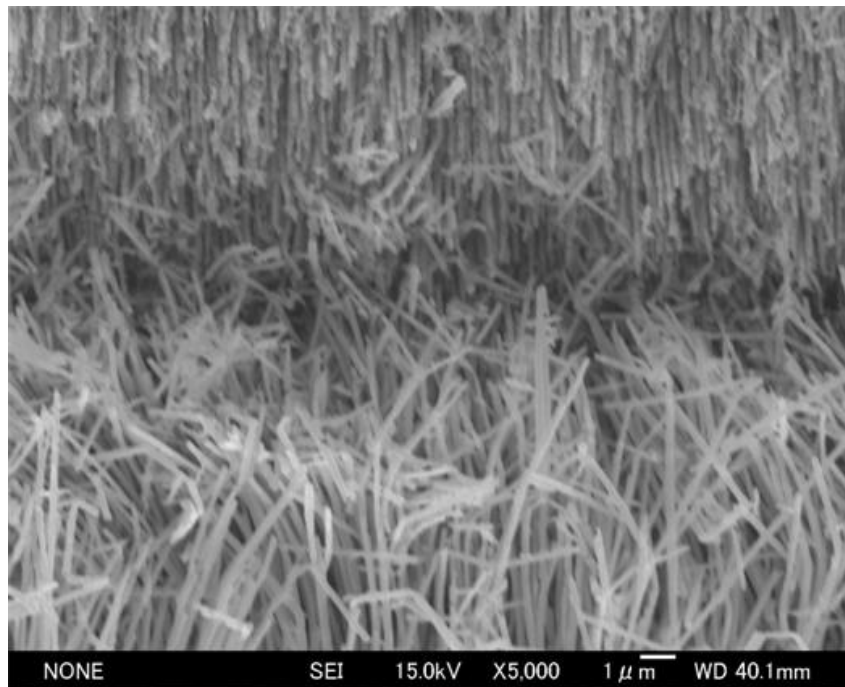


Fig. 2-22 SEM images of interconnected nanowire arrays at the preloads of 9.8 N.

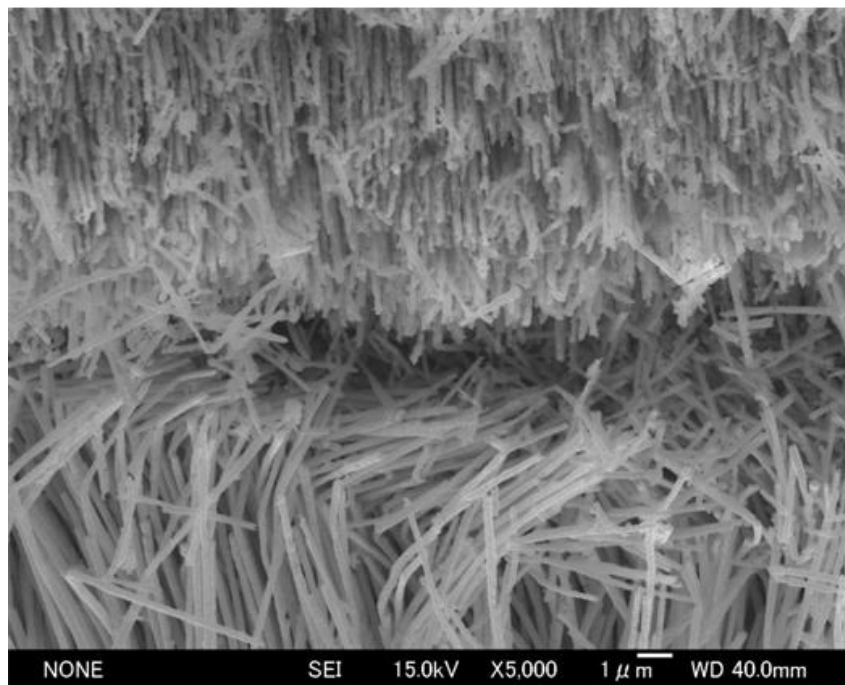


Fig. 2-23 SEM images of interconnected nanowire arrays at the preloads of 19.6 N.

Figure 2-24, 2-25, and 2-26 shows the top-view SEM images of the nanowire

Chapter 2. Copper Nanowire Surface Fastener

array at the preloads of 4.9, 9.8 and 19.6 N after the first debonding. Plastic deformations were found after separating the interconnected nanowire arrays, and larger preload tended to caused larger plastic deformation. **Figures 2-24** and **2-25** showed a cluster-like structure, which indicated that the interconnection changed the direction of nanowires. Moreover, the length of tilted nanowires observed in **Fig. 2-24** is larger than that in **Fig. 2-25**, which indicates that the interconnection of the nanowires at the preload of 9.8 N is better than that at 4.9 N (**Fig. 2-27** (b) and (c)). On the other hand, **Fig. 2-26** shows a surface-like structure, which indicated that too large plastic deformation tend to reduce the contact area (**Fig. 2-27** (d)).

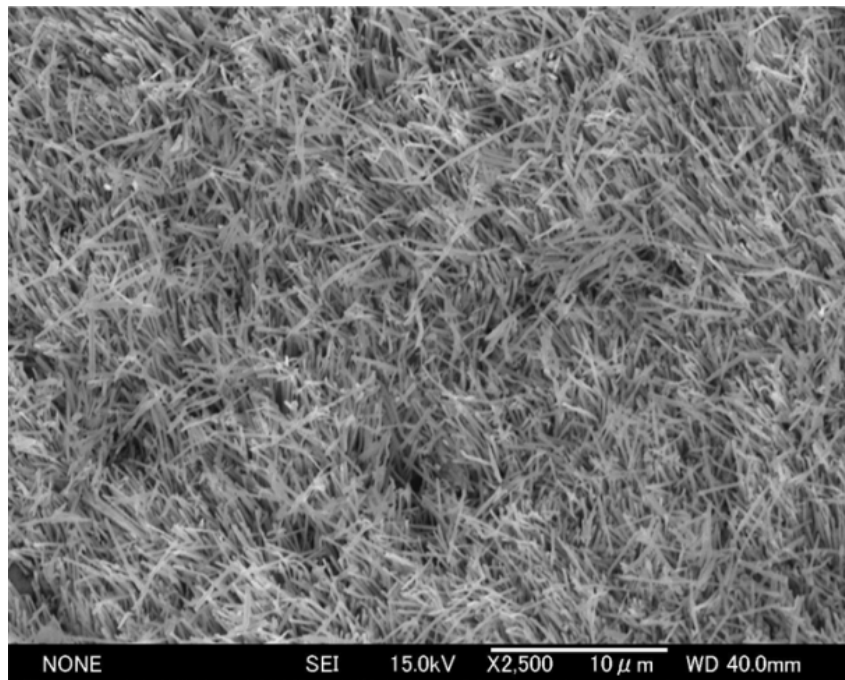


Fig. 2-24 Top-view SEM images of the nanowire array at the preloads of 4.9 N after the first debonding.

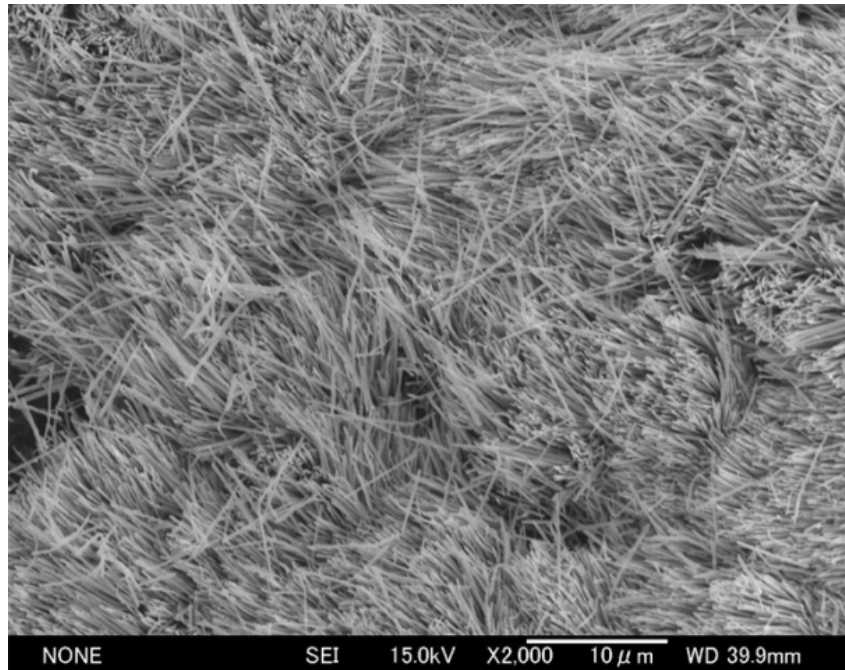


Fig. 2-25 Top-view SEM images of the nanowire array at the preloads of 9.8 N after the first debonding.

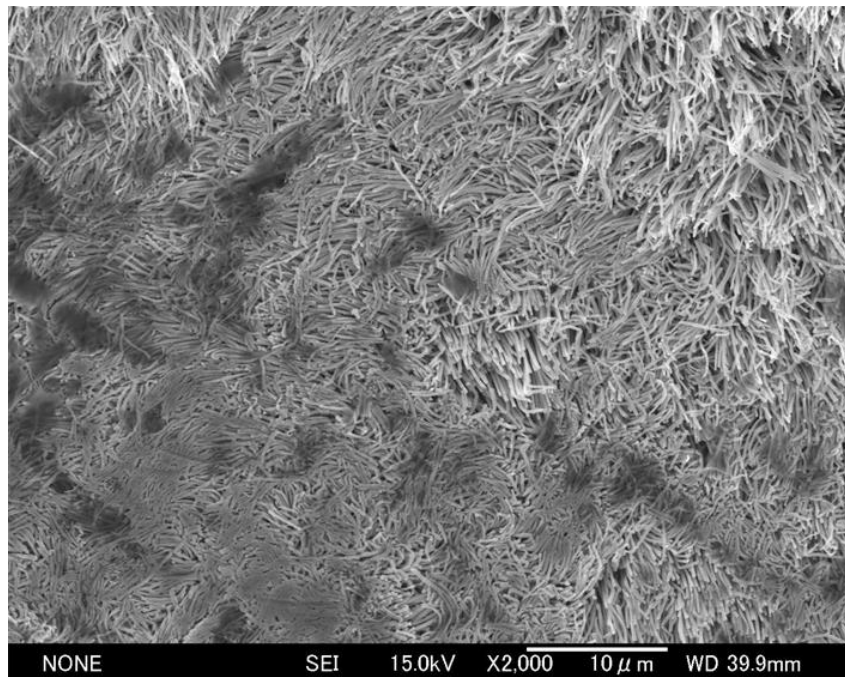


Fig. 2-26 Top-view SEM images of the nanowire array at the preloads of 19.6 N after the first debonding.

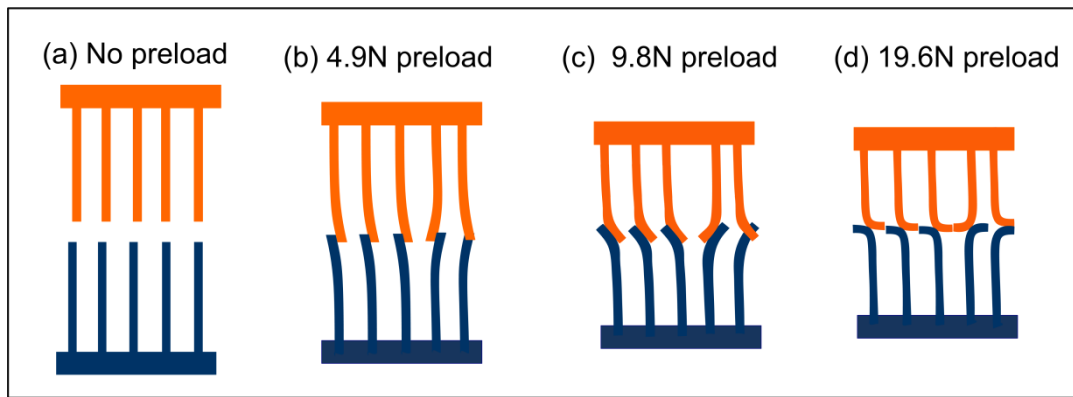


Fig. 2-27 Illustrations of interconnected nanowire arrays (a) before applying the preload and at the preload of (b) 4.9, (c) 9.8 and (d) 19.6 N.

2.4 Van der Waals force theory

Van der Waals (VDW) forces arise from the fluctuations in the electric dipole moments of molecules which becomes correlated as the molecules come closer together, giving rise to an attractive (in the same way that two rotating magnets become aligned and attract each other as they approach) [19]. **Fig. 2-28** shows a general case of van der Waals interaction, in which body 1 and body 2 interacted with each other across medium 3.

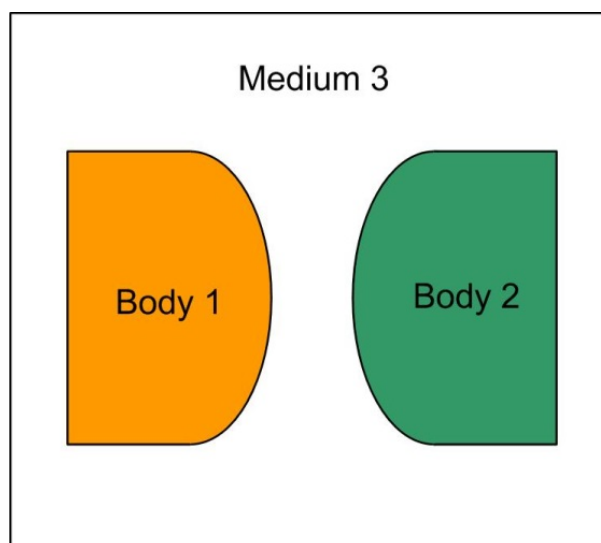


Fig. 2-28 A general case of van der Waals interaction.

2.4.1 Hamaker constant

The Hamaker constant A was generally used to describe the interaction between macroscopic bodies or surfaces. In the original treatment of Hamaker, also called the microscopic approach, the total interaction was calculated by assuming pair-wise additivity of the contributions from individual molecules [20]. However, there are several limitations to this method. The Lifshitz theory has overcome the problem of additivity. It is a continuum theory which neglects the atomic structure. In this study, both body 1 and body 2 as shown in **Fig. 2-28** are two copper nanowires with the same dimensions. In this special case, the Hamaker constant for two same materials interacting across a medium is given by the “Lifshitz theory” as [19]:

$$A = A_{v=0} + A_{v>0} = \frac{3}{4}kT \left(\frac{\varepsilon_1 - \varepsilon_3}{\varepsilon_1 + \varepsilon_3} \right)^2 + \frac{3h\nu_e}{16\sqrt{2}} \frac{(n_1^2 - n_3^2)^2}{(n_1^2 + n_3^2)^{3/2}} \quad (2-1)$$

where ε_1 , ε_3 and n_1 , n_3 are the static dielectric constants and refractive indices of the material and medium, respectively. Symbol k is the Boltzman constant (1.38×10^{-23} J·K⁻¹), T the absolute temperature, h the Plank constant (6.63×10^{-34} J·s), and ν_e the material's absorption frequency (3×10^{15} s⁻¹ for most materials) [19]. The good agreement between theory and experiment for the equation, which is strictly valid only for macroscopic bodies at separations larger than molecular dimensions, is fortuitous: the Lifshitz theory of van der Waals forces assumes that matter is a structureless continuum and it should therefore not apply at the molecular level [19].

2.4.2 Van der Waals expressions

The cut-off distance D_0 represents the effective separation between two surfaces or particles in contact. It is not a rigorously defined quantity. One expects it to be

Chapter 2. Copper Nanowire Surface Fastener

closed to an atomic or molecular dimension and, indeed, values in the range 0.15-0.4 nm, usually provide good estimates of actual binding energies and adhesive forces. For the purpose of crude estimates of the strengths of interaction forces and energies, a ‘universal’ cut-off separation of $D_0=0.4$ nm is normally used for nanoscale contact [21, 22].

Israelachvili et al. have summarized their research together with other researchers’ works, and then listed the van der Waals interaction expressions in some limited geometries. The van der Waals expressions of parallel-contacting and perpendicular-contacting cylinders were suitable for this study. The VDW force F for parallel-contacting cylinders can be formulated as [19]:

$$F(R_1, R_2, D) = \frac{Al}{8\sqrt{2}D^{2.5}} \left(\frac{R_1 R_2}{R_1 + R_2} \right)^{0.5} \quad (2-2)$$

where l is the overlap length.

Moreover, the VDW force F for perpendicular-contacting cylinders can be formulated as [19]:

$$F(R_1, R_2, D) = \frac{A}{6D^2} (R_1 R_2)^{0.5} \quad (2-3)$$

Specially, the geometry parameter of the interconnected nanowires is the same in this study. Let $R_1=R_2=R$, the van der Waals force F in parallel-contacting cylinders model can be formulated as:

$$F_{VDW} = A\sqrt{Rl}/(16D^{2.5}) \quad (2-4)$$

Moreover, the van der Waals force F in perpendicular-contacting cylinders model can be formulated as:

$$F_{VDW} = AR/(6D^2) \quad (2-5)$$

For the simplification of calculation, here $D=D_0=0.4$ nm was used for the two cylinders connection.

2.5 Theory analysis of Cu nanowire surface fastener

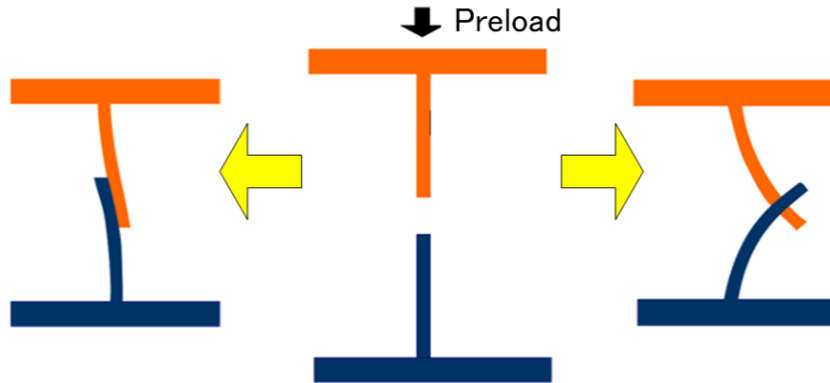


Fig. 2-29 Illustration of the two extreme conditions when the two nanowires interconnected.

Recently, many works have been done to study the mechanism of nanoscale adhesive and the van der Waals force theory has been shown to be a good method to explain such phenomenon [22, 23]. The SEM image in **Fig. 2-22** shows that the interconnected nanowires were crossed at an arbitrary angle. Here the limit of the adhesive strength was determined from two extreme conditions that are when the crossed nanowires were parallel and perpendicular to each other (**Fig. 2-29**). When the upper and lower nanowires are crossed perpendicularly, the attractive force between the two nanowires is $F_{\text{vdw}} = AR/(6D_0^2)$ [19], where A is the Hamaker constant (corresponding to the material), R is the nanowire radius and D_0 is the cut-off gap distance. The maximum shear strength per unit area is $F_{\text{shear}} = \rho F_{\text{vdw}}$ (ρ is the effective nanowires interconnect density per area). Considering $A=28.4 \times 10^{-20}$ J [24], $D_0=0.4$ nm [19], $R=90$ nm and $\rho=10^9$ cm⁻², we have $F_{\text{shear}}=26.6$ N/cm². For obtaining the corresponding normal strength, we assumed that Amonton's first law ($F_{\text{friction}}=\mu F_{\text{load}}$) [25] is effective. Considering $\mu=0.64$ [26], we have $F_{\text{normal}}=\mu F_{\text{shear}}=17.0$ N/cm². When the upper and lower nanowires are parallel, the

Chapter 2. Copper Nanowire Surface Fastener

attractive force between the two nanowires is $F_{VDW} = A\sqrt{Rl}/(16D_0^{2.5})$ [19], where l is the overlap length. Considering $l=300$ nm, $F_{shear}=\rho F_{VDW}=499.2$ N/cm² and $F_{normal}=\mu F_{shear}= 319.5$ N/cm² were obtained. Therefore, we determined that the upper limits of shear and normal strengths are 499.2 and 319.5 N/cm² respectively, and the lower limits of those are 26.6 and 17.0 N/cm² respectively. It is noted that the theoretical results are much higher than the experimental results. We attributed that this finding is due to the very high nanowire density, which prevented the interconnection between the upper and lower nanowires. From the experiment results, we predicted that only 10% of nanowires are connected and larger design space between the nanowires may be possible for further increasing the adhesive force. The poor interconnection arose from the arrangement and the density of nanowire array. As can be seen in **Fig. 2-5**, the template used in this study was disordered and the interpore distance was too small. Hence, if regular-ordered template with appropriate interpore distance was adopted, the adhesive strength will increase dramatically.

2.6 The perfect states of copper interconnection

2.6.1 The determination of adhesive strength

Consider an array of pillars laid out in a regular hexagonal pattern with spacing s between centers (**Fig. 2-30**). The radius of each pillar is R and their length is L . Then in the condition of $s=2\sqrt{3}R$, the perfect states of copper interconnection will occur and then each nanowire will be connected with three other nanowires.

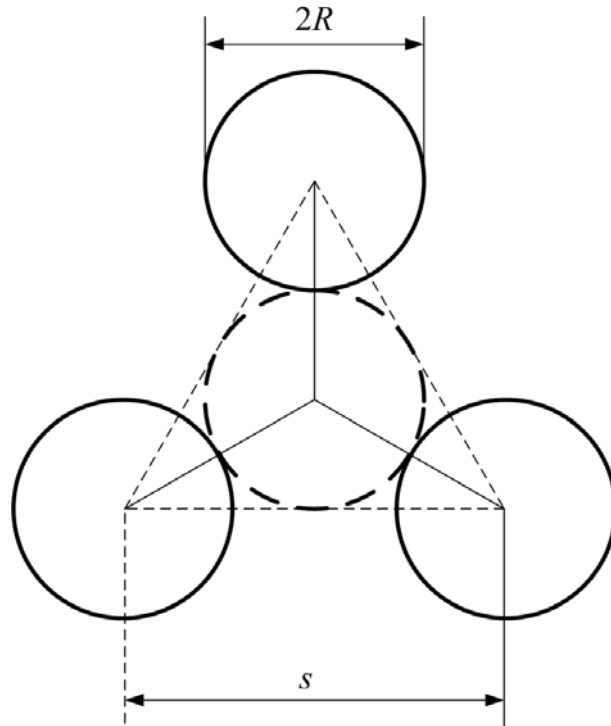


Fig. 2-30 Schematic of the perfect states of copper interconnection.

Now consider two pillar surfaces as depicted in Fig. 2-31(a) in which they are free from applied load and are just touching at the tips of the pillars. Next, compressive forces are applied to drive the surfaces together by a relative distance Δ , as depicted in Fig. 2-31(b).

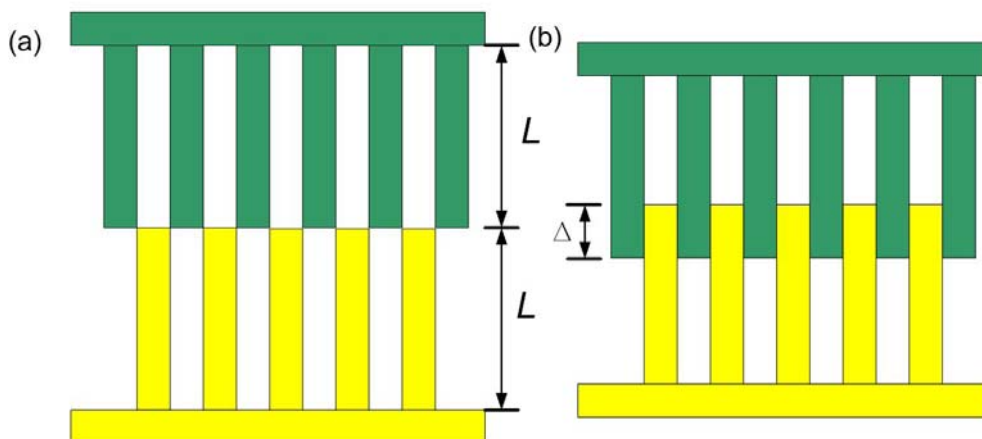


Fig. 2-31 Schematic of the attachment device: (a) prior to being engaged to create the attachment; (b) after displacement by a distance.

Chapter 2. Copper Nanowire Surface Fastener

If the interconnected nanowires were pulled apart in the shear direction which is perpendicular to the direction of nanowires, not only van der Waals forces but also mechanical forces must be overcome. On the other hand, if the nanowires were pulled apart in the normal direction which is parallel to the direction of nanowires, only the friction forces generated by the van der Waals forces must be overcome. Here, the shear and normal adhesive strength of NSF's in the perfect states were estimated and they were compared with the strength of traditional solder to confirm whether it is possible to be used for microelectronics. For simplicity, the evaluation of NSF's was carried out without considering the effect of mechanical forces which may further increase the ideal strength of NSF's.

The van der Waals forces between two nanowires were assumed to be [19]:

$$F_{VDW} = A\sqrt{R\Delta}/(16D_0^{2.5}) \quad (2-6)$$

where A is the Hamaker constant, R is the nanowire radius and D_0 is the cut-off gap distance.

As can be seen in the **Fig 2-30**, each nanowire will be connected with three other nanowires. Then the shear forces for one nanowire will be

$$F_{nanowire} = 3F_{VDW} \quad (2-7)$$

The shear adhesive strength per unit area is

$$F_{shear} = \rho F_{nanowire} \quad (2-8)$$

where ρ is the effective nanowires interconnect density per area. In perfect states, the interconnect density ρ according to the geometry conditions can be estimated by

$$\rho = 2 / 3\sqrt{3}(2R)^2 \quad (2-9)$$

Assuming the Amonton's first law ($F_{friction} = \mu F_{load}$) [25] is effective, the friction forces generated by the van der Waals forces will be

$$F_{normal} = \mu F_{shear} \quad (2-10)$$

Chapter 2. Copper Nanowire Surface Fastener

Considering $A=28.4 \times 10^{-20}$ J [24], $D_0=0.4$ nm [19] and $R=90 \times 10^{-7}$ cm, we have $F_{\text{shear}}=5938$ N/cm²=59.38 MPa when $\Delta=1$ μm . Considering $\mu=0.64$ [26], we have $F_{\text{normal}}=38.00$ MPa. The widely used Pb-free solders show adhesive strength of $\sim 10\text{-}40$ MPa [27, 28], therefore the nanowire surface fastener can be used in the microelectronics when the interconnected length is large enough. In fact, the Cu NSF we fabricated has an average length of 45 μm . When the interconnected length is as large as 45 μm , the Cu NSF in perfect states will show much better performance than the traditional solder. Hence, how to modify the structure of NSF to increase the interconnection length will be the direction of our research.

2.6.2 The determination of electrical resistance

A transmission line model has been adapted to calculate the resistance of multi-walled CNTs contacted by a metallic film [29]. Here, similar method was used to estimate the electrical resistance of copper nanowire surface fasteners. For the geometry model shown in **Fig. 2-32**, it can be divided into two parts: non-interconnected part and the interconnected part. For the non-interconnected part, the electrical resistance is simply as the resistance of copper nanowire. On the other hand, the electrical resistance is a mixture of contact resistance and the resistance of copper nanowire for the interconnected part.

The resistance of copper nanowire, R_{cu} , can be defined as:

$$R_{\text{cu}}=r_{\text{cu}} \times (L-x) \quad (2-11)$$

where r_{cu} reflects the quality of the copper nanowire. In reference [30], the electrical resistivity of copper nanowire with 60 nm diameter is 1.71×10^{-5} $\Omega \cdot \text{cm}$. Then r_{cu} can be estimated by $r_{\text{cu}}=R_{\text{cu}}/(L-x)=\rho/S$, where ρ is electrical resistivity of copper nanowire and S is the cross-section area of copper nanowire.

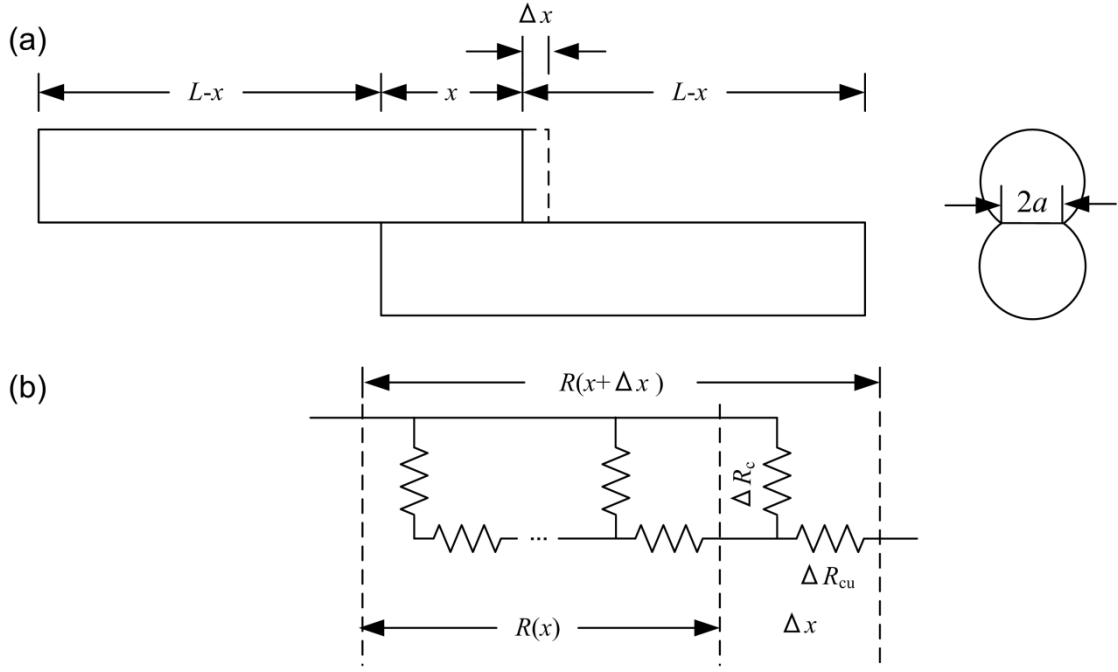


Fig. 2-32 (a) The zone of contact between two interconnected nanowires. (b) A transmission line model which was used to calculate the electrical resistance.

The specific contact resistance R_c is defined as

$$R_c = \frac{\rho_c}{A_c} \quad (2-12)$$

where is ρ_c the specific contact resistivity and A_c is the contact area. For an incremental length Δx , the incremental contact resistance can be written as $\Delta R_c \approx$

$\frac{\rho_c}{2a\Delta x}$, where $2a$ is the contact width of interconnect nanowires (**Fig. 2-32(a)**).

To simplify the discussion, $r_c = \frac{\rho_c}{2a}$ was obtained as the specific contact resistance for a unit length, where ρ_c is $0.16 \times 10^{-8} \Omega \cdot \text{cm}^2$ [31]. Then, the expression can be simply written as $\Delta R_{cu} = r_{cu} \Delta x$ and $\Delta R_c = \frac{r_c}{\Delta x}$. Let $R(x)$ equal the resistance of a copper nanowire which is interconnected with another copper nanowire over a length x . The change in resistance is $\Delta R(x) = R(x+\Delta x) - R(x)$.

Chapter 2. Copper Nanowire Surface Fastener

Fig. 2-32(b) shows the transmission line model which was used to estimate the contact resistance. Here, the contact resistance ΔR_c served as the connection in parallel and the resistance of the copper nanowire ΔR_{cu} served as the connection in series. Further, it can be derived that [29]:

$$R(x+\Delta x) = \Delta R_{cu} + \frac{1}{\frac{1}{R(x)} + \frac{1}{\Delta R_c}} \quad (2-13)$$

Then, it can be further derived that

$$\begin{aligned} R(x+\Delta x) &= \Delta R_{cu} + \frac{R(x) \cdot \Delta R_c}{R(x) + \Delta R_c} \\ &= \Delta R_{cu} + \frac{R(x) \cdot (\Delta R_c + R(x) - R(x))}{R(x) + \Delta R_c} \\ &= \Delta R_{cu} + R(x) - \frac{R^2(x)}{R(x) + \Delta R_c} \end{aligned} \quad (2-14)$$

Then, based on the equation translation, we can get

$$R(x+\Delta x) - R(x) = \Delta R_{cu} - \frac{R^2(x)}{R(x) + \Delta R_c} \quad (2-15)$$

Then, it can be derived that

$$\begin{aligned} \frac{R(x+\Delta x) - R(x)}{\Delta x} &= \frac{\Delta R_{cu}}{\Delta x} - \frac{R^2(x)}{\Delta x(R(x) + \Delta R_c)} \\ &= r_{cu} - \frac{R^2(x)}{\Delta x R(x) + \Delta x \cdot \Delta R_c} \end{aligned} \quad (2-16)$$

From the approximate value $\Delta R_c \approx \frac{\rho_c}{\Delta A_c} = \frac{r_c}{\Delta x}$, we can derive that

$$\frac{dR(x)}{dx} = r_{cu} - \frac{R^2(x)}{\Delta x \cdot R(x) + r_c} \quad (2-17)$$

As $\Delta x \rightarrow 0$ (neglecting higher order terms), we have [29]

$$\frac{dR(x)}{dx} = r_{cu} - \frac{R^2(x)}{r_c} \quad (2-18)$$

Chapter 2. Copper Nanowire Surface Fastener

Upon integrating, a general express for $R(x)$ can be derived [29]:

$$R(x) = \sqrt{r_{\text{cu}} r_c} \left[\frac{1 + e^{-2\sqrt{\frac{r_{\text{cu}}}{r_c}}x}}{1 - e^{-2\sqrt{\frac{r_{\text{cu}}}{r_c}}x}} \right] = \sqrt{r_{\text{cu}} r_c} \coth\left(\sqrt{\frac{r_{\text{cu}}}{r_c}}x\right) \quad (2-19)$$

Returning to the geometry model in **Fig. 2-32(a)** the total resistance from two interconnected nanowires can be given by

$$R_{\text{total}}(x) = \sqrt{r_{\text{cu}} r_c} \coth\left(\sqrt{\frac{r_{\text{cu}}}{r_c}}x\right) + 2r_{\text{cu}}(L - x) \quad (2-20)$$

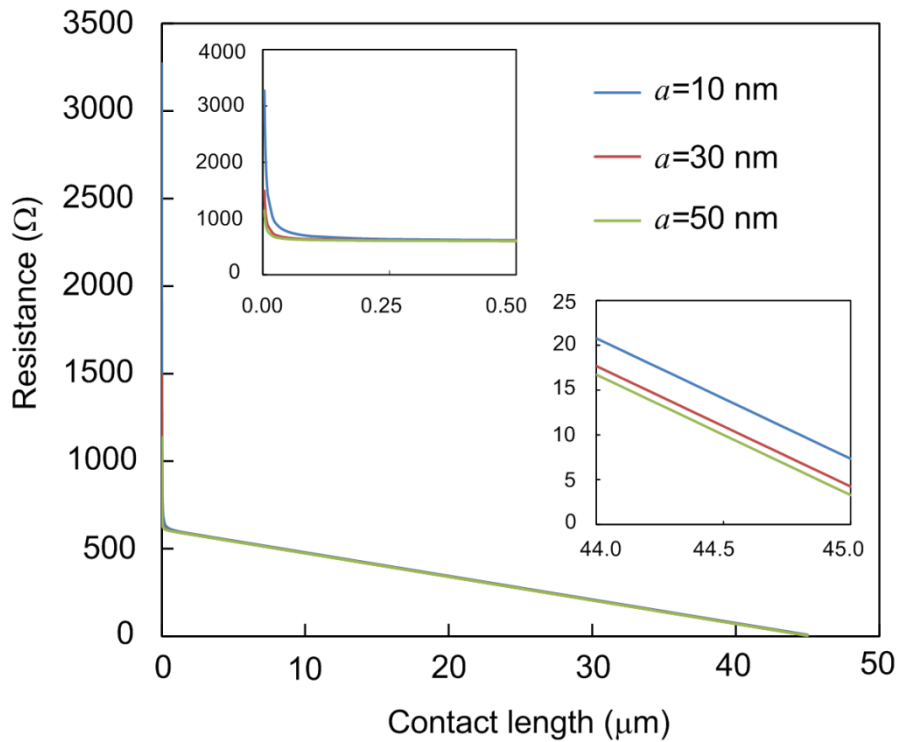


Fig. 2-33 Representative plot of equation (2-20) to illustrate the effect of the parameter a and x on the predicted resistance.

Fig. 2-33 illustrated the prediction of this model for different contact width a as x is varied when the radius of copper nanowire is 90 nm. Compared with x , the contact width a had few effect on the predicted resistance. When the interconnected length is

Chapter 2. Copper Nanowire Surface Fastener

45 μm , the electrical resistance is $\sim 7.3 \Omega$ for $a=10 \text{ nm}$. The interconnected upper and lower nanowire array can be simply considered as parallel connection for the electrical resistance estimation and the interconnect density in the perfect states can be obtained from equation (2-9). Moreover each nanowires will be connected with three other nanowires in the perfect states, the interconnected nanowires served as connection in parallel and the resistance of NSF is estimated to be $2.05 \times 10^{-9} \Omega \cdot \text{cm}^2$. The widely used Pb-free solders show the electrical resistance of $\sim 15.6-62.5 \times 10^{-7} \Omega \cdot \text{cm}^2$ [27]. Hence, the nanowire surface fastener has the potential to show better performance than traditional solder.

2.7 Tilted copper nanowire surface fastener

Recently, synthetic gecko adhesives with uniformly tilted angle have shown anisotropic adhesive properties [32, 33]. Moreover, the research has shown that one part of microhairs in gecko's foot is slight bent in one direction, which can prevent the movement of the gecko's foot in some preferred direction [34]. Here, a room-temperature electrical bonding technique based on tilted copper nanowire fastener with anisotropic adhesive properties was presented. A patterned structure of copper nanowire array on the silicon substrate was prepared through template-assistant electroplating. In terms of pressing the tilted and straight nanowire array against each other, the van der Waals forces between the interconnected nanowires contributed to the room-temperature bonding.

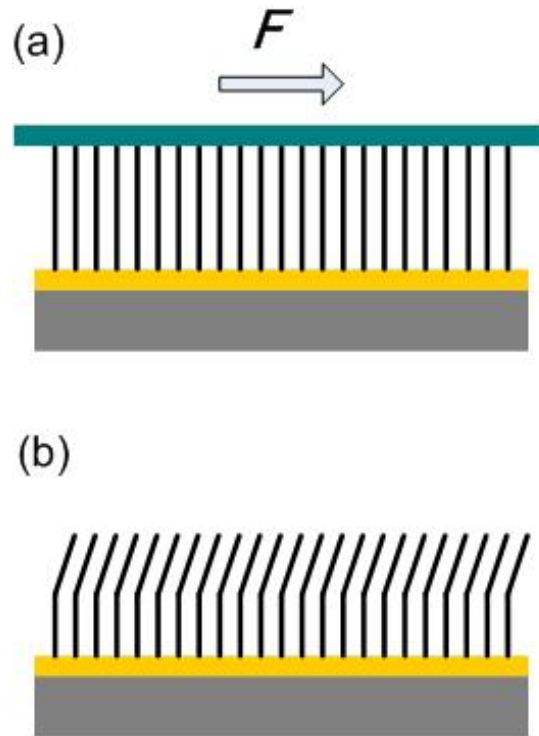


Fig. 2-34 Schematic illustration of the bending process of tilted nanowire array.

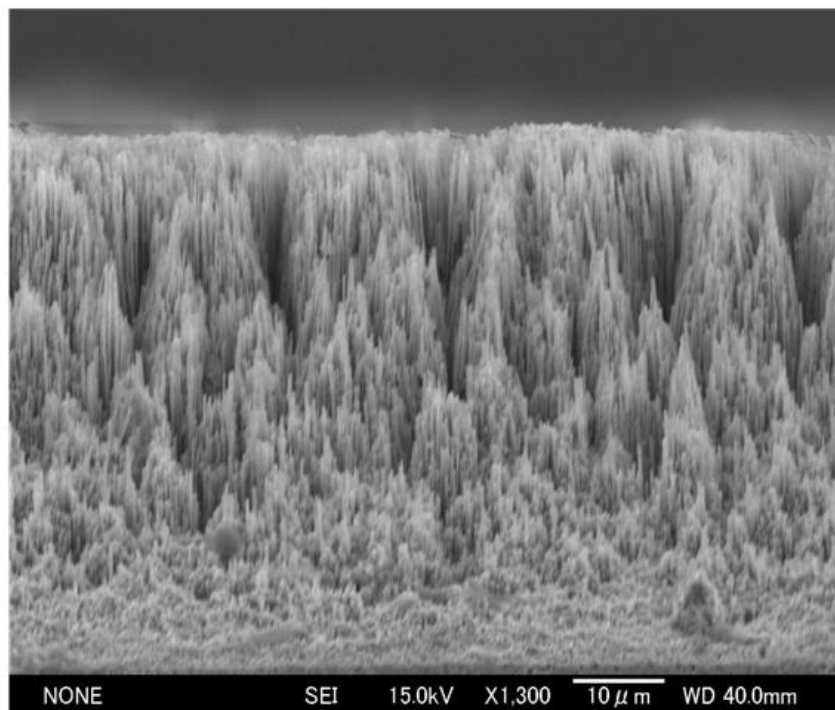


Fig. 2-35 SEM image of copper nanowire array before the mechanical bending.

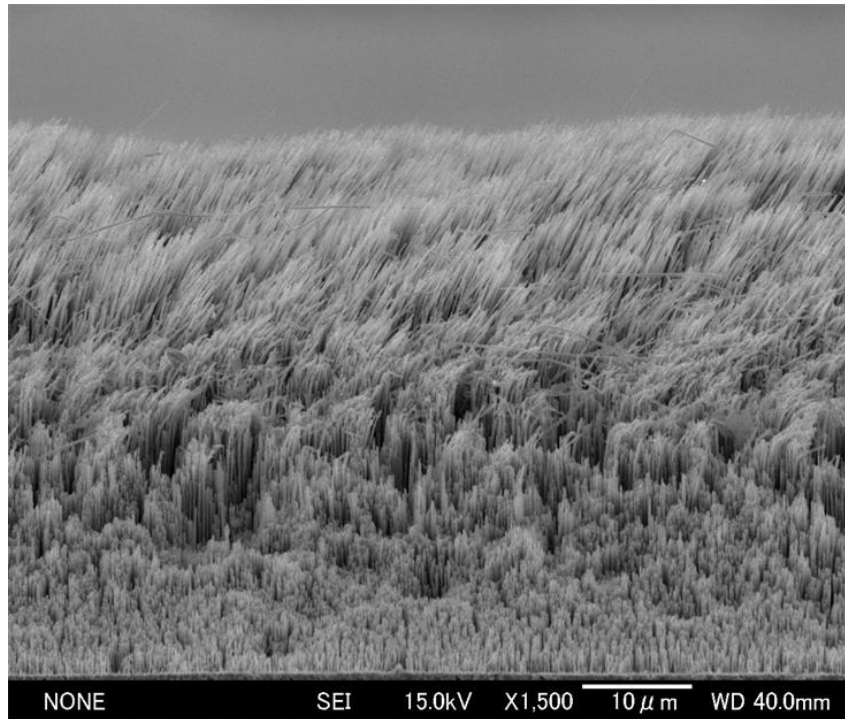


Fig. 2-36 SEM image of copper nanowire array after the mechanical bending.

Fig. 2-35 shows that the average length of these copper nanowires was approximately 45 μm . In order to obtain the tilted nanowire array, a thin polycarbonate film (~ 1 mm thick) was carefully pressed to the surface and pulled in a specified direction (**Fig. 2-34** (b)). SEM images of cross-section views of straight and tilted copper nanowire arrays were shown in **Fig. 2-35** and **Fig. 2-36**, respectively. The average tilt angle of the unloaded nanowires from the surface normal was $\theta=60^\circ$. Because the density of the nanowire array was too high, only 50% in length approximately of each nanowire was tilted.

To test the shear and normal mechanical bonding strengths afforded by the copper nanowire surface fasteners, the straight nanowire array was pressed against the tilted nanowire array under a normal preload force. Then a gradually increasing shear or normal force was applied by using the weights of a balance, until the interconnected nanowire surface fasteners separated. During the measurement, no

Chapter 2. Copper Nanowire Surface Fastener

external normal load was applied.

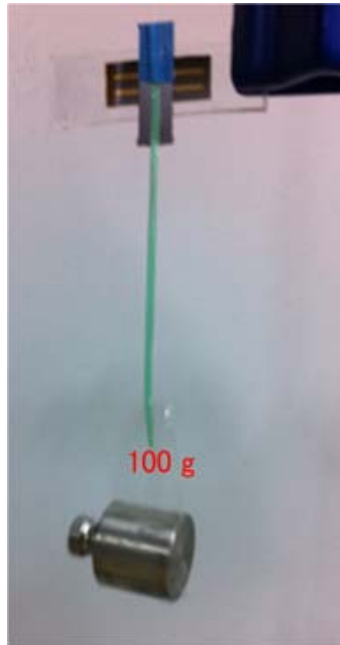


Fig. 2-37 A photo showing a weight balance of 100 g hanging on the interconnected Cu nanowire surface fasteners.

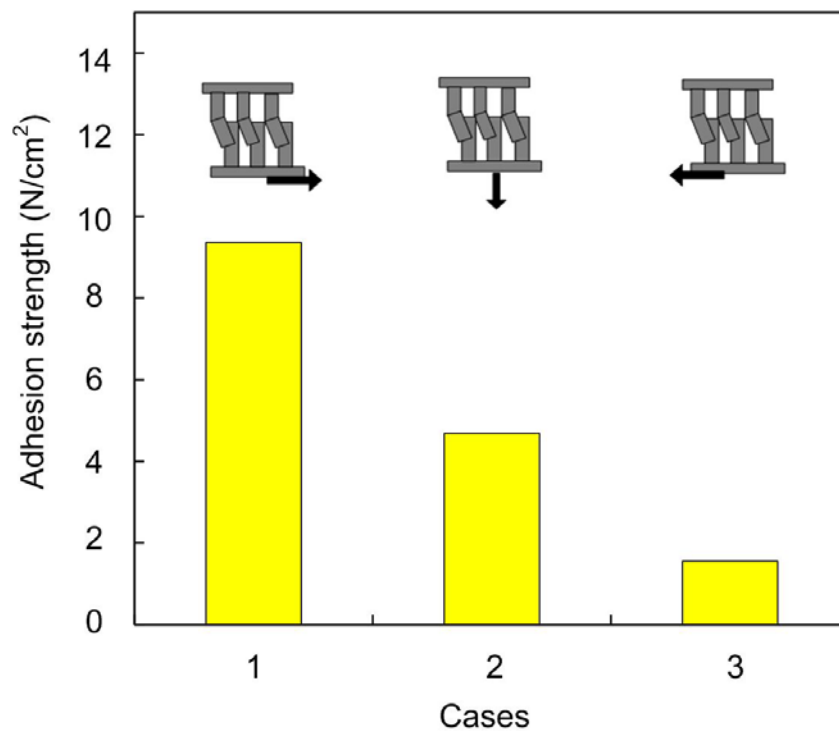


Fig. 2-38 Shear and normal adhesive strength under the preload of $\sim 9.8\text{N}$.

Chapter 2. Copper Nanowire Surface Fastener

After a preload of ~ 9.8 N, the strong bonding was achieved. The interconnected NSFs with a surface area of ~ 12.56 mm² enabled 100 g of weight in shear direction without failure (**Fig. 2-37**). As shown in **Fig. 2-38**, the normal adhesive strength was 4.68 N/cm². Moreover, the shear adhesive strengths were 9.36 and 1.56 N/cm², respectively, for the two opposite directions that are parallel and antiparallel to the tilted direction of the nanowires. Because that the tilted structure increases the side contact area in one direction and decreases the side contact area in the opposite direction, the anisotropic adhesive property was obtained. Regarding to the room temperature bonding or solder in the microelectronics, there are some design guidelines about the ratio between the component's weight and the bonding area. According to the standard value of weight-area ratio for surface mount technology ($R=30$ g/in²) [35], the smallest bonding strength ($S= 1.56$ N/cm² in one shear direction) can withstand an acceleration of $a=S/R=335$ N/kg, which is thirty times larger than g ($g=9.8$ N/kg is the acceleration of gravity). Hence, this room-temperature bonding technique based on the patterned copper nanowire array on the silicon substrate can be applied in most equipment. What is more, when the nanowire array of the NSF contacted with flat surfaces (silicon and Au coated silicon) under the same preload, both normal and shear adhesive were zero. Hence, this room-temperature bonding technique is a self-selective bonding only with special structures.

This room temperature bonding technique is not only effective for mechanical bonding but also electrical conductive for electrical connections. The details of electrical resistance measurement have been shown in **Fig. 2-12**, and the electrical

Chapter 2. Copper Nanowire Surface Fastener

resistance of 0.3Ω was obtained for this kind of nanowire surface fastener. After normalization, the electrical resistance is $\sim 0.94 \times 10^{-2} \Omega \cdot \text{cm}^2$.

Table 2.1 Calculated values from VDW theory and experimental results.

		Adhesive strength (N/cm ²)		Resistance ($\Omega \cdot \text{cm}^2$)
		Shear	Normal	
Theory	Parallel-contacting	499.2	319.5	
	Perpendicular-contacting	26.6	17.0	
	Ideal-contacting	5938	3800	2.05×10^{-9}
Experiment	NSF	8.17	4.10	0.69×10^{-2}
	Tilted NSF	9.36/1.56	4.68	$\sim 0.94 \times 10^{-2}$
Traditional Pb-free solder		1000-4000 [27]	3000-4000 [28]	$\sim 15.6-62.5 \times 10^{-7}$ [27]

Finally, the results of experiment and theoretical analysis in this chapter are summarized in **Table 2.1**. The difference in values between theory and experiment come from the arrangement and the density of nanowire array. Hence, if the nanowire array which is regular-ordered and has appropriate interpillar distance can be fabricated, much higher adhesive strength will be obtained based on the theory estimation.

2.8 Summary

In conclusion, by improved template-assisted electrodeposition, we developed a room-temperature bonding technique based on a copper nanowire surface fastener with a macroscopic adhesive strength of 8.17 N/cm^2 . Furthermore, the electrical resistance of one fastener is around $0.69 \times 10^{-2} \Omega \cdot \text{cm}^2$ under the preload of 9.8 N , which is almost ten times better than the previous result of Au NSF. Furthermore, the

Chapter 2. Copper Nanowire Surface Fastener

van der Waals force theory showed that a much higher adhesive strength can be obtained if all fabricated nanowires interconnect with each other. Furthermore, the room-temperature bonding technique based on tilted nanowire surface fastener further exhibited anisotropic adhesive properties, and the shear adhesive strengths were 9.36 and 1.56 N/cm², respectively, for the two opposite directions that are parallel and antiparallel to the tilted direction of the nanowires. The according electrical resistance of tilted nanowire surface fastener interconnected with the straight nanowire surface fastener is $\sim 0.94 \times 10^{-2} \Omega \cdot \text{cm}^2$.

REFERENCES:

1. C. Jo, J. I. Lee and Y. Jang. Electronic and magnetic properties of ultrathin Fe–Co alloy nanowires. *Chem. Mater.* **2005**, *17*, 2667-2671.
2. Y. Cui, Q. Wei, H. Park, and C. M. Lieber. Nanowire nanosensors for highly sensitive and selective detection of biological and chemical species. *Science* **2001**, *293*, 1289-1292.
3. H. Masuda and K. Fukuda. Ordered metal nanohole arrays made by a two-step replication of honeycomb structures of anodic alumina. *Science* **1995**, *268*, 1466-1468.
4. A. P. Li, F. Müller, and A. Birner. Hexagonal pore arrays with a 50-420 nm interpore distance formed by self-organization in anodic alumina. *J. Appl. Phys.* **1998**, *84*, 6023-6026.
5. G. Sauer, G. Brehm, and S. Schneider. Highly ordered monocrystalline silver nanowire arrays. *J. Appl. Phys.* **2002**, *91*, 3243-3247.

Chapter 2. Copper Nanowire Surface Fastener

6. Y. Yang, J. Chen, and H. Chen. Study of CdS nanowires deposited in silicon based porous alumina film by non-aqueous electrochemical deposition. *Chin. J. Inorg. Chem.* **2004**, *20*, 65-68.
7. M. Steinhart, R. B. Wehrspohn, U. Gösele, and J. H. Wendorff. Nanotubes by template wetting: a modular assembly system. *Angew. Chem., Int. Ed.* **2004**, *43*, 1334-1344.
8. C. Pan, L. Zhang, and J. Zhu. Surface decoration of anodic aluminum oxide in synthesis of Nafion[®]-115 nanowire arrays. *Nanotechnology* **2007**, *18*, 015302-015307.
9. G. Hu, H. Zhang, W. Di, and T. Zhao. Study on wet etching of AAO template. *Appl. Phys. Res.* **2009**, *1*, 78-82.
10. Y. Ju, M. Amano, and M. Chen. Mechanical and electrical cold bonding based on metallic nanowire surface fasteners. *Nanotechnology* **2012**, *23*, 365202.
11. G. Riveros, H. Gomez, A. Cortes, R. Marotti, and E. A. Dalchiele. Crystallographically-oriented single-crystalline copper nanowire arrays electrochemically grown into nanoporous anodic aluminum templates. *Appl. Phys. A* **2005**, *81*, 17-24.
12. M. Paunovic and M. Schlesinger. *Fundamentals of Electrochemical Deposition*, John Wiley & Sons, Inc., U.S.A, **1998**, 1-10.
13. F. A. Lowenheim. *Electroplating*, McGraw-Hill, New York, **1978**, 1-5.
14. B. Ye. Fabrication and Magnetic Property Investigation of Metallic Nanowire Arrays. Doctor Thesis, University of New Orleans **2006**.

Chapter 2. Copper Nanowire Surface Fastener

15. P. Wang, et al.. Room-temperature bonding technique based on copper nanowire surface fastener. *Appl. Phys. Express* **2013**, *6*, 035001.
16. P. Wang, Y. Ju, A. Hosoi, and Y. Song. Room temperature electrical bonding technique based on tilted copper nanowire fastener with anisotropic adhesive properties. Proc. IEEE Nano 2012 Conf. **2012**, 1-4.
17. T. R. Kline, et al.. Template-Grown Metal Nanowires. *Inorg. Chem.* **2006**, *45*, 7555-7565.
18. Y. Zhao, et al.. Interfacial energy and strength of multiwalled-carbon-nanotube-based dry adhesive. *J. Vac. Sci. Technol. B.* **2006**, *24*, 331-335.
19. D. Leckband and J. Israelachvili. Intermolecular forces in biology. *Q. Rev. Biophys.* **2001**, *34*, 105-267.
20. V. Wallqvist. Interaction between non-polar surfaces in water. Doctor Thesis, Royal Institute of Technology **2009**, 5-8.
21. C. Pang, D. Kang, T. Kim, and K. Suh. Analysis of preload-dependent reversible mechanical interlocking using beetle-inspired wing locking device. *Langmuir* **2012**, *28*, 2181-2186.
22. C. Pang, et al.. Bioinspired reversible interlocker using regularly arrayed high aspect-ratio polymer fibers. *Adv. Mater.* **2012**, *24*, 475-479.
23. L. Qu, L. Dai, M. Stone, Z. Xia, and Z. L. Wang. Carbon nanotube arrays with strong shear binding-on and easy normal lifting-off. *Science* **2008**, *322*, 238.
24. J. Visser. On Hamaker constant: a comparison between hamaker constants and lifshitz – van der Waals constants. *Adv. Colloid Interface Sci.* **1972**, *3*, 331-363.

Chapter 2. Copper Nanowire Surface Fastener

25. Y. F. Mo, K. T. Turner, and I. Szlufarska. Friction laws at the nanoscale. *Nature* **2009**, *457*, 1116-1119.
26. Y. Y. Ye, R. Biswas, J. R. Morris, A. Bastawros, and A. Chandra. Molecular dynamics simulation of nanoscale machining of copper. *Nanotechnology* **2003**, *14*, 390-396.
27. S. K. Kang, W. K. Choi, M. J. Yim, and D. Y. Shin. Studies of the mechanical and electrical properties of Lead-free solder joints. *J. Electron. Mater.* **2002**, *31*, 1292-1303.
28. S. M. L. Nai, J. Wei, and M. Gupta. Effect of carbon nanotubes on the shear strength and electrical resistivity of a Lead-free solder. *J. Electron. Mater.* **2008**, *37*, 515-522.
29. C. Lan, P. Srisungthitsunti, P. B. Amama, T. S. Fisher, X. Xu, and R. G. Reifenger. Measurement of metal/carbon nanotube contact resistance by adjusting contact length using laser ablation. *Nanotechnology* **2008**, *19*, 125703.
30. M. E. T. Molaes, et al.. Electrical characterization of electrochemically grown single copper nanowires. *Appl. Phys. Lett.* **2003**, *82*, 2139-2141.
31. K. N. Chen, C. S. Tan, R. Reif. Contact resistance measurement of bonded copper interconnects for three-dimensional integration technology. *IEEE Electro Device Lett.* **2004**, *25*, 10-12.
32. J. Lee, R. S. Fearing, and K. Komvopoulos. Directional adhesive of gecko-inspired angled microfiber arrays. *Appl. Phys. Lett.* **2008**, *93*, 191910.

Chapter 2. Copper Nanowire Surface Fastener

33. H. E. Jeong, J. -K. Lee, H. N. Kim, S. H. Moon, and K. Y. Suh. A nontransferring dry adhesive with hierarchical polymer nanohairs. *Proc. Natl. Acad. Sci. USA* **2009**, *106*, 5639-5644.
34. K. Autumn, et al.. Adhesive force of a single gecko foot-hair. *Nature* **2000**, *405*,681-685.
35. Y. Liu, D. A. Geiger, and D. Shangguan. Determination of components candidacy for second side reflow with Lead-free solder. Proc. 55th IEEE Electron. Compon. Technol. Conf. **2005**, 970-976.

3. Copper-parylene Core-shell Nanowire Surface Fastener Used for Room-Temperature Electrical Bonding

3.1 Introduction

Copper nanowire surface fastener and tilted copper nanowire surface fastener have been described in chapter 2. However, the adhesive strength is still not big enough. To solve this problem, a room-temperature electrical surface fastener consisting of copper-parylene core-shell nanowire arrays was presented in this chapter [1]. Interestingly, the parylene-C film becomes conductive due to dielectric breakdown when the thickness of it is miniaturized to nanoscale. This copper-parylene core-shell nanowire surface fastener exhibits high macroscopic adhesive strength ($\sim 25 \text{ N/cm}^2$) and low electrical resistance ($\sim 4.22 \times 10^{-2} \Omega \cdot \text{cm}^2$).

3.2 Experimental section

3.2.1 Pattern design and fabrication

The specific pattern for the fastener areas and printed wires has been shown in **Fig. 2-6** and **2-7**. With the help of mask, a $\sim 50 \text{ nm}$ thick Cr adhesive layer and a $\sim 100 \text{ nm}$ thick Au film were deposited on the glass substrate by sputter machine E200-S (**Fig. 2-8**). The diameter of each of the four fasteners was 2 mm and the width of printed wire was 1 mm .

3.2.2 Polycarbonate template

Radiation track-etched polycarbonate (PC) membranes are another kind of widely used template. PC membranes are made by bombarding a nonporous polycarbonate sheet, typically 6 to 20 μm in thickness, with nuclear fission fragments to create damage tracks, and then chemically etching these tracks into pores [2]. In these radiation track etched membranes, pores have a uniform size as small as 10 nm, but they are randomly distributed. Pore densities can be as high as 10^9 pores/ cm^2 [3].

As can be seen in **Fig. 3-1**, the overall image of polycarbonate membrane is similar with AAO template. However, due to the material difference, AAO template is rigid and fragile while polycarbonate membrane is flexible (**Fig. 3-2**). **Fig. 3-3** is the SEM top view image of commercial Isopore polycarbonate membrane manufactured by Millipore Company with 150 nm mean pore size and 20-25 μm thickness. As shown in **Fig. 3-3**, the ion track-etched membrane has non-deformed round pore shape, which is better than the commercial AAO membrane. The usual drawbacks of the radiation track-etched membranes are low porosity, bad pore distribution and tilted channels. From **Fig. 3-3**, we can find that the pores are distributed randomly and some are overlapped partially among vicinal pores. The reason why ion track-etched membranes having lots of partially overlapped pores is the random ion bombardment [2]. Besides, the tilted channels are contributed from the angler between the member surface and the flying path of heavy ions is not exact perpendicularity, which is caused by the unparallelled flying path of ions [4].



Fig. 3-1 Overall image of polycarbonate membrane.



Fig. 3-2 Photo showing the flexibility of polycarbonate membrane.

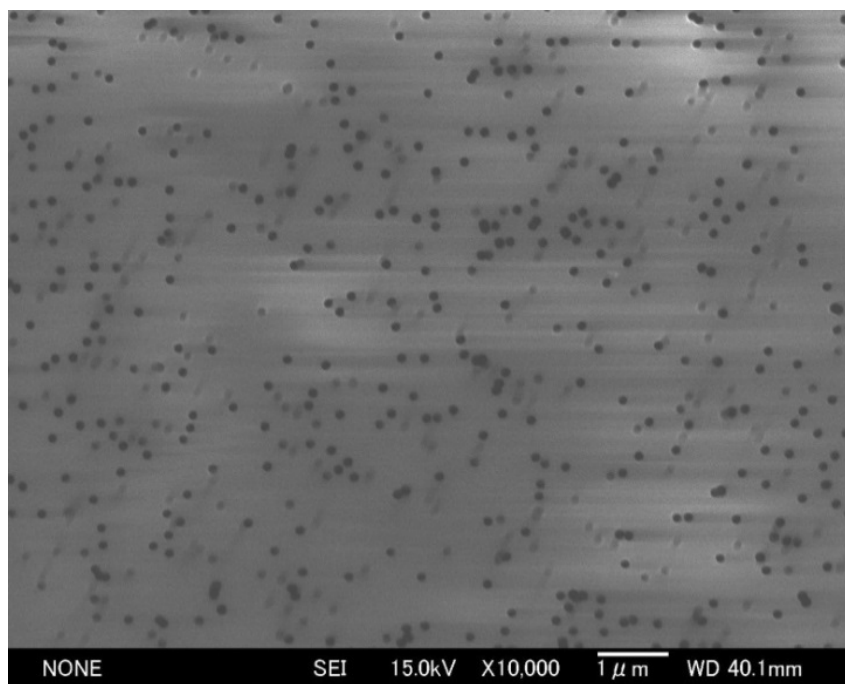


Fig. 3-3 SEM image of one surface of polycarbonate membrane.

3.2.3 Electrodeposition of copper nanowire

Polycarbonate (PC) membranes (ISOPORE, Millipore Inc.) with the pores of 150 nm diameter measured in average were used as the templates. Due to the flexibility of polycarbonate membrane, the cell shown in **Fig. 2-10** becomes unavailable. A porous glass plate and a porous cellulose paper were introduced. Porous glass plate with G1 grade (100-120 μm porous diameters) was purchased from Fujirika Tech, Japan. The kind of porous glass plate has a radius of 13 mm (**Fig. 3-4**) and a thickness of 2.5 mm. The cellulose paper was purchased from Whatman Ltd, UK (reference 1441-055). This kind of cellulose paper (**Fig. 3-5**) was 215- μm thick, with a diameter of 55 mm and a mean porous diameter of 20 μm . In the experiment, this cellulose paper will be further cut into several pieces with 13 mm diameter.



Fig. 3-4 Overall image of porous glass plate.

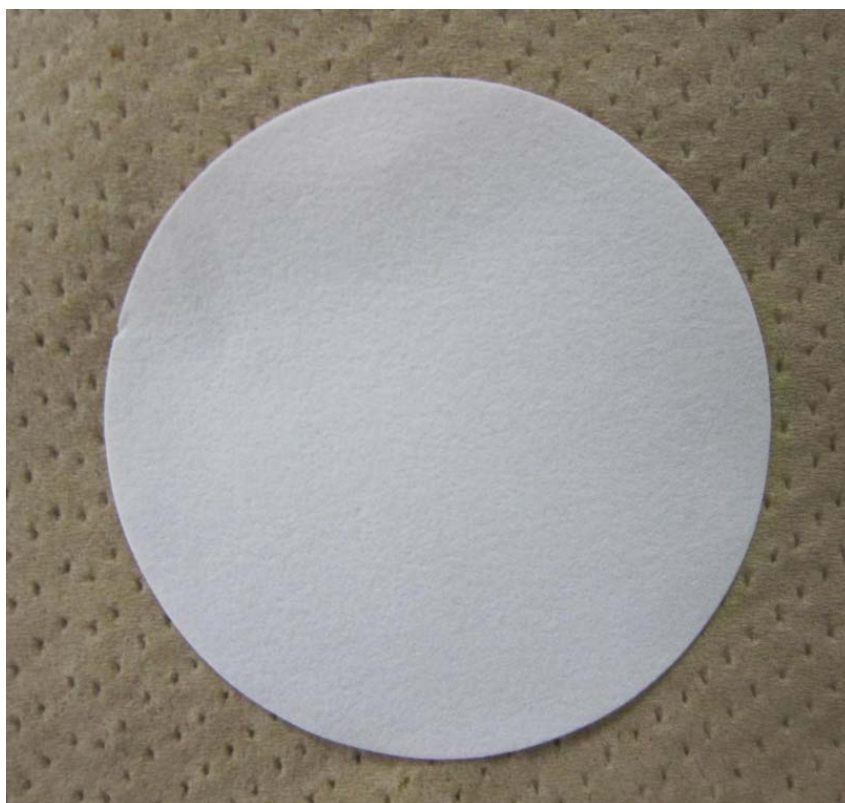


Fig. 3-5 Overall image of porous cellulose paper.

Chapter 3. Copper-parylene core-shell NSF

A peculiar cell shown in **Fig. 3-6** was used to fabricate free-standing copper nanowire on the substrate directly [1]. The introduced porous glass and porous cellulose membrane have three important functions. First, the capillary forces provided by the porous glass and porous cellulose membrane help maintain a continuous electrolyte flow from the bulk of the electrolyte to PC membrane [5]. Second, the stiffness of porous glass ensures the contact of the substrate with PC membrane. Third, the compliance of porous cellulose membrane offers a buffer and then ensures tight contact of the substrate with PC membrane. It is known that for flat anodes the metal is deposited preferentially at the outer border areas of the cathode [6]. This effect was avoided by using a conical copper anode, leading to a noticeably more homogeneous copper nanowire distribution over the whole cathode surface [7].

Before and after the assembly of the cell, two additional immersions were introduced to ensure the even copper ion density throughout the PC membrane similar as before [8]. Copper nanowire arrays were then synthesized by electrodeposition under a constant current of approximately 0.003A. The electrodeposition electrolyte used was a 0.4 M $\text{CuSO}_4 \cdot 5\text{H}_2\text{O}$ solution, adjusted at pH=2 with sulfuric acid. The electro-deposition was performed at room temperature and without stir. The inter-electrode distance was kept at 40 mm and a current of 3 mA was applied. After etching in methylene chloride to remove the PC membrane, the freestanding copper nanowire array on the substrate was obtained.

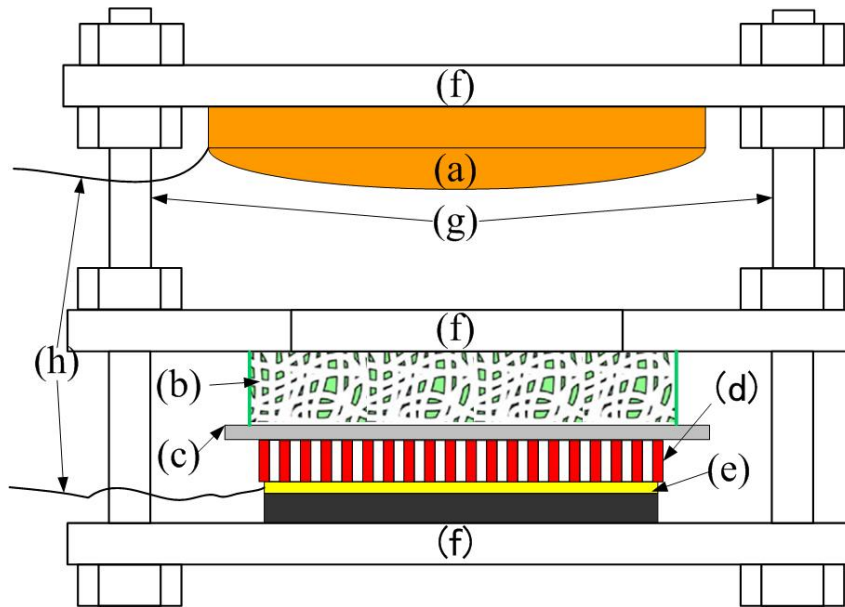


Fig. 3-6 Schematic of the cell for copper nanowire fabrication: (a) conical copper anode; (b) porous glass plate; (c) cellulose membrane; (d) polycarbonate template; (e) glass substrate with gold film; (f) isolation holder; (g) screw and nut; (h) copper wire

3.2.4 Parylene conformal coating

Parylene (name for a unique product family: poly-para-xylylene) was first discovered in 1947. Since it was discovered, research for this polymer has yield many variations (e.g. type -N, -C, -HT, etc.). Parylene-N (**Fig. 3-7**), the basic member of the series, has highest dielectric strength and the most penetration factor and conformability among the types of parylene but low deposition rate due to its low threshold temperature (40 °C) compared to other parylene types [9]. Parylene-C (**Fig. 3-7**), having substituted a single chlorine substitution for one of its aromatic hydrogen, has a slight lower conformability due to its higher molecular weight but faster deposition rate due to its high threshold temperature (90 °C). Parylene-HT (**Fig. 3-7**), which has its alpha hydrogen at the N dimer replaced with fluorine, is the most thermally stable (up to 350 °C) and best used for high temperature applications [10].

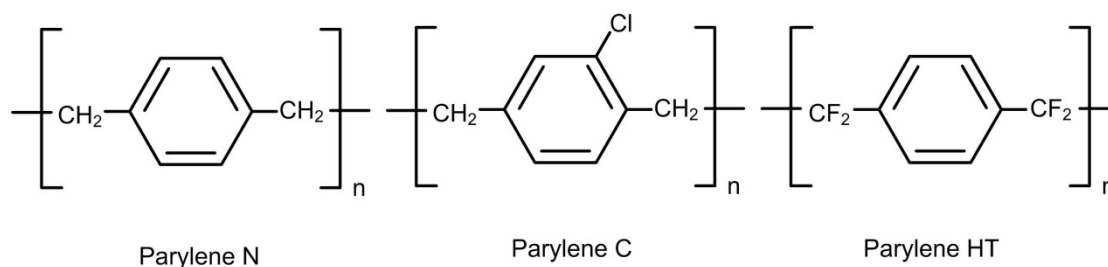


Fig. 3-7 Chemical structure of various parylene [11].

Due to the uniqueness of the vapor phase deposition, the parylene can be formed as structurally continuous films from as thin as a fraction of a micrometer to as thick as several millimeters [12]. The parylene polymers are deposited by chemical vapor deposition process which is in some respects similar with vacuum metallizing. Different from vacuum metallization which should be conducted at pressure of 10^{-5} torr or below, the parylenes can be formed at around 0.1 torr. Under these conditions the mean free path of the gas molecules in the deposition chamber is in the order of 0.1 cm [12]. Therefore, all sides of an object to be encapsulated can be uniformly impinged by the gaseous monomer. This is responsible for the truly conformal nature of coating.

In this study, a thin film of parylene-C was deposited on copper nanowire arrays by using a DACS-LAB deposition system. The deposition process is shown in **Fig. 3-8**. A typical deposition condition used in this study were 160°C for the vaporization of the parylene dimer precursor, 650°C for the pyrolysis of the dimer into monomers, and 0.06 torr for the vacuum chamber. Through controlling the amount of the loaded precursor, the corresponding thickness of parylene shell could be obtained.

Chapter 3. Copper-parylene core-shell NSF

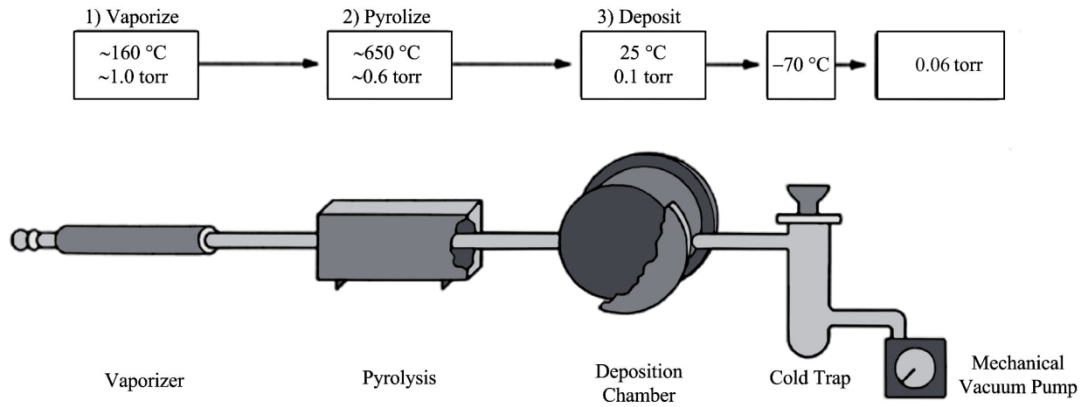


Fig. 3-8 The deposition process of parylene-C [12].

3.2.5 The electrical testing of thin parylene film

Samples were fabricated on 28×10 mm glass substrate over which a continuous layer of Au/Cr (200/50 nm thick, respectively) was sputtered to serve as the ground. With the help of mask, the specific thickness of the parylene-C film was then deposited over the central area of the substrate. To create the upper contact electrodes, a thin gold film (100 nm thick) was deposited on the parylene film in a specific pattern.

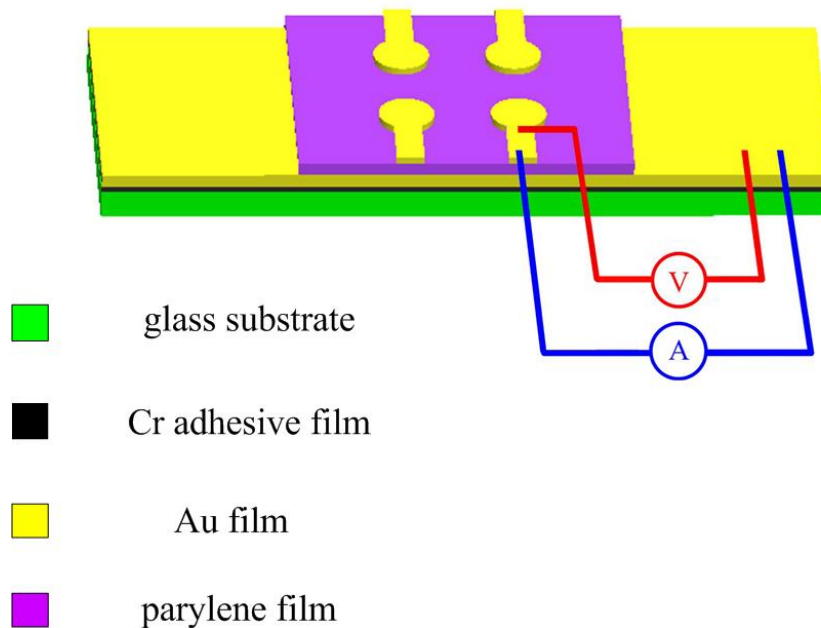


Fig. 3-9 Schematic for the electrical resistance measurement of thin parylene film.

As shown in **Fig. 3-9**, the electrical resistance measurement was performed and the current from 0 to 2 mA was applied by the current source to the four-point probe measuring circuits. The corresponding voltage was extracted from the voltmeter.

3.2.6 Testing of adhesive strength and electrical resistance

To investigate the adhesive strength, an external preload was applied by pressing two NSF samples against each other. After the preload was released, the weight of balance was used to measure the pull-off forces with the parallel (i.e. the shear adhesive strength) and normal (i.e. the normal adhesive strength) directions to the glass substrate. The experimental sketch has been shown in **Fig 2-11**. To measure the electrical resistance, the four-point probe method [8] shown in **Fig. 2-12** was used. The current in the range from 0 to 2 mA was applied by a constant current source and the corresponding voltage was extracted from a voltmeter.

3.3 Experimental results

3.3.1 The performance of thin parylene film

Fig. 3-10 shows the measured electrical resistance of the parylene-C films with different thicknesses (see **Fig. 3-11** for details). Because the parylene film is nonconductive in microscale, it is easy to understand the tendency in **Fig. 3-10** that larger parylene thickness result in larger electrical resistance. Moreover, since a constant current source was used to measure the resistance of the parylene films, the initial voltage applied to the film tended to reach the breakdown voltage so as to flow the required current. Thus, the parylene film was dielectrically break down and became conductive.

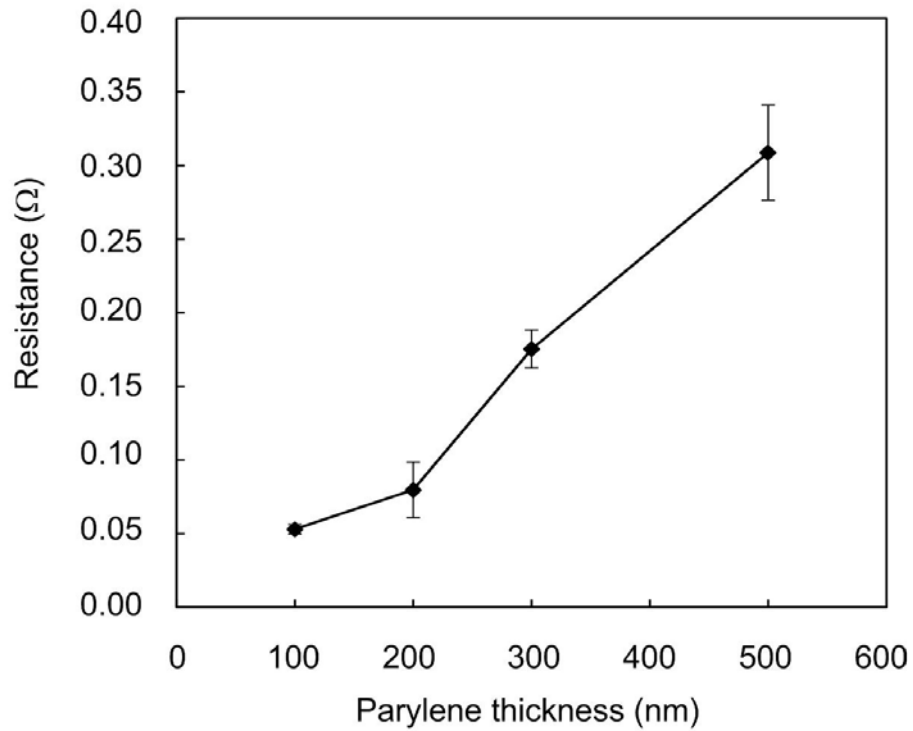


Fig. 3-10 The electrical resistance of parylene film as a function of thickness.

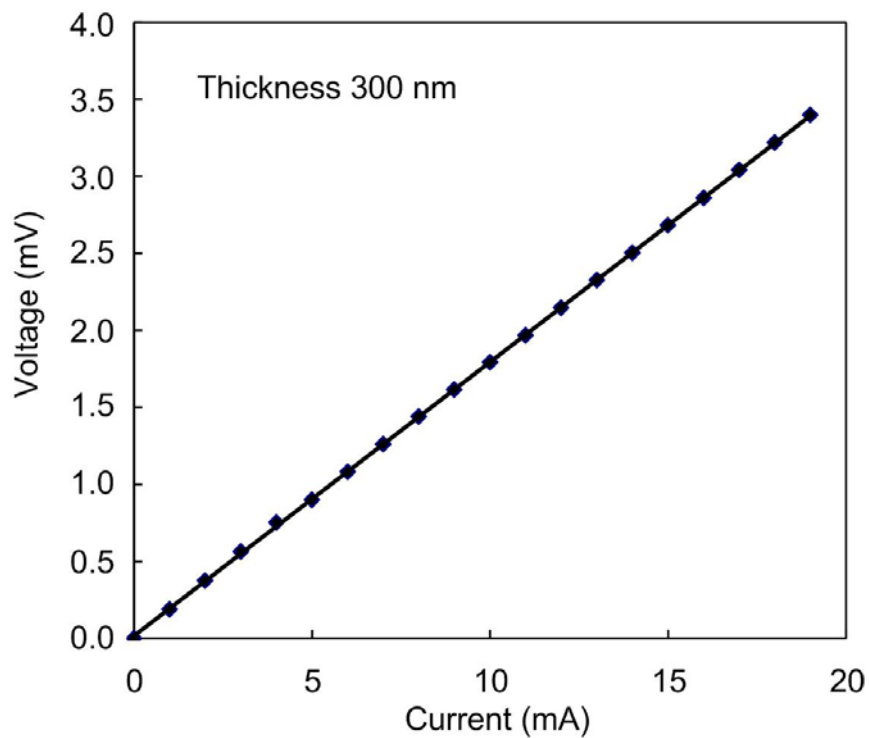


Fig. 3-11 Measured I - V curve for a sample of parylene-C film.

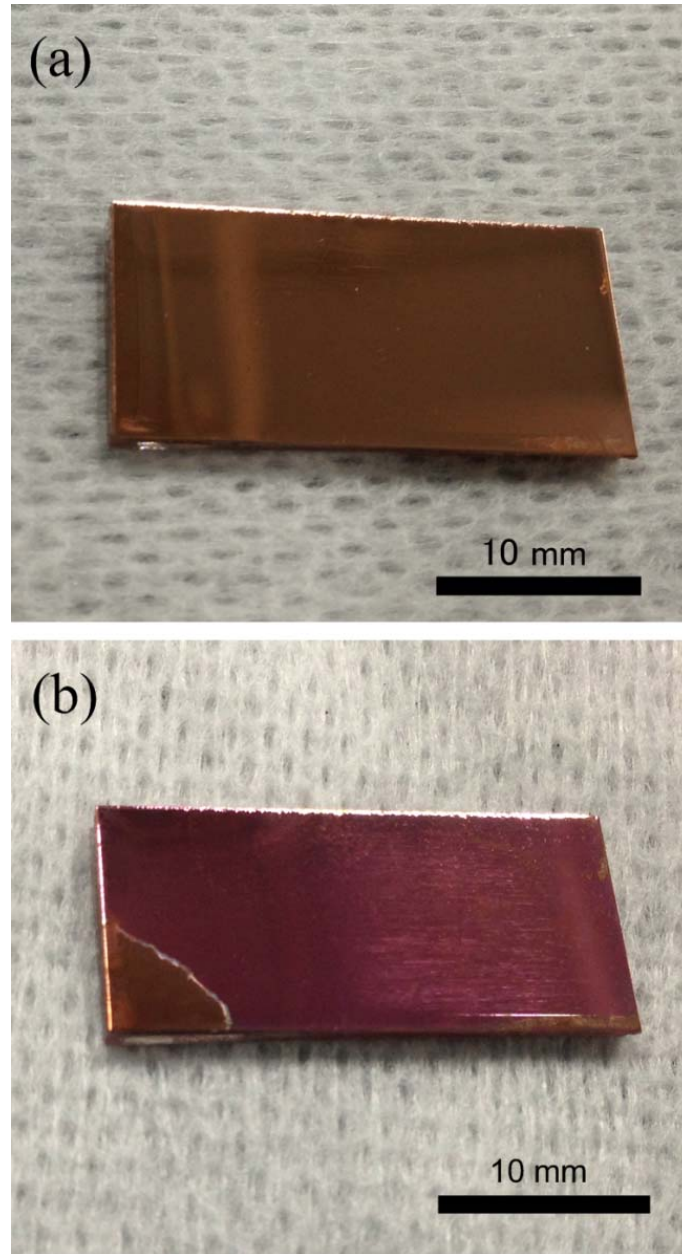


Fig. 3-12 (a) The photograph of flat polished Cu sheet. (b) The photograph of parylene coated on Cu sheet. One corner of the parylene film was peeled off in order to distinguish the Cu sheet from the color.

The reason why parylene-C film in nanoscale thickness becomes conductive is mainly due to the dielectric breakdown phenomenon. For parylene film with the thickness larger than $1\mu\text{m}$, the breakdown voltage could be estimated by the equation, $V_{\text{bd}}=1.89\times(th)^{0.45}$, based on the experimental data [13], where V_{bd} is the breakdown

Chapter 3. Copper-parylene core-shell NSF

voltage in volt, and th is the thickness in micrometer. According to this equation, the breakdown voltage of 300 nm thick parylene film could be 1.10 V. However, the crystal size at low thickness is smaller than that at high thickness [14], and the voids and discontinuities which may exist in the material will have an effect as the decrease of film thickness. Therefore, the thickness in nanoscale will further decrease the breakdown voltage.

In order to quantitatively measure the breakdown voltage of parylene-C film, a thin parylene-C film (~300 nm thickness) was coated on a flat polished Cu sheet (**Fig. 3-12(a) and (b)**). The morphology of the parylene film was measured by SEM (**Fig. 3-13**). As shown in **Fig. 3-14**, the red light from the light-emitting diode shows that the parylene film becomes conductive under the voltage of 3V. The according electric circuit is shown in **Fig. 3-15**.

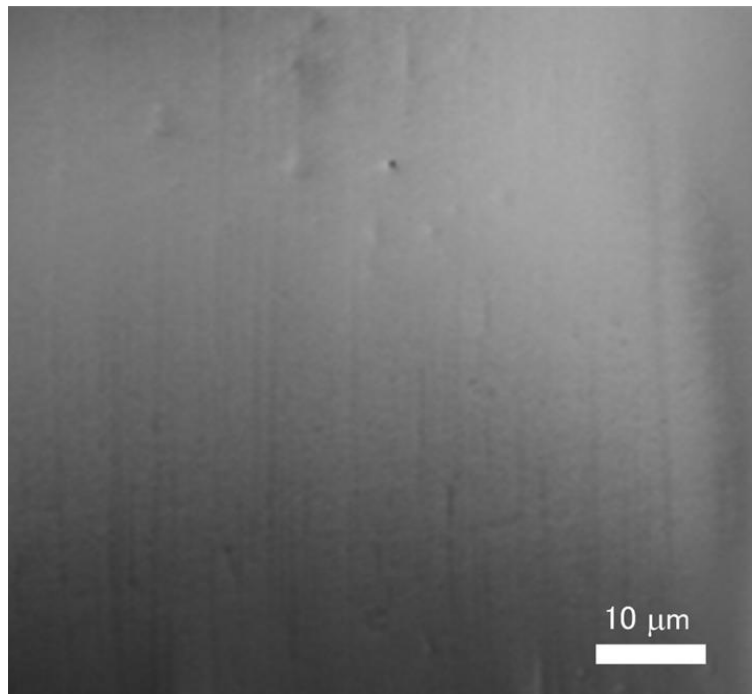


Fig. 3-13 SEM images of parylene film.

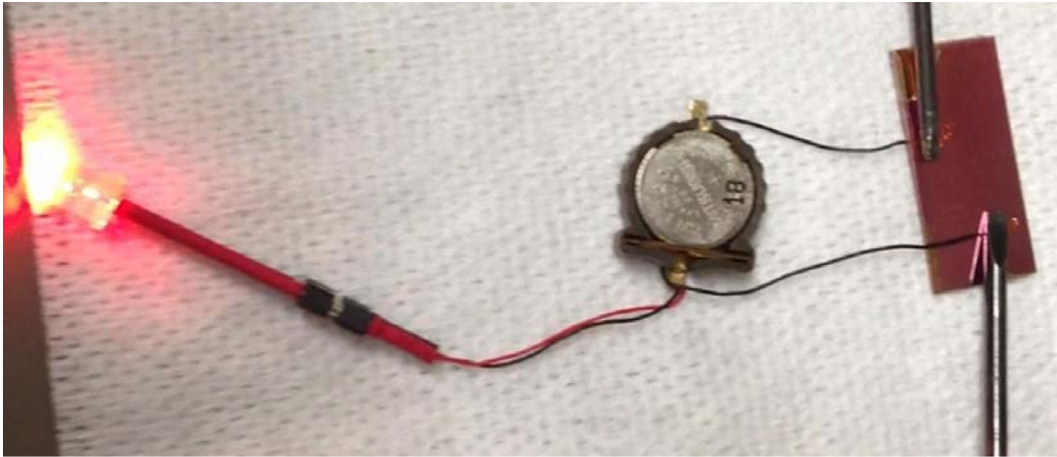


Fig. 3-14 Light-emitting diode to show electrical conductivity of thin parylene film.

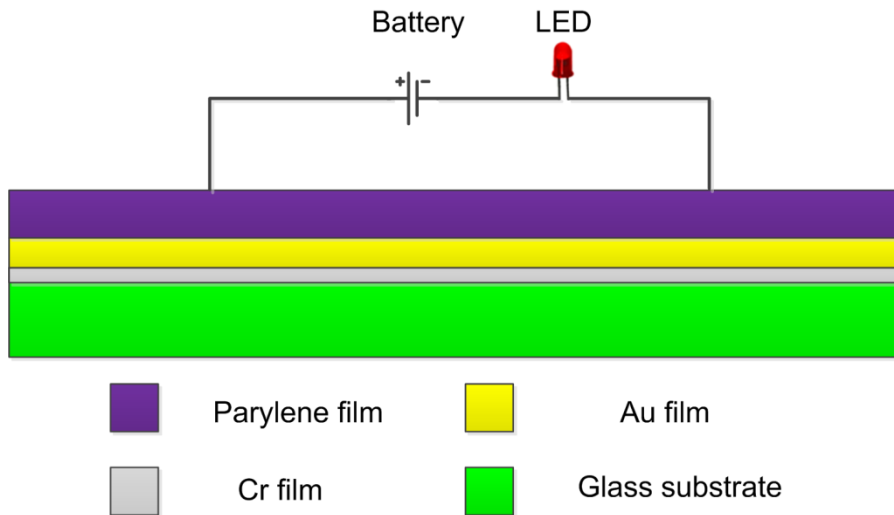


Fig. 3-15 The electric circuit for the **Fig. 3-14**.

Fig. 3-16 shows the measured dielectric breakdown for the parylene film. Here, a two-point measurement was carried out. DC voltage from 0 to 1 V was applied by a constant voltage source, and the current was measured by a current meter. The breakdown voltage was measured to be 0.55 V.

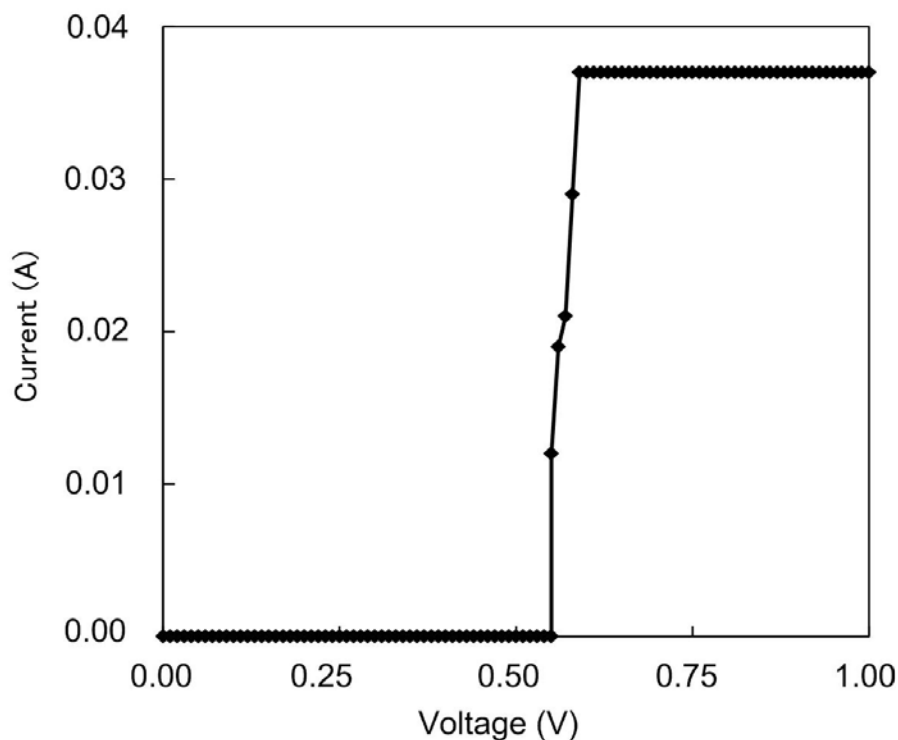


Fig. 3-16 Measured dielectric breakdown for the parylene-C film with ~300 nm thickness.

3.3.2 The performance of copper-parylene core-shell NSF

The fabrication procedure of the copper-parylene core-shell NSFs is outlined in **Fig. 3-17**. At first, copper NWs were grown on Au/Cr/glass substrates by template-assisted electrodeposition method. After etching the PC template, a thin layer of parylene-C was evenly deposited on the copper NWs to enhance the adhesive ability of NSFs. Scanning electron microscopy (SEM) image of the copper NW arrays with the average diameter of 150 nm (**Fig. 3-18**) indicates that most of the NWs were grown vertically on the substrate but oriented in a wide range of directions. **Fig. 3-19** and **3-20** show the SEM image of copper NWs with a 100 nm parylene coating and with a 200 nm parylene coating, respectively. Clearly, the grown copper NWs sustain their high aspect ratio without aggregation, partly due to the high Young's modulus of the copper (~110 GPa).

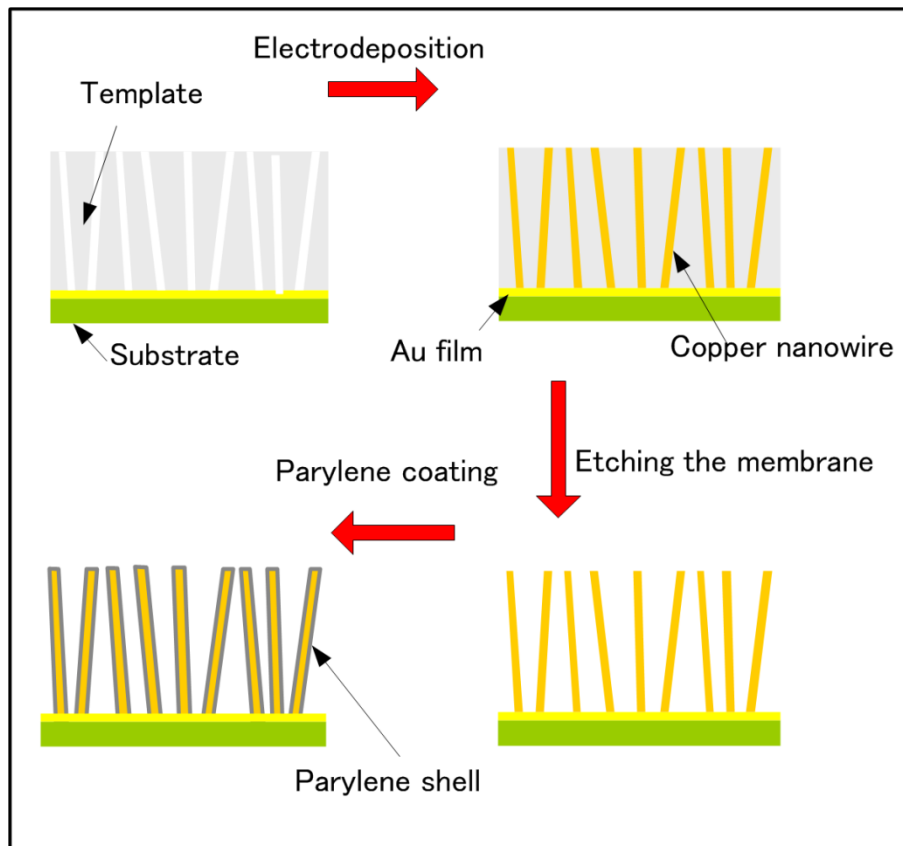


Fig. 3-17 Schematics of the fabrication process.

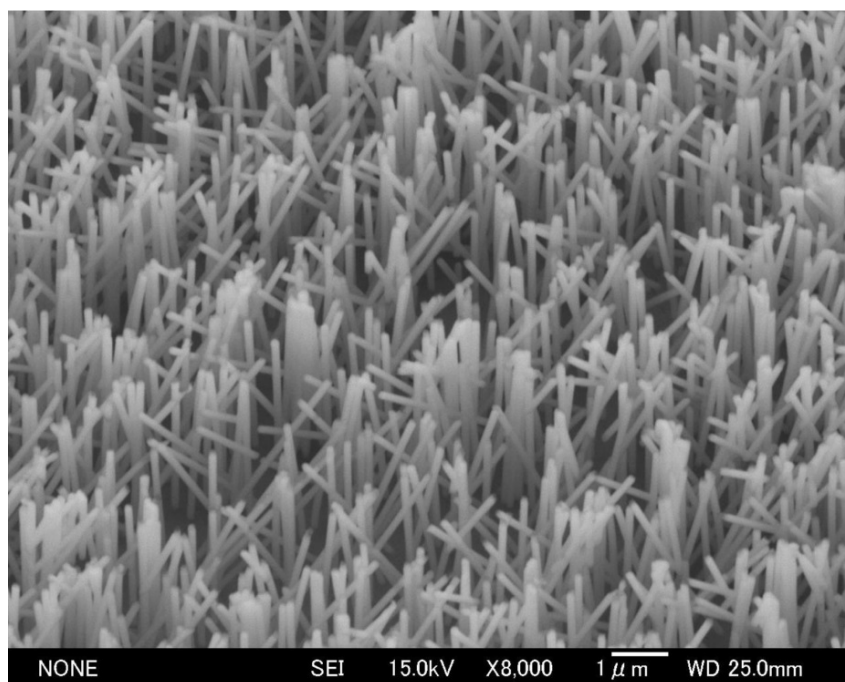


Fig. 3-18 SEM images of copper NWs without parylene coating.

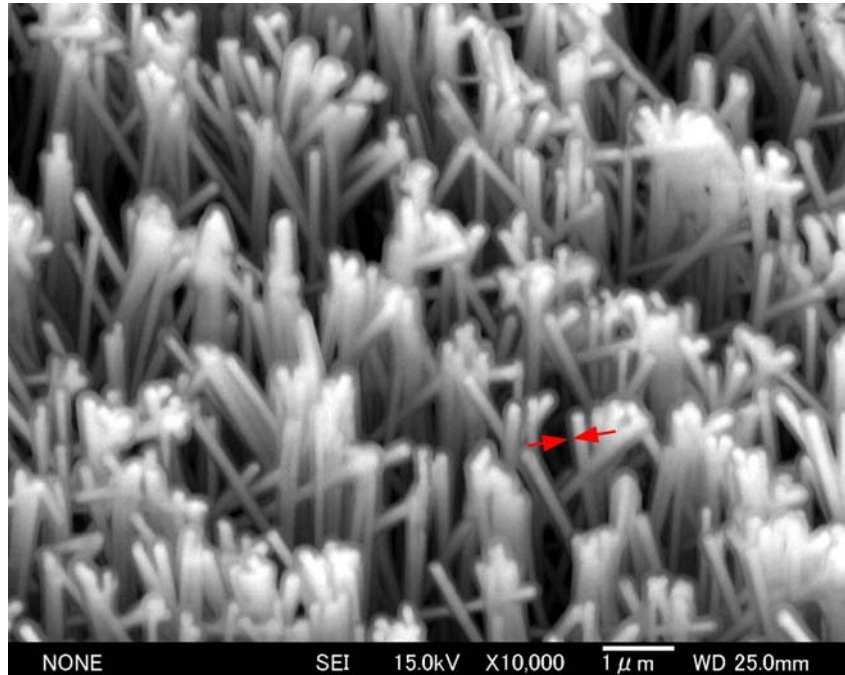


Fig. 3-19 SEM images of copper NWs with 100 nm parylene coating. The red arrow indicates the parylene shell.

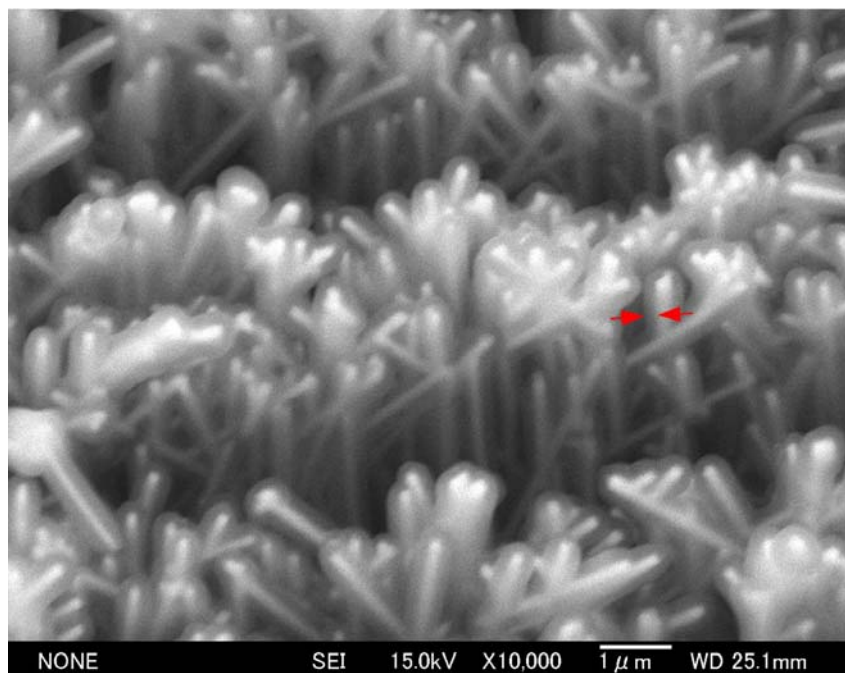


Fig. 3-20 SEM images of copper NWs with 200 nm parylene coating. The red arrow indicates the parylene shell.

To characterize the properties of core-shell NSF, we first measured the adhesive

Chapter 3. Copper-parylene core-shell NSF

strength and relative electrical resistance as a function of NW length (5, 10 and 20 μm). All the samples in this test have a parylene shell (100 nm thickness) and experienced a preload of 9.8 N. As can be seen in **Fig. 3-21**, both shear and normal adhesive can be realized at the same time, which is different from other kinds of core/shell-type connectors [15, 16]. Moreover, the adhesive strength is strongly affected by the length of the NWs. The maximum shear and normal strengths were obtained when the length was 10 μm . When $L < 10 \mu\text{m}$, the NWs sustained their high aspect ratio and the neighboring NWs did not contact with each other (**Fig. 3-23**), therefore the contact area is directly proportional to the NW length (**Fig. 3-26(c)**). However, when the NW length is as large as 20 μm , the NWs tend to collapse and the neighboring NWs contact with each other (**Fig. 3-25**), which leads to the reduction of contact area (**Fig. 3-26(c)**).

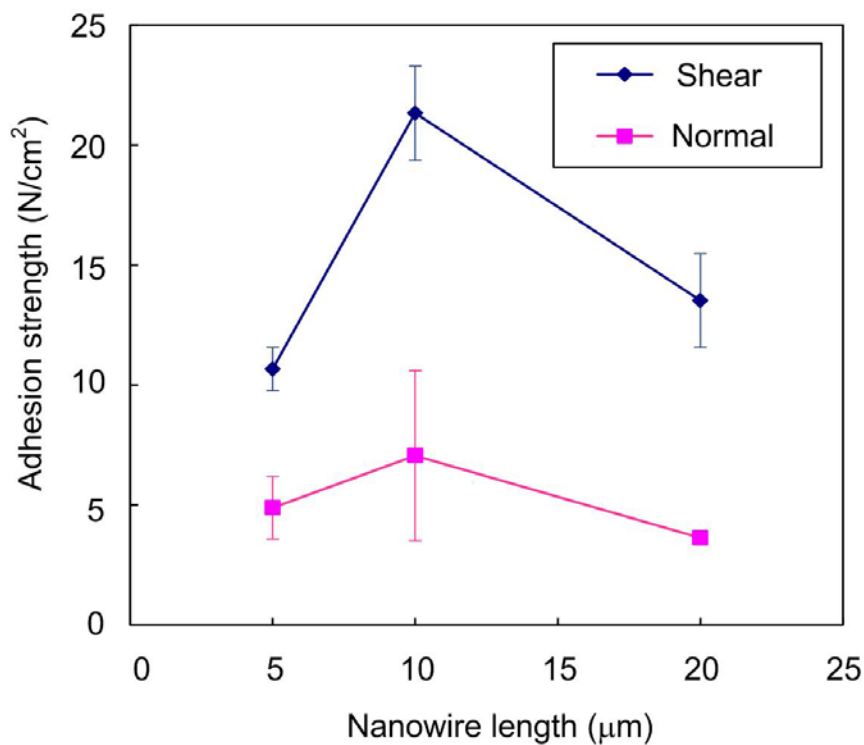


Fig. 3-21 Adhesive strength as a function of nanowire length. The preload is 9.8 N and the thickness of parylene shell is 100nm.

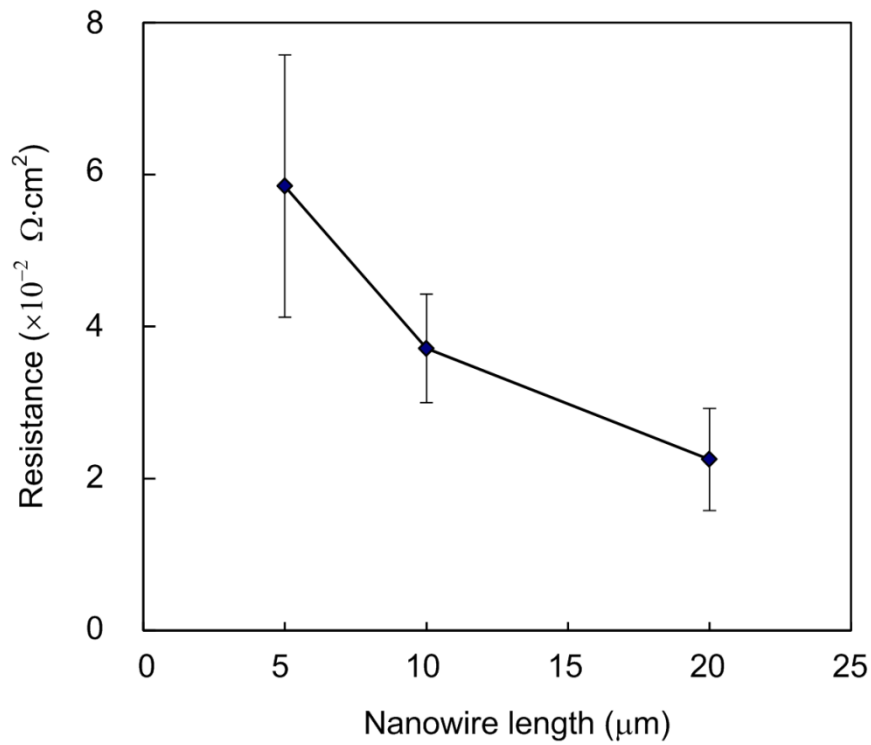


Fig. 3-22 Electrical resistance of NSFs as a function of nanowire length. The preload is 9.8 N and the thickness of parylene shell is 100nm.

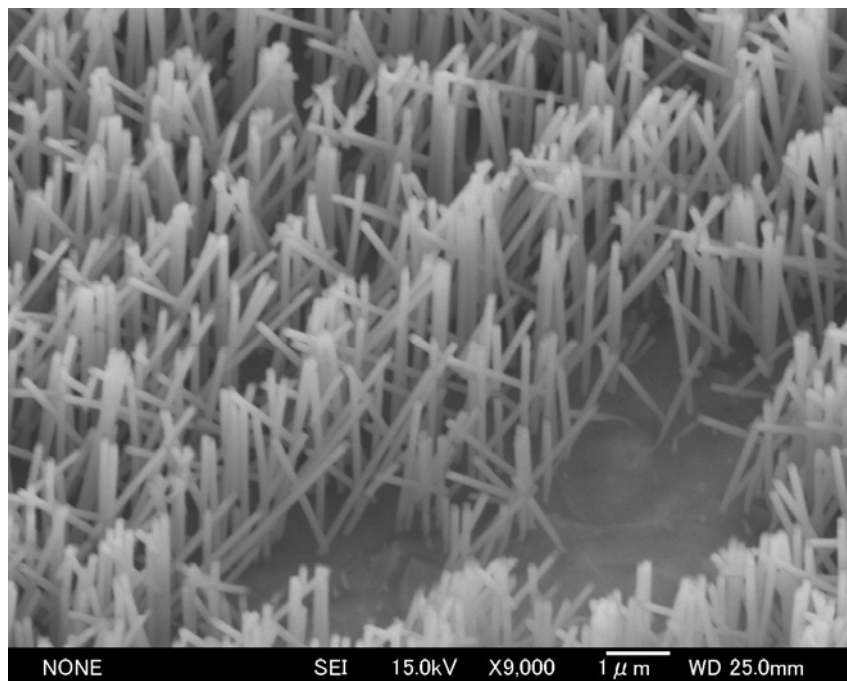


Fig. 3-23 Side-view SEM images of nanowire arrays with the length of 5 μm .

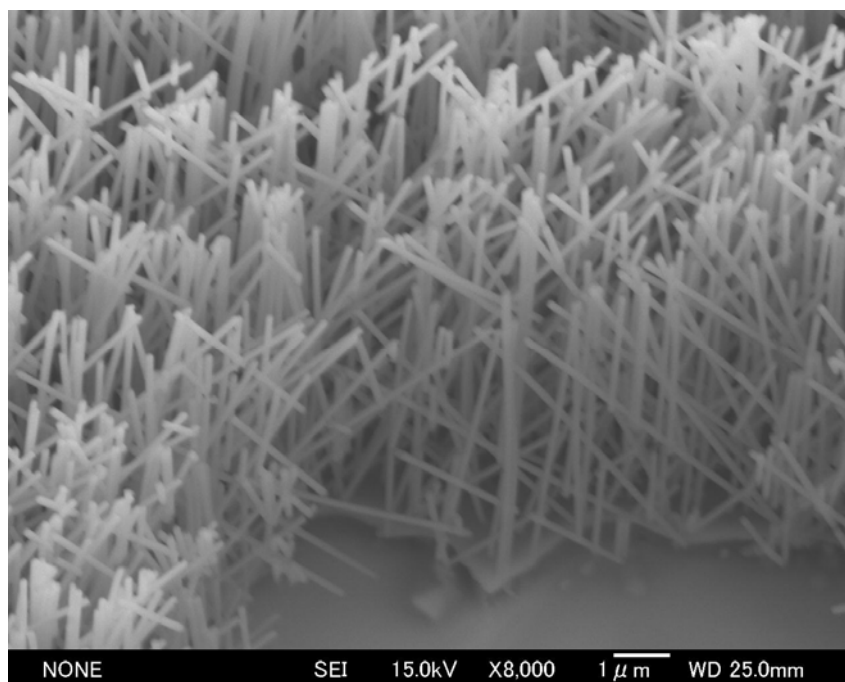


Fig. 3-24 Side-view SEM images of nanowire arrays with the length of 10 μm .

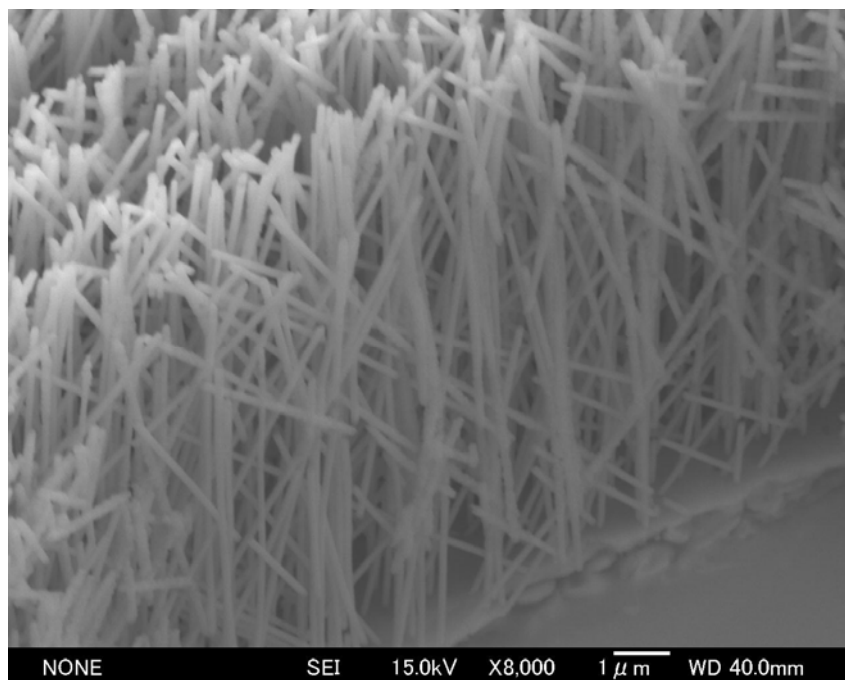


Fig. 3-25 Side-view SEM images of nanowire arrays with the length of 20 μm .

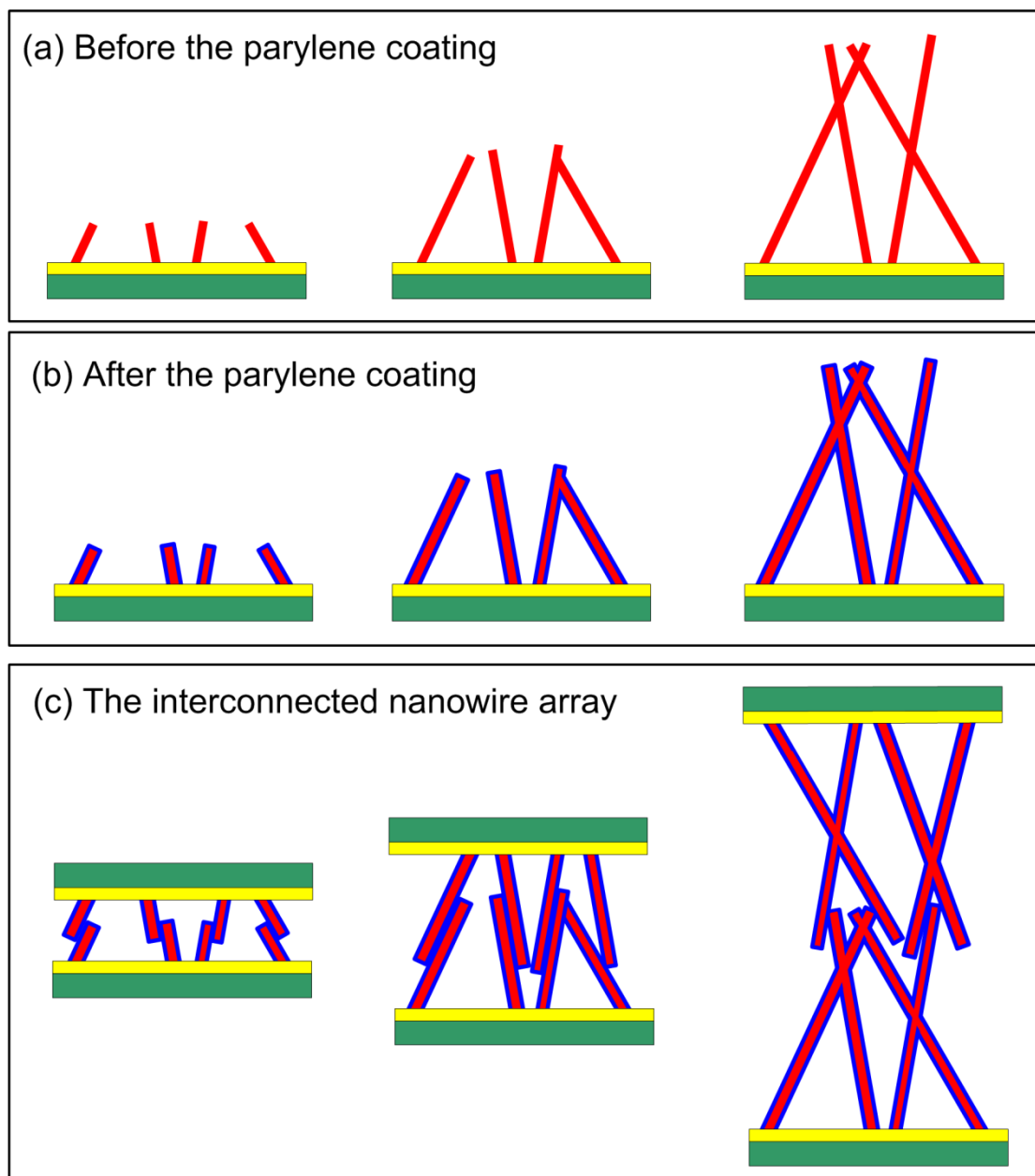


Fig. 3-26 (a) Illustration of nanowire arrays before the parylene coating with the length of 5, 10, 20 μm. (b) Illustration of nanowire arrays after the parylene coating with the length of 5, 10, 20 μm. (c) Illustration of interconnected nanowire array with the length of 5, 10, 20 μm.

The electrical resistance is also strongly affected by the length of NWs. Specifically, longer NW length results in smaller electrical resistance (**Fig. 3-22**). As can be seen in **Fig. 3-23, 3-24, 3-25, and 3-26**, the interconnection of neighboring NWs increases as the length of NWs increases, and it can not be changed after the

Chapter 3. Copper-parylene core-shell NSF

parylene coating. The interconnected neighboring NWs served as connect in parallel in the electrical connection, which lead to the reduction of resistance.

Besides the nanowire length, the adhesive strength and electrical resistance is also affected by the parylene thickness. The samples with the same nanowire length (10 μm) and the same preload (9.8 N) are used in the test. As can be seen in **Fig. 3-27**, the adhesive properties strongly depend on the thickness of parylene shell. Specifically, weak adhesive strengths ($\sim 0.99 \text{ N/cm}^2$ in shear and $\sim 0.57 \text{ N/cm}^2$ in normal directions) are obtained from the pristine copper NWs (**Fig. 3-27**). The adhesive strength is dramatically enhanced by the application of the parylene shell. When the thickness of parylene shell is 150 nm, the maximum shear adhesive strengths ($\sim 24.97 \text{ N/cm}^2$) is obtained. There is no significant difference in normal adhesive strength for the parylene thickness of 100 nm and 150 nm, and the maximum normal adhesive strength is $\sim 11.08 \text{ N/cm}^2$. This significant enhancement in adhesive is attributed to the higher surface compliance of parylene shell, enabling conformal contact with increased contact area between the interpenetrating NWs [16]. When the thickness of parylene shell further increases, the adhesive strengths decrease. This trend is attributed to the higher filling factor for thicker parylene shells (**Figs. 3-18, 3-19 and 3-20**). When the thickness of the parylene shell increases to 250 nm (**Fig. 3-29**), almost no spare space exists between the neighboring NWs. Hence, the interconnected mode changes from “wire-wire” to “tip-tip” when the thickness of parylene shell increases, which results in the reduction of adhesive strengths. The electrical properties of NSFs are also affected by the parylene shell thickness. It can be seen from **Fig. 3-28** that larger parylene shell thickness results in larger electrical resistance of the NSFs. This trend is attributed to the poor electrical conductivity of parylene.

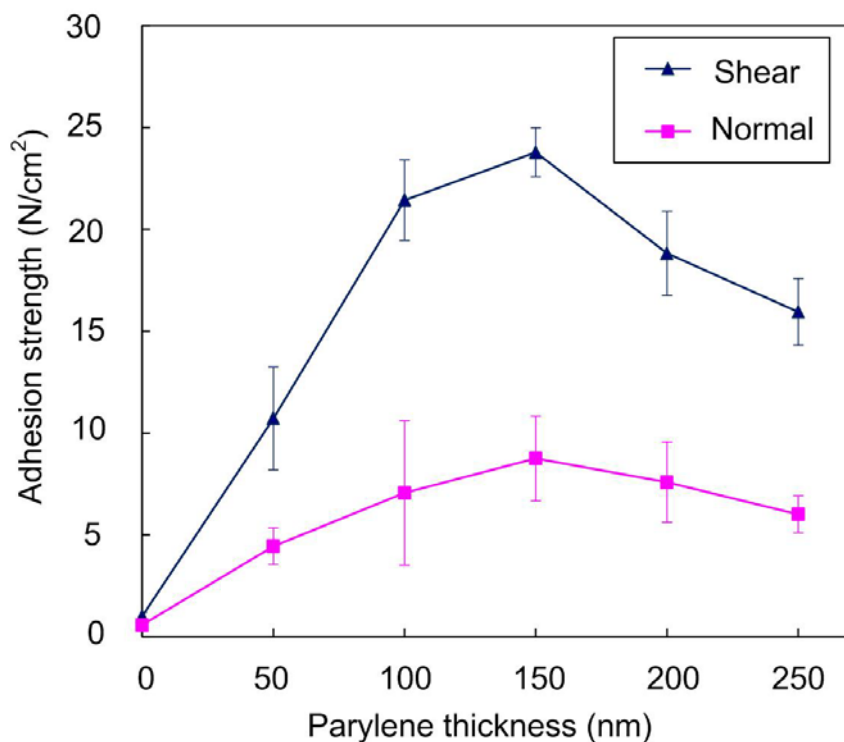


Fig. 3-27 Adhesive strength of NSFs as a function of parylene thickness. The preload is 9.8N and the length of nanowire array is 10 μm .

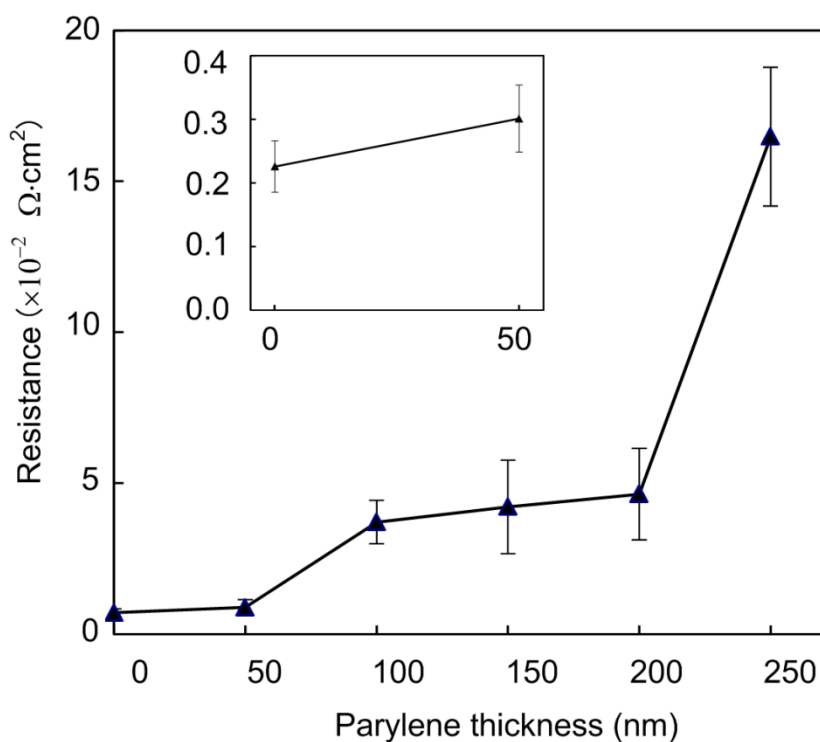


Fig. 3-28 Electrical resistance of NSFs as a function of parylene thickness. The preload is 9.8N and the length of nanowire array is 10 μm .

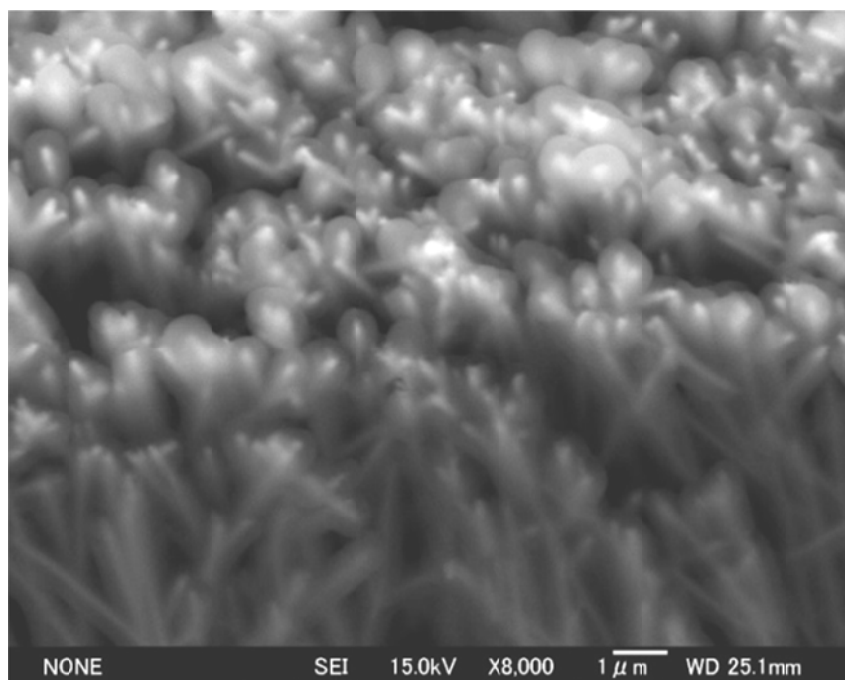


Fig. 3-29 SEM image of core-shell nanowire array with 250 nm parylene shell.

To examine the effect of preload on the adhesive and electrical properties of core-shell NSF, two NSF samples were brought into interconnection at the preload of 4.9, 9.8 and 19.6N. A monotonic increase in the normal adhesive strength and decrease in electrical resistance is observed with the increase of preload force (**Fig. 3-30** and **3-31**). This phenomenon is just as expected because the higher preload force leads to larger contact area between the NWs. However, no increase in the shear adhesive was observed when the preload increases from 9.8 N to 19.6N. This phenomenon is attributed to the poor adhesive of electrodeposited copper NWs on the Au seed layer. As can be seen in **Fig. 3-32**, NW arrays detached from the Au seed layer after the adhesive test.

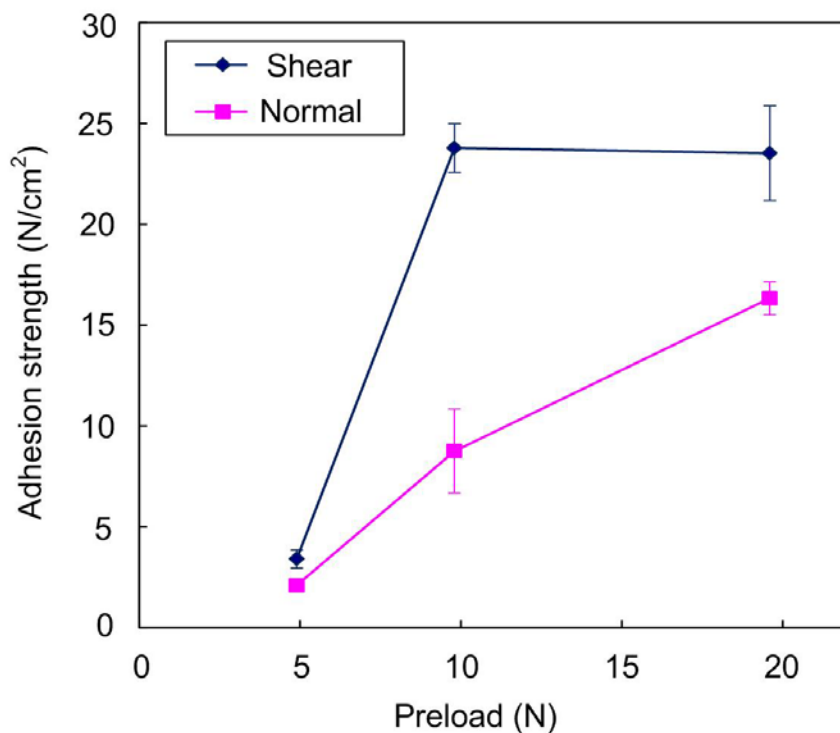


Fig. 3-30 Adhesive strength of NSFs as a function of preload. The thickness of parylene shell is 150 nm and the length of nanowire array is 10 μm .

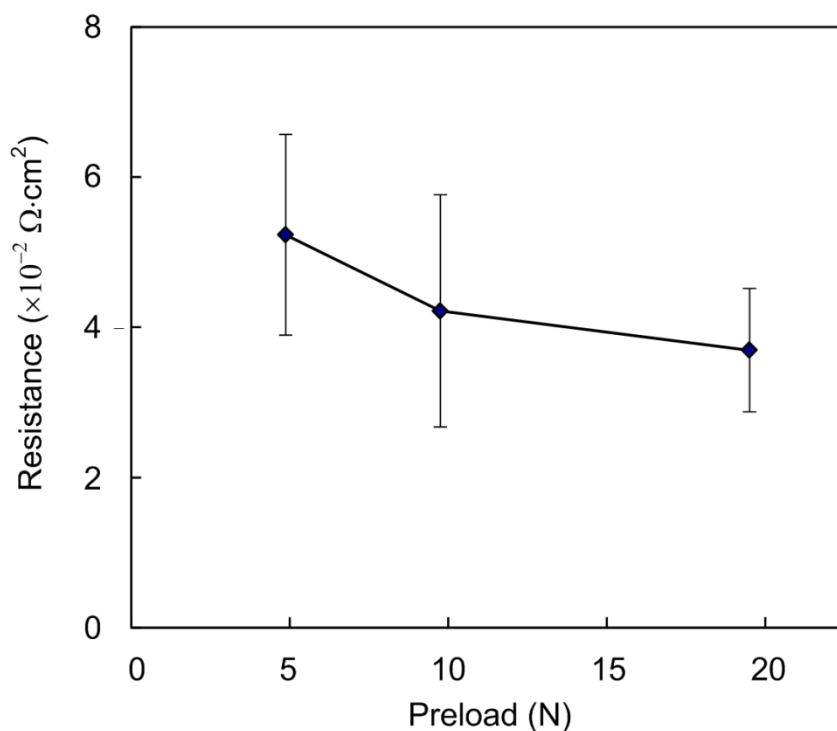


Fig. 3-31 Electrical resistance of NSFs as a function of preload. The thickness of parylene shell is 150 nm and the length of nanowire array is 10 μm .

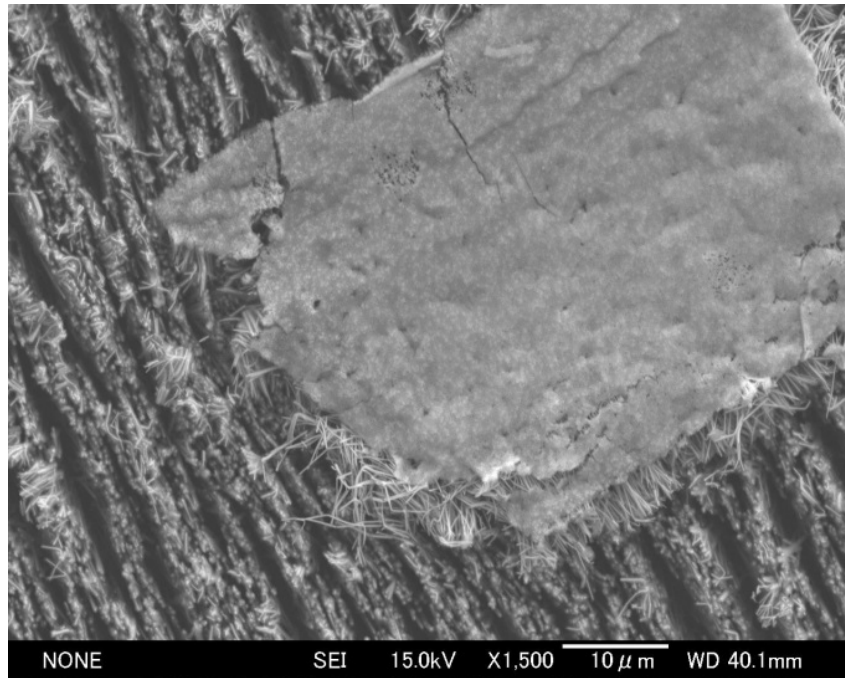


Fig. 3-32 SEM image of the nanowire array after the debonding. The preload is 19.6N, the thickness of parylene shell is 150nm, and the length of nanowire is 10 μm.

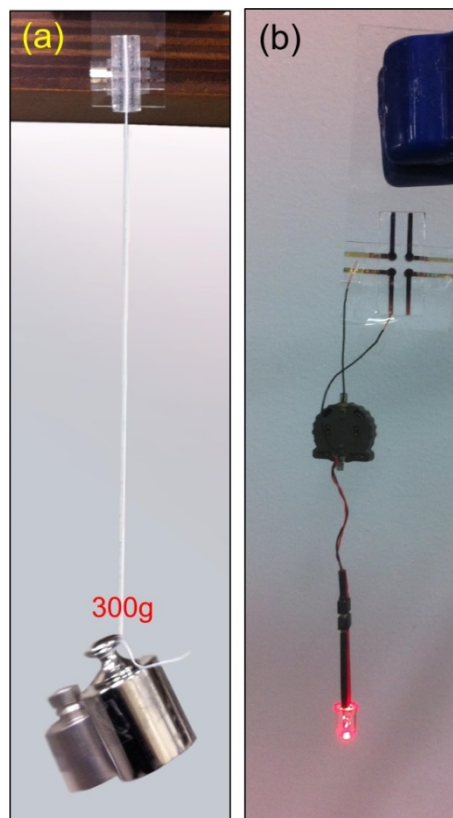


Fig. 3-33 (a) Photo showing a weight of 300g hanging on the interconnected copper NSF. (b) Light-emitting diode suspended by the NSF to show electrical conductivity.

Chapter 3. Copper-parylene core-shell NSF

An example of the strong bonding achieved is shown in **Fig. 3-33(a)** in which the copper-parylene core-shell NSFs with the surface area of $\sim 3.14 \times 4 \text{ mm}^2$ enables 300g of weight to be hung without failure in shear direction. As shown in **Fig. 3-33(b)**, the red light from the light-emitting diode shows that the core-shell NSFs are conductive.

3.4 Theory analysis

3.4.1 Calculation of Hamaker constant

The Hamaker constants of common materials can be found from many literatures, and the Hamaker constants of special materials are usually estimated from Lifshitz theory. According to Lifshitz theory, the Hamaker constant of parylene-C can be determined by dielectric constant ε and refractive index n , and it can be formulated as [17]:

$$A = A_{v=0} + A_{v>0} = \frac{3}{4} kT \left(\frac{\varepsilon_1 - \varepsilon_3}{\varepsilon_1 + \varepsilon_3} \right)^2 + \frac{3h\nu_e}{16\sqrt{2}} \frac{(n_1^2 - n_3^2)^2}{(n_1^2 + n_3^2)^{3/2}} \quad (3-1)$$

where k is the Boltzmann constant ($1.38 \times 10^{-23} \text{ J}\cdot\text{K}^{-1}$), T is the absolute temperature, h is the Planck constant ($6.63 \times 10^{-34} \text{ J}\cdot\text{s}$), and ν_e is the material's absorption frequency ($3 \times 10^{15} \text{ s}^{-1}$) [17]. The dielectric constant and refractive index of parylene-C and air are listed in **Table 3.1**:

Table 3.1 The parameters used to determine the Hamaker constant

ε_1 [12]	ε_3 [17]	n_1 [12]	n_3 [17]	A_{pa}
3.15	1	1.639	1	$10.678 \times 10^{-20} \text{ J}$

The Hamaker constant between copper and parylene-C $A_{\text{pa-cu}}$ can be obtained

approximate through the combining relation, which is given by [17]:

$$A_{pa-cu}=(A_{cu}\times A_{pa})^{0.5} \quad (3-2)$$

3.4.2 The van der Waals force between two core-shell nanowires

In order to further understand the interlocking behavior presented here, a simple theoretical model is adopted to quantitatively describe the measured adhesive forces. Once the nanowires are brought into interconnection at a uniformed preload, the VDW forces between the interconnected nanowires are assumed to contribute to the bonding.

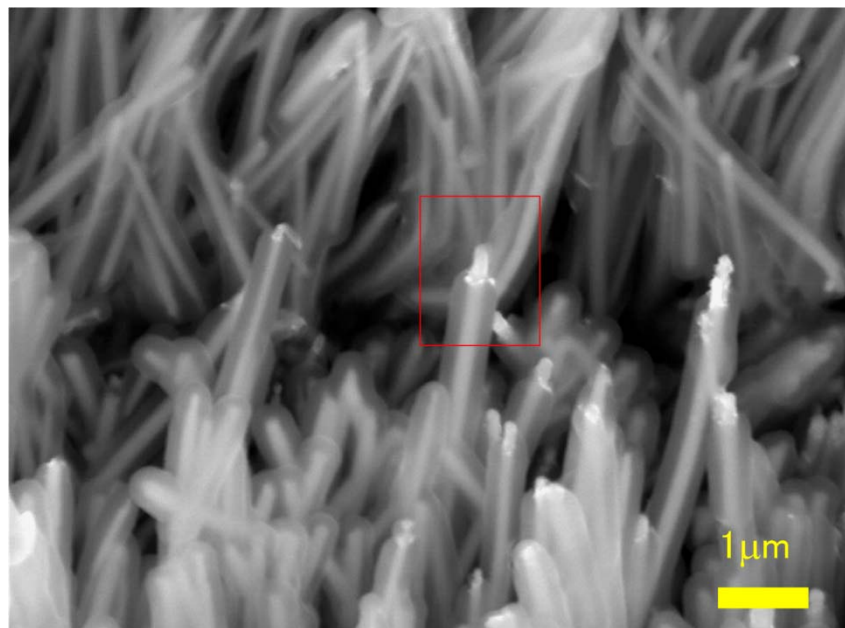


Fig. 3-34 SEM images of interconnected NWs. The parylene thickness is 150 nm; the preload is 9.8N and the length of nanowire array is 10 μm.

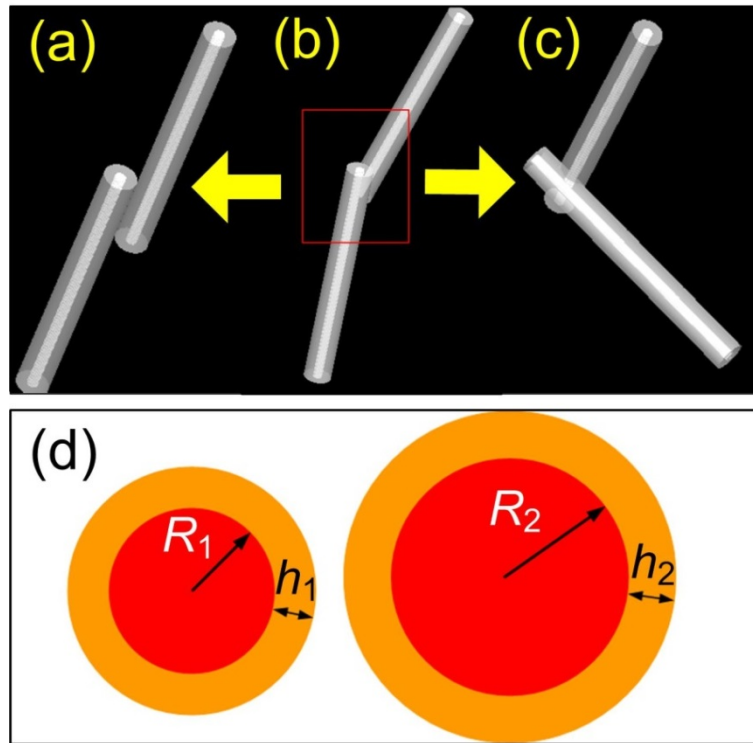


Fig. 3-35 (a) Parallel-contacting cylinders. (b) Interconnected cylinders with arbitrary angle. (c) Perpendicular-contacting cylinders. (d) The cross-section of two core-shell cylinders.

As shown in **Fig. 3-34**, the interconnected nanowires were crossed at arbitrary angles. Considering two extreme interconnection scenarios between two cylinders, arbitrary interconnection (**Fig. 3-35(b)**) can be considered as either in parallel (**Fig. 3-35(a)**) or perpendicular (**Fig. 3-35(c)**) configuration with each other.

Until now, the expressions for the VDW forces between two core-shell cylinders are not available. On the other hand, based on the assumption of additivity, the VDW expressions between two spherical shells have been presented by R. Tadmor [18]. Here, the VDW expression for core-shell cylinder mode was derived through the same method. In this study, the interconnected core-shell NWs have the same core radius and the same shell thickness. However, in order to obtain more general result, the geometry of the interconnected core-shell cylinders was assumed to be different. As can be seen in **Fig. 3-35(d)**, one core-shell cylinder has a core radius of R_1 and

Chapter 3. Copper-parylene core-shell NSF

shell thickness of h_1 , and another core-shell cylinder has a core radius of R_2 and shell thickness of h_2 .

In the case of two interacting cylinders, let us suppose cylinder 2 is composed of one core (core 2) and one shell (shell 2). Then, based on the assumption, the total interaction energy per unit length between the two cylinders can be formulated as:

$$E(\text{cylinder}_1, \text{cylinder}_2) = E(\text{cylinder}_1, \text{core}_2) + E(\text{cylinder}_1, \text{shell}_2) \quad (3-3)$$

where $E(x, y)$ is the interaction energy between a geometrical object x and a geometrical object y and the indexes 1 and 2 can be reversed. Then, based on the equation translation, we can get

$$E(\text{cylinder}_1, \text{shell}_2) = E(\text{cylinder}_1, \text{cylinder}_2) - E(\text{cylinder}_1, \text{core}_2) \quad (3-4)$$

Moreover, the interaction energy per unit length between one cylinder core and one cylinder shell can be derived through simply change the name of cylinder 1 to core 1 in equation (3-4):

$$E(\text{core}_1, \text{shell}_2) = E(\text{core}_1, \text{cylinder}_2) - E(\text{core}_1, \text{core}_2) \quad (3-5)$$

After the equation translation, we can find that on the right side of the equation there is a simple mathematic calculation of two energies of interacting cylinders. Because there exists specific expressions for the energy of interacting cylinders [17], the unknown expression of the energy between one cylinder and one shell can be calculated through the mathematic calculation in equation (3-4) and then get a specific expression.

Furthermore, let us suppose that cylinder 1 is composed of one core (core 1) and one shell (shell 1), cylinder 2 is composed of one core (core 2) and one shell (shell 2).

It is easy to derive that

$$E(\text{cylinder}_1, \text{cylinder}_2) = E(\text{core}_1, \text{core}_2) + E(\text{core}_1, \text{shell}_2) + E(\text{shell}_1, \text{core}_2) + E(\text{shell}_1, \text{shell}_2) \quad (3-6)$$

Chapter 3. Copper-parylene core-shell NSF

Then, based on the equation translation, we can get

$$E(\text{shell}_1, \text{shell}_2) = E(\text{cylinder}_1, \text{cylinder}_2) - E(\text{core}_1, \text{core}_2) - E(\text{core}_1, \text{shell}_2) - E(\text{shell}_1, \text{core}_2) \quad (3-7)$$

Then, through substituting equation (3-5) into equation (3-7), we can further derived that

$$E(\text{shell}_1, \text{shell}_2) = E(\text{cylinder}_1, \text{cylinder}_2) + E(\text{core}_1, \text{core}_2) - E(\text{core}_1, \text{cylinder}_2) - E(\text{cylinder}_1, \text{core}_2) \quad (3-8)$$

The van der Waals forces, corresponds to the interaction energy, can be defined as [19]:

$$F = -dE/dD \quad (3-9)$$

Here, D is the shortest distance between the surfaces of two cylinders. Then, through substituting equation (3-5) and (3-8) into equation (3-9), we can further derived that

$$F(\text{core}_1, \text{shell}_2) = F(\text{core}_1, \text{cylinder}_2) - F(\text{core}_1, \text{core}_2) \quad (3-10)$$

and

$$F(\text{shell}_1, \text{shell}_2) = F(\text{cylinder}_1, \text{cylinder}_2) + F(\text{core}_1, \text{core}_2) - F(\text{core}_1, \text{cylinder}_2) - F(\text{cylinder}_1, \text{core}_2) \quad (3-11)$$

When two solid cylinders have a radius of R_1+h_1 and R_2+h_2 and are at a distance D apart, the van der Waals force F in parallel-contacting can be formulated as [19]:

$$F(R_1 + h_1, R_2 + h_2, D) = \frac{A \cdot l}{8\sqrt{2}D^{2.5}} \left(\frac{(R_1 + h_1)(R_2 + h_2)}{R_1 + R_2 + h_1 + h_2} \right)^{0.5} \quad (3-12)$$

Moreover, the van der Waals force F in perpendicular-contacting can be formulated as [19]:

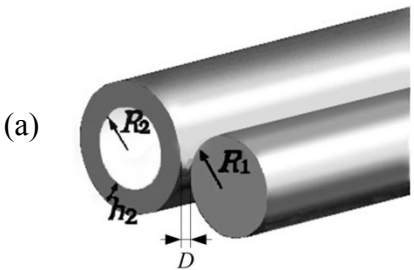
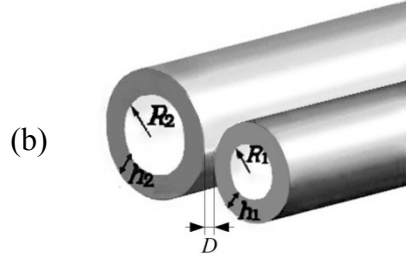
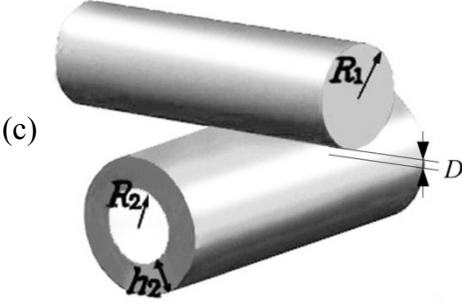
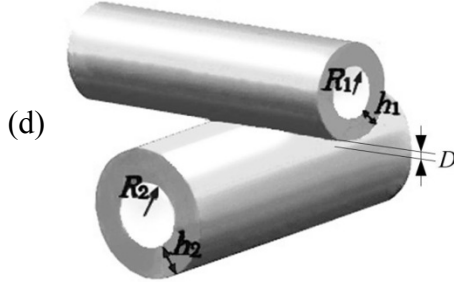
$$F(R_1 + h_1, R_2 + h_2, D) = \frac{A}{6D^2} ((R_1 + h_1)(R_2 + h_2))^{0.5} \quad (3-13)$$

Chapter 3. Copper-parylene core-shell NSF

where A is the Hamaker constant (corresponding to the material) and l is the overlapped length. Based on equation (3-10), (3-11), (3-12) and (3-13), the expression of VDW forces in some limited cases were obtained and summarized in **Table 3.2**.

It should be noted that D is defined as the shortest distance between the surfaces of interconnected objects in **Table 3.2** and the numerical value of D may be changed during different interconnection cases.

Table 3.2 the VDW forces between some limited geometries.

<p style="text-align: center;">cylinder and cylinder shell in parallel (per unit length)</p> <div style="text-align: center;">  <p>(a)</p> </div> $F = \frac{A}{8\sqrt{2}D^{2.5}} \left(\frac{R_1(R_2+h_2)}{R_1+R_2+h_2} \right)^{0.5} - \frac{A}{8\sqrt{2}(D+h_2)^{2.5}} \left(\frac{R_1R_2}{R_1+R_2} \right)^{0.5}$	<p style="text-align: center;">Two cylinder shells in parallel (per unit length)</p> <div style="text-align: center;">  <p>(b)</p> </div> $F = \frac{A}{8\sqrt{2}D^{2.5}} \left(\frac{(R_1+h_1)(R_2+h_2)}{R_1+R_2+h_1+h_2} \right)^{0.5} + \frac{A}{8\sqrt{2}(D+h_1+h_2)^{2.5}} \left(\frac{R_1R_2}{R_1+R_2} \right)^{0.5}$ $- \frac{A}{8\sqrt{2}(D+h_2)^{2.5}} \left(\frac{(R_1+h_1)R_2}{R_1+h_1+R_2} \right)^{0.5} - \frac{A}{8\sqrt{2}(D+h_1)^{2.5}} \left(\frac{R_1(R_2+h_2)}{R_1+R_2+h_2} \right)^{0.5}$
<p style="text-align: center;">cylinder and cylinder shell in perpendicular</p> <div style="text-align: center;">  <p>(c)</p> </div> $F = \frac{A\sqrt{R_1(R_2+h_2)}}{6D^2} - \frac{A\sqrt{R_1R_2}}{6(D+h_2)^2}$	<p style="text-align: center;">Two cylinder shells in perpendicular</p> <div style="text-align: center;">  <p>(d)</p> </div> $F = \frac{A\sqrt{(R_1+h_1)(R_2+h_2)}}{6D^2} + \frac{A\sqrt{R_1R_2}}{6(D+h_1+h_2)^2}$ $- \frac{\sqrt{(R_1+h_1)R_2}}{6(D+h_2)^2} - \frac{\sqrt{R_1(R_2+h_2)}}{6(D+h_1)^2}$

The VDW forces between two core-shell cylinders can be formulated as:

$$F_{VDW} = F(\text{shell}_1, \text{shell}_2) + F(\text{core}_1, \text{shell}_2) + F(\text{shell}_1, \text{core}_2) + F(\text{core}_1, \text{core}_2) \quad (3-14)$$

Chapter 3. Copper-parylene core-shell NSF

which can be obtained through substituting the equations (a) and (b), or (c) and (d) in **Table 3.2**, and equation (3-12) or (3-13) into equation (3-14). Although the writing equation for core-shell cylinder is redundant and lengthy, the calculation is easy with the help of computer.

As shown in **Fig. 3-34**, the radius of copper nanowire is $R \approx 75$ nm, the thickness of parylene is $h \approx 150$ nm, and the overlapped length is $l \approx 650$ nm. Considering $D=D_0=0.4$ nm [19], $A_{cu}=28.4 \times 10^{-20}$ J [20], $A_{pa}=10.678 \times 10^{-20}$ J, $A_{pa-cu}=17.414 \times 10^{-20}$ J, the VDW forces F_{vdw} between the parallel-contacting and perpendicular-contacting core-shell cylinders can be obtained from the equation expressions derived in this paper. The normalization by area is taken by $F_{shear}=\rho F_{vdw}$ (ρ is the effective nanowires interconnect density per area, $\approx 3 \times 10^8$ cm⁻²). After normalized by area, the shear strengths F_{shear} are calculated to be 192.906 and 7.508 N/cm² for parallel-contacting and perpendicular-contacting mode, respectively. For the normal adhesive, we assumed that Amonton's first law ($F_{friction}=\mu F_{shear}$) is effective [21]. Considering $\mu=0.369$ [22], F_{normal} is calculated to be 71.182 N/cm² for parallel-contacting cylinders, and 2.770 N/cm² for perpendicular-contacting cylinders, respectively. The results are summarized and then compared with the experimental results, as shown in **Table 3.3**.

Table 3.3 Calculated values from VDW theory and experimental results.

	Shear strength (N/cm ²)	Normal Strength (N/cm ²)
Parallel-contacting	192.906	71.182
Perpendicular-contacting	7.508	2.770
Experimental results	24.97	11.08

The measured adhesive strengths are much smaller than the calculated value for parallel-contacting core-shell cylinders but larger than the calculated value for perpendicular-contacting core-shell cylinders. This trend can be explained by 1) the

actual contact was a mixture of parallel- and perpendicular-contacting cylinder modes. The calculation of parallel-contacting cylinders provided an upper limit, while the adhesive for perpendicular-contacting cylinders offered the lower limit. 2) the backing substrate is rather stiff, which lead to the stress concentration, thus, drastically lower the adhesive strength [23]. 3) the calculation values were based on ideal model. In fact, the contact geometry (i.e. nanowire length, radius) and the contact orientation between two nanowires are non-ideal.

3.4.3 Determination of maximum adhesive strength

Van der Waals forces between two nanowires, interfacial shear strength of parylene-C shell, the tensile strength of parylene-C material and adhesive strength of copper nanowire tearing at the base from the substrate were thought to be the factors to affect the maximum adhesive strength of the NSFs. In this study, copper nanowires were grown on Au seed layer. However, since Cu is also possible to be used as a seed layer to grow copper nanowires. Here, Cu film was used to evaluate the force of the nanowire tearing at the base from the substrate. The minimum force which will make copper nanowire detached from the Cu substrate can be estimated as:

$$F_a = \sigma_a \cdot S_{cu} = 2.1 \mu\text{N} \quad (3-15)$$

where S_{cu} is the cross-section area of copper nanowire, and $\sigma_a = 119 \text{ MPa}$ [24] is the adhesive strength measured between Cu substrate and electrodeposited Cu film.

The van der Waals forces, F_{VDW} , can be obtained from equation (3-14).

The friction force contributed to the normal adhesive strength of NSFs between two interconnected parallel nanowires can be expressed as [21]:

$$F_{\text{friction}} = \mu F_{VDW} \quad (3-16)$$

Moreover, the minimum interfacial shear force which will detach the parylene-C

Chapter 3. Copper-parylene core-shell NSF

shell from the copper core can be obtained from the following equation:

$$F_s = \tau \pi d L \quad (3-17)$$

where $\tau = 2$ MPa [16,25] is the interfacial shear stress, d the diameter of copper nanowire, and L the interconnected length.

On the other hand, the minimum force which will lead to the plastic deformation of parylene shell can be assumed as:

$$F_t = \sigma_t \cdot S_{pa} = 6.835 \mu\text{N} \quad (3-18)$$

where S_{pa} is the cross-section area of parylene-C shell, and $\sigma_t = 43$ MPa [16] is the tensile strength of parylene material.

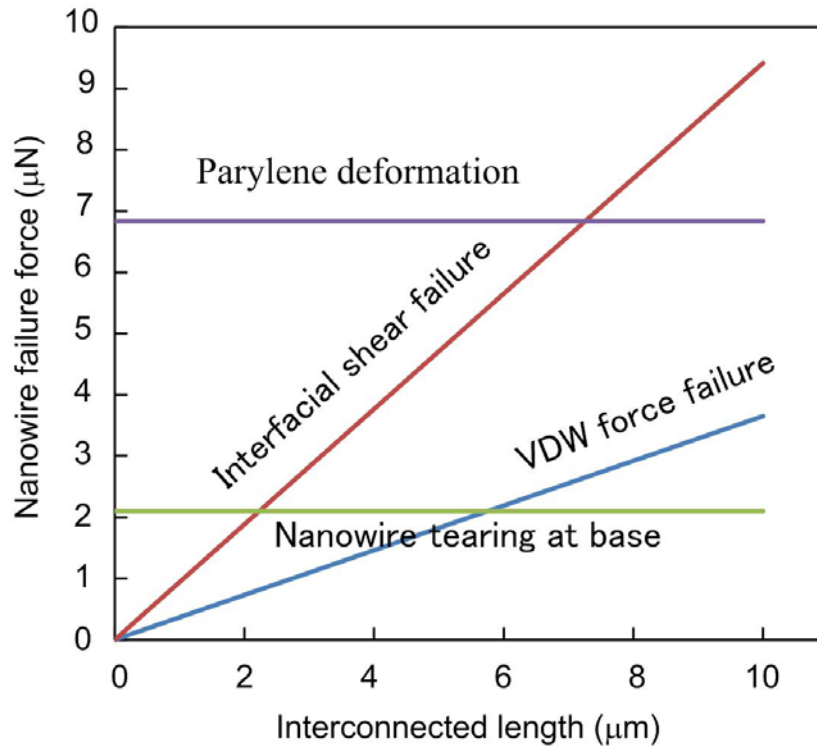


Fig. 3-36 The relationship between nanowire failure force and interconnected length under four failure modes.

Based on the above equations, the relationship between nanowire failure force and the interconnected length can be obtained, as shown in **Fig. 3-36**. When the interconnected length $L < 5.7 \mu\text{m}$, the failure mode is VDW force failure; when the

Chapter 3. Copper-parylene core-shell NSF

interconnected length $L > 5.7 \mu\text{m}$, the failure mode is nanowire tearing at base. Therefore, for the $10 \mu\text{m}$ long nanowires, the maximum adhesive strength (normal) of the NSFs is $S_{\text{max}} = \rho F_a = 630 \text{ N/cm}^2$, where ρ is the nanowires density, $\sim 3 \times 10^8$ nanowires cm^{-2} .

3.5 Summary

In summary, we designed a unique electrical surface fastener with strong adhesive based on the van der Waals forces between the two sets of identical core-shell nanowire arrays. The thin parylene-C film was found to be conductive as the thickness shrunk to nanoscale. Hence, both strong bonding and small electrical resistance were achieved at room temperature for this copper-parylene core-shell nanowire surface fastener. Uniquely, this electrical surface fastener exhibit high macroscopic adhesive strength ($\sim 25 \text{ N/cm}^2$) and low electrical resistance ($\sim 4.22 \times 10^{-2} \Omega \cdot \text{cm}^2$). Furthermore, a simple theory based on van der Waals forces was used to explain the adhesive mechanism, and the measured adhesive strength is much smaller than the calculated value for parallel-contacting core-shell cylinders but larger than the calculated value for perpendicular-contacting core-shell cylinders.

REFERENCE

1. P. Wang, Y. Ju, Y. Cui, and A. Hosoi. Copper/parylene core/shell nanowire surface fastener used for room-temperature electrical bonding. *Langmuir* **2013**, *29*, 13909-13916.
2. R. L. Fleisher, P. B. Price, and R. M. Walker. *Nuclear Tracks in Solids: principles*

Chapter 3. Copper-parylene core-shell NSF

- and applications*, Berkeley University of California Press, **1975**, 23-25.
3. G. Cao and D. Liu. Template-based synthesis of nanorod, nanowire, and nanotube arrays. *Adv. Colloid Interface* **2008**, *136*, 45-64.
 4. B. Ye. Fabrication and Magnetic Property Investigation of Metallic Nanowire Arrays. Doctor Thesis, University of New Orleans **2006**.
 5. P. L. Taberna, S. Mitra, P. Poizot, P. Simon, and J. M. Tarascon. High rate capabilities Fe₃O₄-based Cu nano-architected electrodes for lithium-ion applications. *Nature Mater.* **2006**, *5*, 567-573.
 6. J. -C. Puipe, F. Leaman. *Theory and Practice of Pulse Plating*, American Electroplaters and Surface Finishers Society, Orland, FL, **1986**, 55-58.
 7. M. E. T. Molaes, et al.. Single-crystalline copper nanowire produced by electrochemical deposition in polymeric ion track membranes. *Adv. Mater.* **2001**, *13*, 62-65.
 8. P. Wang, Y. Ju, A. Hosoi, and Y. Song. Room temperature electrical bonding technique based on tilted copper nanowire fastener with anisotropic adhesive properties. Proc. IEEE Nano 2012 Conf. **2012**, 1-4.
 9. Q. P. Nguyen. Characterization of biocompatible parylene-C coatings for biomems applications. Master thesis, Louisiana State University **2007**, 4-8.
 10. Parylene Knowledge. <http://www.scscoating.com/parylene_knowledge/index.aspx>
 11. A. Kahouli, et al.. Dielectric properties of parylene AF4 as low-*k* material for microelectronic applications. *Thin solid films* **2012**, *520*, 2493-2497.

Chapter 3. Copper-parylene core-shell NSF

12. Parylene Conformal Coating Specifications & Properties.
<<http://www.scscookson.com/parylene/properties.cfm>>
13. J. M. Elizondo-Decanini and E. Dudley. Pulsed high-voltage breakdown of thin-film parylene C. *IEEE Trans. Plasma Sci.* **2011**, *39*, 3162-3167.
14. A. Kahouli. Effect of film thickness on structural, morphology, dielectric and electrical properties of parylene C films. *J. Appl. Phys.* **2012**, *112*, 064103.
15. R. Kapadia, et al.. Hybrid core-multishell nanowire forests for electrical connector applications. *Appl. Phys. Lett.* **2010**, *94*, 263110.
16. H. Ko, et al.. Hybrid core-shell nanowire forests as self-selective chemical connectors. *Nano Lett.* **2009**, *9*, 2054-2058.
17. J. N. Israelachvili, *Intermolecular and surface forces*, Academic press, San Diego, **1991**, 253-290.
18. R. Tadmor. The London-van der Waals interaction energy between objects of various geometries. *J. Phys.: Condens. Matter.* **2001**, *13*, 195-202.
19. D. Leckband and J. Israelachvili. Intermolecular forces in biology. *Q. Rev. Biophys.* **2001**, *34*, 105-267.
20. J. Visser. On Hamaker constant: a comparison between hamaker constants and lifshitz-van der Waals constants. *Adv. Colloid Interface Sci.* **1972**, *3*, 331-363.
21. Y. F. Mo, K. T. Turner and I. Szlufarska. Friction laws at the nanoscale. *Nature* **2009**, *457*, 1116-1119.

Chapter 3. Copper-parylene core-shell NSF

22. T. Goda, T. Konno, M. Takai, and K. Ishihara. Photoinduced phospholipid polymer grafting on parylene film: advanced lubrication and antibiofouling properties. *Colloids Surf., B.* **2007**, *54*, 67-73.
23. S. Kim, M. Sitti, C. Y. Hui, R. Long, and A. Jagota. Effect of backing layer thickness on adhesive of single-level elastomer fiber arrays. *Appl. Phys. Lett.* **2007**, *91*, 221913.
24. T. Osborn, A. He, N. Galiba, and P. Kohl. All-copper chip-to-substrate interconnects part I. fabrication and characterization. *J. Electrochem. Soc.* **2008**, *155*, 308-313.
25. J. B. Fortin and T. -M. Lu. Chemical Vapor Deposition Polymerization: The Growth and Properties of Parylene Thin Films, Kluwer Academic, Norwell, MA **2004**, 57-76.

4. Copper-polystyrene Core-shell Nanowire Surface Fastener

4.1 Introduction

In chapter 3, a room-temperature electrical surface fastener consisting of copper-parylene core-shell nanowire arrays was presented. It has been found that the conformal parylene coating could improve adhesive strength dramatically. However, the parylene coating process need a special coating system [1] and the coating process is very slow. On the other hand, it was found that some polymer such as polystyrene (PS) can be simply fabricated through bringing porous templates into contact with polymer solution or melts [2]. Based on the peculiar template-assisted electrodeposition method in chapter 3, it is easy to electrodeposit copper nanowire into polymer nanotube and then core-shell nanostructure could be obtained. Moreover, polystyrene shows viscosity after the treatment of volatile toluene solution and then it can be used to increase the adhesive strength of nanowire surface fasteners. Hence, a new kind of core-shell electrical nanowire surface fastener which consists of copper core and polystyrene shell was presented in this chapter. This copper-polystyrene core-shell nanowire surface fastener exhibits high macroscopic adhesive strength ($\sim 47.04 \text{ N/cm}^2$) and low electrical resistance ($\sim 0.78 \times 10^{-2} \Omega \cdot \text{cm}^2$). According to the experiment results, it seems that the conductive mechanism of thin parylene film shown in chapter 3 can also be applied to polystyrene, which means that the dielectric breakdown leads to the electrical conductivity of polystyrene film in nanoscale thickness.

4.2 Polystyrene chemical bonding

For thermoplastic polymers, they will become moldable when the heating temperature is above a specific value. They are held by weak intermolecular bonds such as van der Waals or hydrogen bonds [3]. Thermoplastics are heat softenable, heat meltable and reprocessable [4]. The most important advantages of thermoplastics over thermosets are their high impact strength and fracture resistance which in turn imparts excellent damage tolerance characteristics to the composite material [5].

One typical thermoplastic polymer is polystyrene. Polystyrene is a vinyl polymer made from the monomer styrene through vinyl polymerization. The commonly used polystyrene is transparent, stiff and brittle. However, it can also be foamed. Its price is really cheap. Moreover, it has relatively low melting temperature and it cannot keep off the oxygen and water vapor [6]. Polystyrene is one of the most widely used plastics, and its production has been up to several billion kilograms per year [7]. The natural polystyrene is transparent but it can have different colors with the help of colorants.

Liquid solvents will readily bond polystyrene parts. Methylene chloride, methyl ethyl and toluene are effective for polystyrene bonding. Compared with methylene chloride and methyl ethyl, toluene has the least side effect to the health of human. Hence, toluene was chose to bond polystyrene in this study. **Fig. 4-1** shows the schematic of polystyrene bonding. One drop of solution (20 μ l toluene solution) was directly loaded on the polystyrene plate, which will make the polystyrene show viscosity. Then two samples of toluene-treated polystyrene plate were connected each other under a preload of 9.8 N. After waiting for several minutes, strong bonding was obtained. As shown in **Fig. 4-2**, the bonded polystyrene plate could afford a weight of 1 kg in the shear direction without failure.

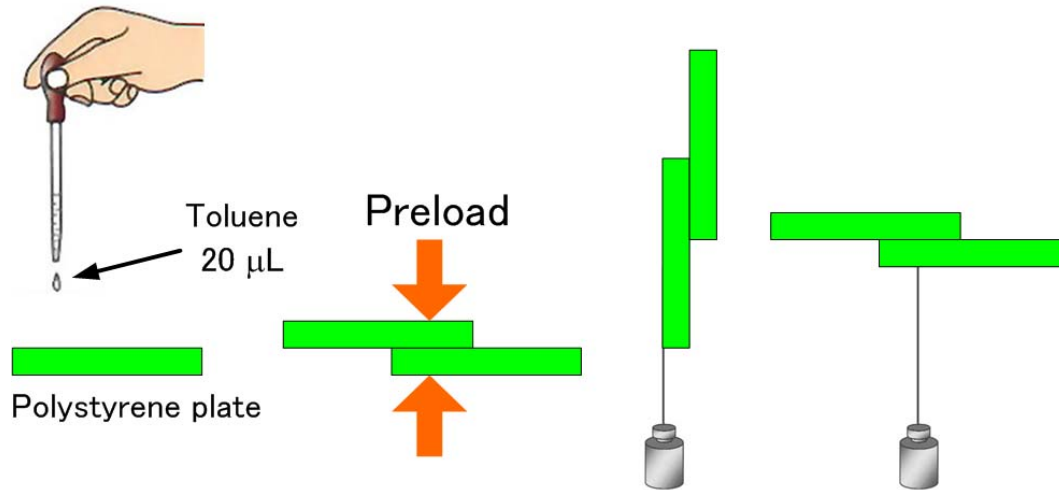


Fig. 4-1 Schematic of polystyrene bonding.



Fig 4-2 Photo of polystyrene bonding.

4.3 Template wetting method

Recently, the fabrication and the application of polymer nanotubes (PNTs) have

Chapter 4. Copper-polystyrene Core-shell NSF

received more and more attention because they are very important for fundamental studies [8, 9] as well as practical applications in biochips, biosensors, and bioseparations [10]. Many methods can be used to fabricate polymer nanotubes, such as sol–gel processes [11], self-assembly processes [12], direct polymerization [13, 14], and template wetting [15, 16]. Among these methods, template wetting has been found to be a volatile and technically simple process for the preparation of nanotubes. Polystyrene [17], polymethyl methacrylate (PMMA) [18], polyamide 66 [19] et al. can form nanotube structure through this method. Polystyrene was first used to fabricate nanotube structure by Steinhart et al. [2]. They suggested that the morphology of polystyrene nanotube can be adjusted by controlling primary solution parameters such as polymer molecular weight, concentration and solvent properties [16, 20]. In the traditional template wetting method, nanotube structure could be obtained through simply bring the porous template into contact with polymer solutions or melts. Although this method is quite easy, some limitations exist for obtaining open-ended through-hole polymer nanotubes. Although the residual polymer layer on the surface of porous template could be removed by mechanical polishing [19], the structure of nanotube tends to be destroyed at the same time. Recently, a new fabrication method for open-ended through-hole polymer nanotubes of controllable thickness was developed through combing template wetting method with the spin-casting method [21]. Moreover, multi-layer nanotubes made of polystyrene, PMMA and PS-PMMA copolymer can be prepared through this method.

4.4 Copper-polystyrene core-shell nanowire array

The fabrication procedure of the copper-polystyrene core-shell nanowire array is outlined in **Fig. 4-3**. At first, surface modification which will be described in details

Chapter 4. Copper-polystyrene Core-shell NSF

later was carried out to improve the adhesive strength between the Au film and the copper nanowire to be electrodeposited. Second, open-ended through-hole polystyrene nanotube array was fabricated into the AAO template through spin-casting method. Third, copper nanowires were fabricated into polystyrene nanotubes through template-assisted electrodeposition method. Finally, after selectively etching the AAO template in NaOH solution, freestanding copper-polystyrene core-shell nanowire array on the Au/Cr/glass substrate was obtained.

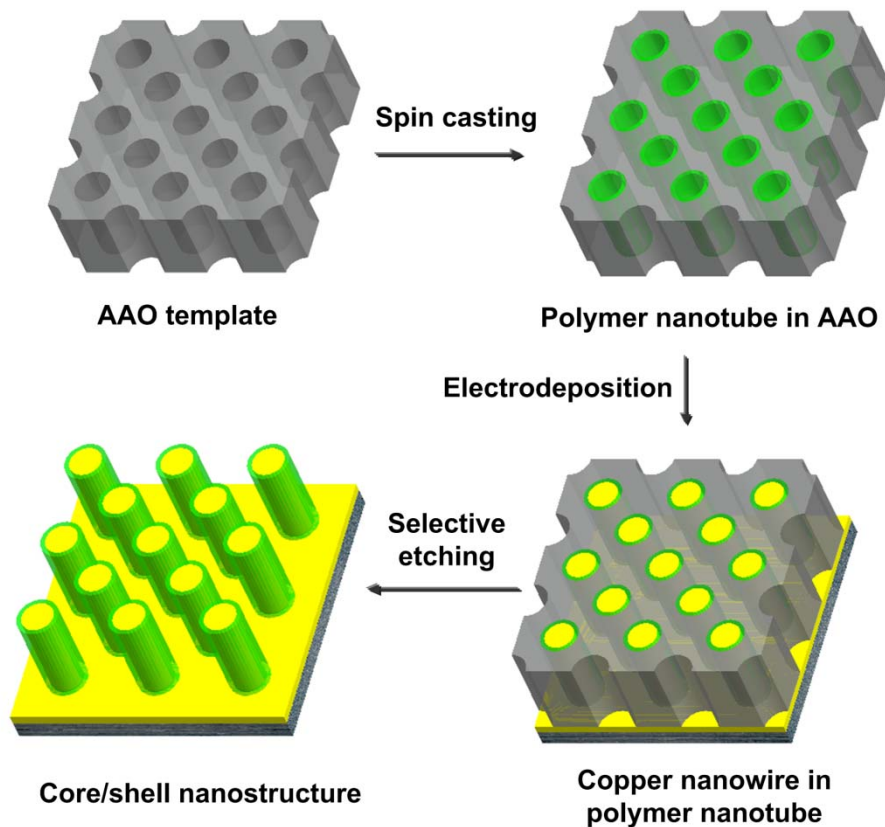


Fig. 4-3 Schematic of copper-polystyrene core-shell nanowire array.

Through electrodepositing copper nanowire into polystyrene nanotube, an innovative method to fabricate core-shell nanowire structure was presented here. Moreover, this is a versatile and technically simple method. Because template wetting

Chapter 4. Copper-polystyrene Core-shell NSF

method can be used to fabricate various nanotubes (such as PS, PMMA, PS-PMMA block copolymer and silica) and template-assisted electrodeposition method can be used to fabricate various metal nanowires (such as Cu, Au, Fe, Ni and Ag), this method combined the template wetting method with template-assisted electrodeposition method and then has the potential to fabricate a various kind of core-shell nanowire structures. Hence, this method may be able to be applied into many research areas, such bonding technique, battery electrode, and so on.

4.4.1 Anodize alumina oxide template

In this study, Synkera anodized alumina oxide (AAO) membranes with a nominal pore diameter of 80 nm were utilized as templates. These membranes had a thickness of 50 μm and a interpore distance of 240 nm.

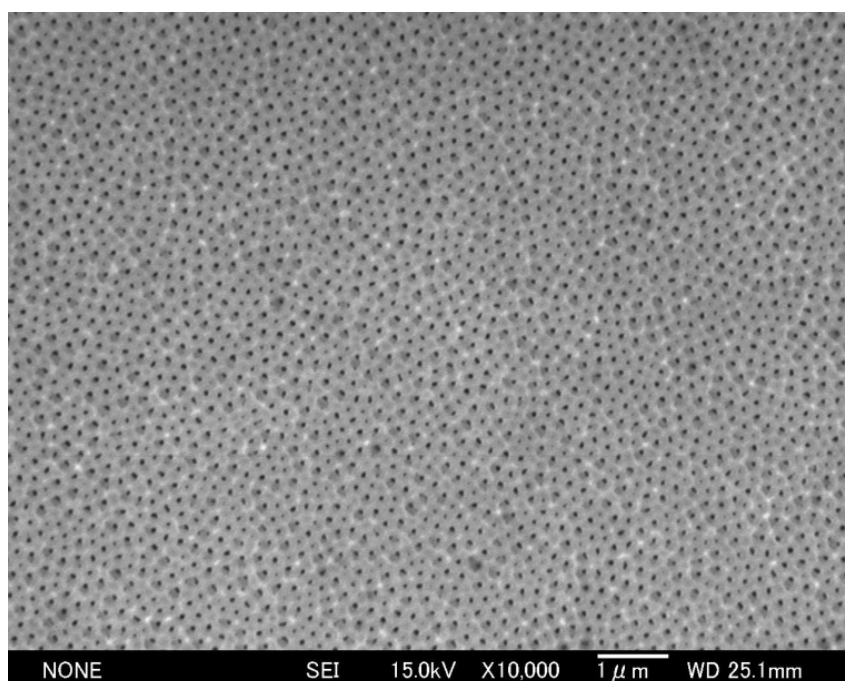


Fig. 4-4 SEM image of one surface of Synkera template.

4.4.2 Surface modification of the substrate

In the chapter 3 it has been found that the adhesive strength between the electrodeposited copper nanowire and the Au film has become the limiting factor of copper-parylene core-shell nanowire surface fastener. In order to improve the adhesive strength, one simple method is to change the Au film to be Cu film. However, neither Cu/Ta/glass nor Cu/Ta/silicon substrate made by electron beam (EB) evaporation could withstand the corrosion of copper sulfate electrolyte during the two immersion processes. Another method is to improve the adhesive strength between Au film and copper nanowire through surface modification. This method was inspired by the excellent adhesive capability of mussels. Through secreting adhesive proteins, mussels could attach to all types of inorganic and organic surfaces [22], including classically adhesive-resistant materials such as polytetrafluoroethylene (PTFE). Through deeply studying the adhesive mechanism of mussel, Messersmith et al. invented a volatile and technically simple method named polydopamine coating for multifunctional surface modification [23]. Moreover, polydopamine coating shows metal-binding ability [24] so that it has good adhesive properties with the metal. In this study, polydopamine was chose to be interlayer to improve the adhesive strength between the Au film and the electrodeposited copper nanowire. The polydopamine coating was prepared following a similar method reported in the literature of Ref. [23]. Briefly, dopamine (2g/L) was dissolved in 10 mM Tris-Hcl. Then the solution was adjusted to PH 8.5 with diluted hydrochloric acid immediately. The polydopamine coating will be carried out through simply dipping the substrate into the solution. Through controlling the dipping time, the corresponding thickness of polydopamine film was obtained. In this study, the dipping time is one hour and then the thickness of polydopamine film will be smaller than 5 nm [23]. Because the thickness of

polydopamine film is too small, it is easy to understand that the dielectric breakdown will lead to electrical conductivity of polydopamine film which is similar with the parylene film [25] as described in chapter 3.

4.4.3 The formation of PS nanotube in AAO template

In this study, the PS nanotube array was prepared following a similar method reported in the literature of Ref. [21]. As can be seen in the **Fig. 4-5**, AAO template was firstly fixed on a circular glass substrate with the help of nail polish. The glass gasket was used to let the two sides of AAO template suspended in the midair.

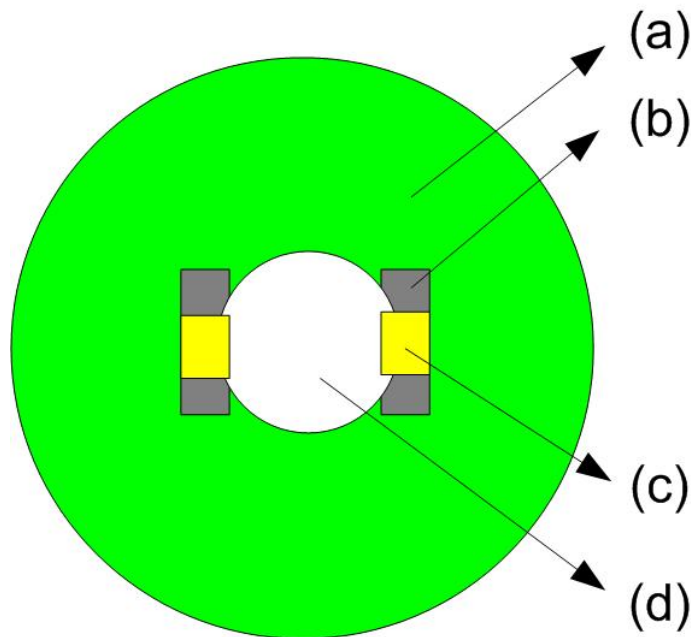


Fig. 4-5 The device used to fix the AAO template: (a) glass substrate, (b) glass gasket, (c) nail polish, (d) AAO template.

In our experiment, nail polish shows better performance than double-sided adhesive tape because it is very easy to be removed through acetone etching. Second, one drop of solution (20 μl of 2.5 wt% PS solution in toluene) was directly loaded on the spinning AAO template. That drop will immediately and completely fill the AAO

Chapter 4. Copper-polystyrene Core-shell NSF

nanoholes by wetting and capillary forces. The PS nanotube array could be formed after spinning at 3000 rpm for 90 s. Finally, the thickness of PS nanotube can be controlled through adjusting the loaded times of PS solution.

Fig. 4-6 shows the SEM image of PS nanotube arrays after removing the AAO template. Because of the low Young's modulus of the PS (3-3.5 GPa), the fabricated PS nanotubes tended to fall down and then bundle together. Hence, the electrodeposition of copper nanowire into polystyrene nanotube has two functions: (1) The copper offers the electrical connection for the nanowire fastener. (2) The copper nanowire will support the polystyrene nanotube so that the polystyrene nanotube will not fall down.

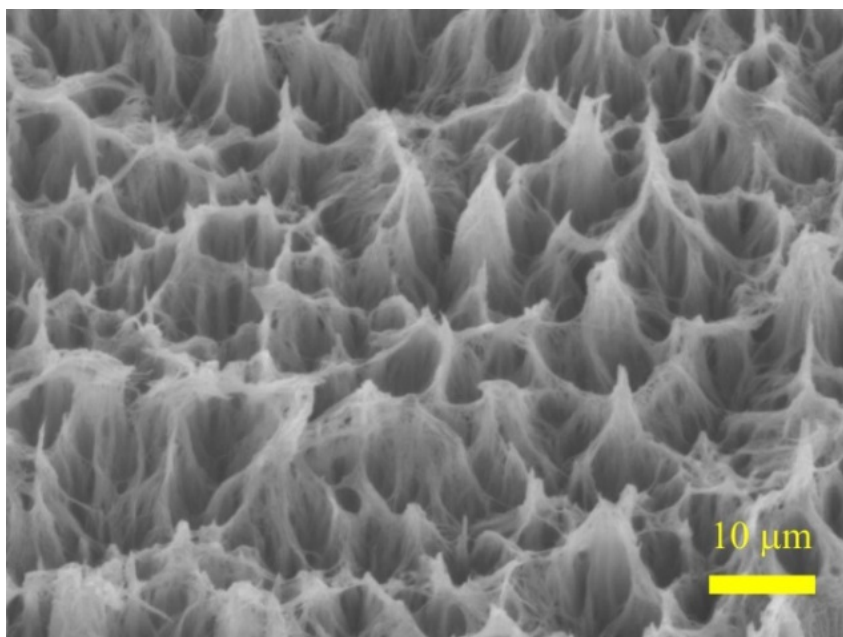


Fig. 4-6 SEM image of PS nanotube array.

4.4.4 Electrodeposition of Cu nanowires

The copper nanowire array was fabricated following a similar method reported in the chapter 3. Briefly, template was fixed right above the fabrication areas by the

Chapter 4. Copper-polystyrene Core-shell NSF

insulation holders. The electrodeposition electrolyte used was a 0.4 M $\text{CuSO}_4 \cdot 5\text{H}_2\text{O}$ solution, adjusted at pH=2 with sulfuric acid. A peculiar cell and two additional immersion method described in **Fig. 3-6** were used to guarantee the uniform growth of copper nanowire array. The only difference with the previous cell in **Fig. 3-6** is the template. After selectively etching the AAO template in 2M NaOH solution, freestanding copper-polystyrene core-shell nanowire array on the Au/Cr/glass substrate was obtained.

4.5 SEM image of copper-polystyrene core-shell nanowire

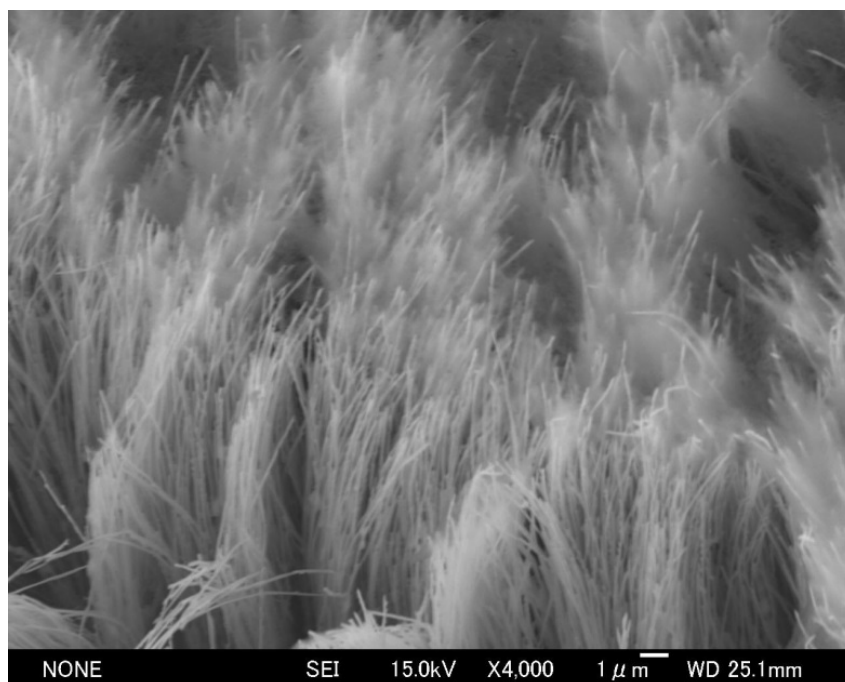


Fig. 4-7 SEM image of copper-polystyrene core-shell nanowires in the small magnification.

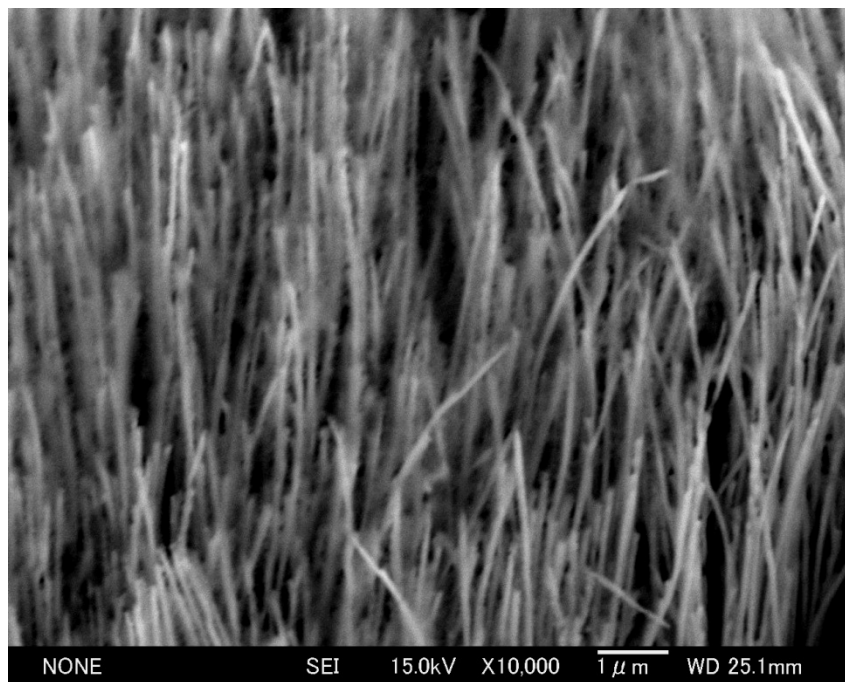


Fig. 4-8 SEM image of copper-polystyrene core-shell nanowires in the large magnification.

As shown in **Fig. 4-7** and **4-8**, SEM observation indicated that most of the copper-polystyrene core-shell nanowires grew vertically on the fasten area and the length of nanowire array was uniform in most areas. The thickness of polystyrene shell is around 18 nm.

4.6 Adhesive strength measurement

The exceptional adhesive performance for the copper-polystyrene core-shell nanowire surface fastener is determined below. **Fig. 4-9** shows a weight of (a) 600 g in shear direction or (b) 300 g in normal direction being held by a thin wire that was pre-glued on the back side of a glass substrate with the as grown copper-polystyrene core-shell nanowire arrays interconnected with each other.

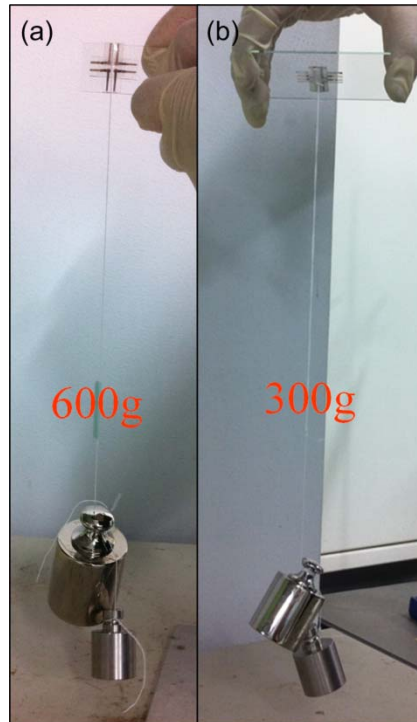


Fig. 4-9 A weight of (a) 600 g in shear direction or (b) 300 g in normal direction is suspended by the use of copper-polystyrene core-shell NSFs.

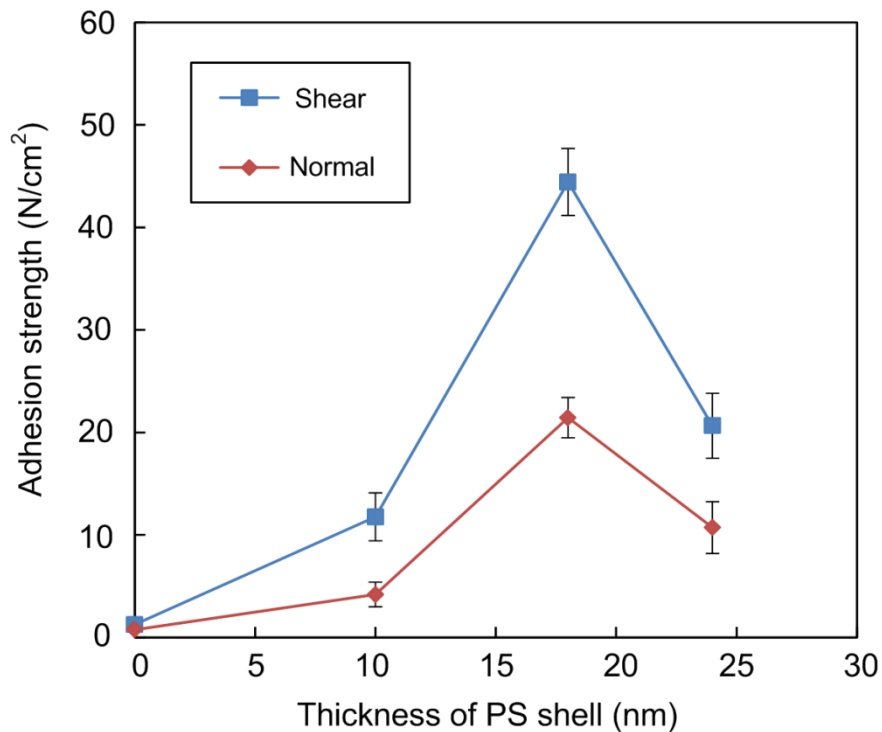


Fig. 4-10 Adhesive strength of NSFs as a function of thickness of PS shell in the spin-casting process. The preload is 9.8 N.

Chapter 4. Copper-polystyrene Core-shell NSF

As can be seen in the **Fig. 4-10**, the adhesive properties strongly depended on the thickness of the polystyrene shell. Specifically, weak adhesive strength ($\sim 1.18 \text{ N/cm}^2$ in shear and $\sim 0.78 \text{ N/cm}^2$ in normal directions) are obtained from pristine copper nanowires. When the thickness of PS shell is $\sim 18 \text{ nm}$, the maximum adhesive strength ($\sim 47.04 \text{ N/cm}^2$ in shear and $\sim 23.52 \text{ N/cm}^2$ in normal directions) are obtained. This significant enhancement in adhesive is attributed to the dispersion forces of polystyrene bonding. As it is known to all, both polystyrene and toluene are whole non-polar molecules. Non-polar molecules will dissolve in other non-polar molecules due to the existence of dispersion forces. After the polystyrene dissolved in the toluene, the solution will show viscosity. Fox et al. [26] has found that larger molecule weight leads to larger viscosity. When the molecule weight of polystyrene is higher than 100000 g/mol , the viscosity is so high that it can serve as an adhesive. Moreover, the toluene is a volatile solution. During the volatilization process of toluene, the polystyrene which was dissolved in toluene will solidify in the interface again. The recrystallization process during the solidification of polystyrene will also increase the adhesive strength of interconnected polystyrene. When the thickness of the polystyrene shell further increases, the adhesive strengths decrease. This trend may be attributed to the higher filling factor, which has been given a detailed discussion in chapter 3.

4.7 Electrical resistance measurement

The I - V curves of room-temperature bonding based on copper-polystyrene core-shell NSF under a preload of 9.8 N are presented in **Fig. 4-11**. In order to remove the contingency, the electrical resistance measurement was performed at three times. The average electrical resistance is $0.247 \text{ } \Omega$. After the normalization by the contact

area, the electrical resistance is $0.78 \times 10^{-2} \Omega \cdot \text{cm}^2$.

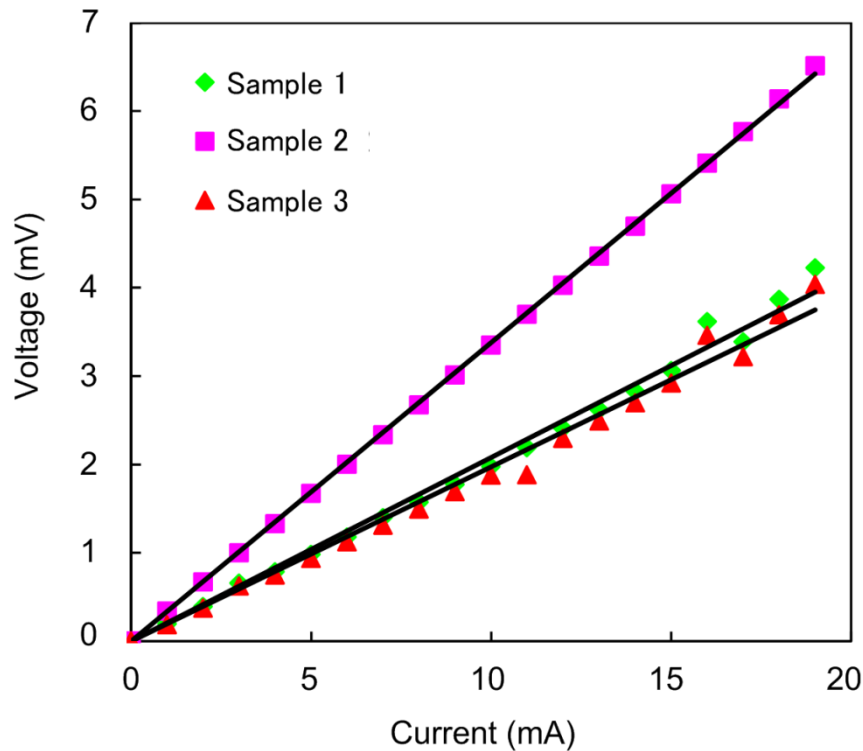


Fig. 4-11 Measured I - V curves of the bonding for three times. The preload is 9.8 N.

The thickness of PS shell is ~ 18 nm.

4.8 Summary

In summary, a new kind of surface nanowire fastener based on copper-polystyrene core-shell nanowire array has been presented through which electrical and mechanical bonding can be realized at room temperature. Electrical measurement indicated that the electrical resistance of the interconnected nanowire array on the fastener is around $0.78 \times 10^{-2} \Omega \cdot \text{cm}^2$ under the preload of about 9.8 N. The maximum bonding strength of $\sim 23.52 \text{ N/cm}^2$ (in normal direction) and $\sim 47.04 \text{ N/cm}^2$ (in shear direction) were obtained. Therefore, this kind of copper-polystyrene core-shell nanowire fastener is hopeful to be used as electrical and mechanical room-temperature bonding in the surface mount.

Chapter 4. Copper-polystyrene Core-shell NSF

REFERENCE

1. Parylene Knowledge. <http://www.scscoating.com/parylene_knowledge/index.aspx>
2. M. Steinhart, et al.. Polymer nanotubes by wetting of ordered porous templates. *Science* **2002**, *296*, 1997-1997.
3. E. A. Muccio. *Plastics Processing Technology*, ASM International, U.S.A., **1994**, 32-36.
4. G. Akovali. *Handbook of Composite Fabrication*, Rapra Technology Ltd., United Kingdom, **2001**, 143-150.
5. M. M. Schwartz. *Composite Materials, Volume II: Processing, Fabrication and Applications*, Society of Manufacturing Engineers Publications, New Jersey, **1989**, 1-592.
6. J. R. Wunsch. *Polystyrene: Synthesis, Production and Applications*, iSmithers Rapra Publishing, **2000**, 28-31.
7. J. Maul, et al.. *Polystyrene and Styrene Copolymers*, Ullmann's Encyclopedia of Industrial Chemistry, Wiley-VCH, Weinheim, **2007**, 1-15.
8. K. Shin, et al.. Curving and frustrating flatland. *Science* **2004**, *306*, 76-76.
9. Y. Sun, et al.. Diameter-dependence of the morphology of PS-b-PMMA nanorods confined within ordered porous alumina templates. *Macromol. Rapid Commun.* **2005**, *26*, 369-375.
10. C. R. Martin and P. Kohli. The emerging field of nanotube biotechnology. *Nat. Rev. Drug Discovery* **2003**, *2*, 29-37.

Chapter 4. Copper-polystyrene Core-shell NSF

11. R. Gasparac, P. Kohli, M. O. Mota, L. Trofin and C. R. Martin. Template synthesis of nano test tubes. *Nano Lett.* **2004**, *4*, 513-516.
12. T. Shimizu, M. Masuda and H. Minamikawa. Supramolecular nanotube architectures based on amphiphilic molecules. *Chem. Rev.* **2005**, *105*, 1401-1444.
13. K. J. Lee, J. H. Oh, Y. Kim and J. Jang. Fabrication of photoluminescent-dye embedded poly(methyl methacrylate) nanofibers and their fluorescence resonance energy transfer properties. *Adv. Mater.* **2006**, *18*, 2216-2219.
14. K. Y. Choi, J. J. Han, B. He, and S. B. Lee. Syndiotactic polystyrene nanofibrils in silica nanotube reactors: understanding of synthesis with ultrahigh molecular weight. *J. Am. Chem. Soc.* **2008**, *130*, 3920-3926.
15. M. Zhang, P. Dobriyal, J. -T. Chen, and T. P. Russel. Wetting Transition in Cylindrical Alumina Nanopores with Polymer Melts. *Nano Lett.* **2006**, *6*, 1075-1079.
16. M. Steinhart, R. B. Wehrspohn, U. Gösele, and J. H. Wendorff. Nanotubes by template wetting: a modular assembly system. *Angew. Chem., Int. Ed.* **2004**, *43*, 1334-1344.
17. M. Pasquali, J. Liang, and S. Shivkumar. Role of AAO template filling process parameters in controlling the structure of one-dimensional polymer nanoparticle. *Nanotechnology* **2011**, *22*, 375605.
18. G. Chen, S. A. Soper, and R. L. McCarley. Free-standing, erect ultrahigh-aspect-ratio polymer nanopillar and nanotube ensembles. *Langmuir* **2007**, *23*, 11777-11781.

Chapter 4. Copper-polystyrene Core-shell NSF

19. X. She, G. Song, J. Li, P. Han, S. Yang, and Z. Peng. Preparation and characterization of polyamide 66 nanotubes and nanowires on an anodic aluminum oxide template by a physical wetting method. *J. Mater. Res.* **2006**, *21*, 1209-1214.
20. S. Schlitt, A. Greiner, and J. H. Wendorff. Cylinder polymer nanostructures by solution template wetting. *Macromolecules* **2008**, *41*, 3228-3234.
21. S. Jin, et al.. Simple fabrication of single- and multi-layer polymer nanotubes by spin-casting method within anodized aluminum oxide (AAO) templates. *J. Mater. Chem.* **2012**, *22*, 23368-23373.
22. H. Lee, N. F. Scherer, and P. B. Messersmith. Single-molecule mechanics of mussel adhesive. *Proc. Natl. Acad. Sci. USA* **2006**, *103*, 12999-13003.
23. H. Lee, S. M. Dellatore, W. M. Miller, P. B. Messersmith. Mussel-inspired surface chemistry for multifunctional coatings. *Science* **2007**, *318*, 426-430.
24. K. D. Karlin, C. G. Pierpont, C. W. Lange. The chemistry of transition metal complex containing catechol and semiquinone ligands. *Prog. Inorg. Chem.* **2007**, *41*, 331-442.
25. P. Wang, Y. Ju, Y. Cui, and A. Hosoi. Copper/parylene core/shell nanowire surface fastener used for room-temperature electrical bonding. *Langmuir* **2013**, *29*, 13909-13916.
26. T. G. Fox JR and P. J. Flory. Viscosity-Molecular Weight and Viscosity-Temperature Relationships for Polystyrene and Polyisobutylene. *J. Am. Chem. Soc.* **1948**, *70*, 2384-2395.

5. Conclusions

(a) To avoid the problems aroused by the high heating temperature in microelectronics, we proposed a novel room-temperature technique based on the freestanding nanowire array on the substrate which was named nanowire surface fastener. This room-temperature bonding technique was realized by pressing two nanowire arrays against each other. The van der Waals forces between the interconnected nanowires contributed to the room-temperature bonding which exhibited good mechanical and electrical properties.

(b) In the past, it is difficult to fabricate freestanding nanowire array on the substrate directly through template-assisted electrodeposition method. Traditionally, a thin conductive metallic layer was deposited on one side of the template through sputter or electron-beam evaporation, which is difficult to get free-standing nanowire array after the AAO template is fully removed. In this study, two additional immersion methods were introduced so that freestanding copper nanowire array can be fabricated on the substrate directly with the help of AAO template. Although the two additional immersions were quite easy, these innovative processes were shown to be crucial in the experimental process. This novel process was verified of importance and significance by studying the results of SEM and TEM images on samples. SEM observation indicated that a copper nanowire array grew in the entire fastener area and the length of the nanowire array was uniform in most areas.

(c) Through introducing two additional immersion methods, we developed a room-temperature bonding technique based on copper nanowire surface fastener which showed a macroscopic adhesive strength of 8.17 N/cm^2 and an electrical resistance of $0.69 \times 10^{-2} \Omega \cdot \text{cm}^2$. Furthermore, through observing the SEM images of

Chapter 5. Conclusions

interconnection interface, the upper and lower nanowire arrays were found to be interconnected at an arbitrary angle. Hence, two extreme conditions (parallel-contacting mode and perpendicular-contacting mode) were considered in the theory analysis, which showed that much higher adhesive strength can be obtained if most copper nanowires could interconnect with each other. In addition, the adhesive strength and electrical resistance of the copper nanowire surface fastener in the perfect states were predicted. The predicted values show that the nanowire surface fastener has the possibility to replace the traditional solders.

(d) Anisotropic adhesive properties could be obtained from tilted copper nanowire fastener. Tilted copper nanowire array was obtained through applying directional shear force onto the freestanding copper nanowire array from AAO template. In terms of pressing the straight copper nanowire array against the tilted array, the electrical bonding was achieved. This bonding technique shows good electrical conductivity ($\sim 0.94 \times 10^{-2} \Omega \cdot \text{cm}^2$). Moreover, anisotropic adhesive properties were obtained, and the shear adhesive strengths were 9.36 and 1.56 N/cm^2 , respectively, for the two opposite directions that are parallel and antiparallel to the tilted direction of the nanowires.

(e) A porous glass plate and a cellulosic paper was introduced to achieve the uniform contact between the flexible polycarbonate membrane and the substrate. The stiffness of the porous glass plate ensured the contact of the substrate with polycarbonate membrane. Moreover, the compliance of cellulose paper offered a buffer and then ensured tight contact of the substrate with the polycarbonate membrane. Then, flexible polycarbonate membrane could also be used as the template for growing nanowire array. With the help of this new cell and polycarbonate

Chapter 5. Conclusions

template, freestanding copper nanowire array can be fabricated on the substrate directly.

(f) Interestingly, the parylene-C film becomes conductive due to dielectric breakdown when the thickness of it is miniaturized to nanoscale. Based on this phenomenon, a room-temperature electrical surface fastener consists of copper-parylene core-shell nanowire arrays were demonstrated. The copper nanowire array was electrodeposited on the substrate directly with the help of polycarbonate template, which provided the electrical conductive function. The parylene shell was deposited on Cu nanowire array through CVD method, which provided surface compliance to increase contact areas, thereby realizing larger bonding strength. Through pressing core-shell nanowire arrays against each other, the van der Waals forces between the interpenetrating nanowires had a contribution to the room temperature bonding. Uniquely, this electrical surface fastener exhibits high macroscopic adhesive strength ($\sim 25 \text{ N/cm}^2$) and low electrical resistance ($\sim 4.22 \times 10^{-2} \Omega \cdot \text{cm}^2$). Until now, the expressions for the van der Waals forces between two core-shell cylinders are not available. Based on the assumption of additivity, the corresponding van der Waals expressions were presented and were proved to be effective.

(g) An innovative fabrication method of core-shell nanowire array was presented. At first, polystyrene nanotube array was fabricated into the AAO template through spin-casting method. Second, copper nanowires were fabricated into polystyrene nanotubes through template-assisted electrodeposition method. Finally, after selectively etching the AAO template in NaOH solution, freestanding copper-polystyrene core-shell nanowire array on the Au/Cr/glass substrate was obtained.

Chapter 5. Conclusions

(h) After the surface treatment of polystyrene shell with toluene, the polystyrene shows viscosity so that the interaction forces between two polystyrene nanoshells could increase dramatically. Based on this phenomenon, a new kind of surface nanowire fastener based on copper-polystyrene core-shell nanowire array was presented. Electrical measurement indicated that the electrical resistance of the interconnected nanowire array on the fastener is around $0.78 \times 10^{-2} \Omega \cdot \text{cm}^2$ under the preload of about 9.8 N. The bonding strength of approximately 23.52 N/cm² (in normal direction) and 47.04 N/cm² (in shear direction) were obtained. Therefore, this kind of copper-polystyrene core-shell nanowire based fastener is hopeful to be used as electrical and mechanical room-temperature bonding in microelectronics.

Acknowledgements

I would first and foremost like to express my sincere gratitude to my supervisor, Professor Yang Ju, for his tireless supports, encouragement and inspiration through my study. Luckily as his PhD student in Nagoya University, I have got the chance to study abroad and experience the growth of Ju group. He nurtures me not only a research spirit of approaching intriguing scientific problems and demanding technical challenges, but also gives me many great opportunities to expose myself into the real scientific and engineering communities through a variety of conferences and symposiums, presenting my research, talking with my peers and learning from the authorities. When I continue my research career in China, he is my role model who taught me the invaluable character of humility, diligence, modesty, perseverance and prudence.

I want to say thanks to Professor Nobutada Ohno for his irreplaceable suggestions, say thanks to Associate Professor Tadashige Ikeda for his incomparable kindness.

I want to give my heartily thanks to Associate Professor Yasuyuki Morita. His willingness, knowledge and expertise are instrumental in helping me finishing my experiment and graduation. I further extend my appreciations to Assistant Professor Atsushi Hosoi for his warm help. For many times of my experiment, he has been supporting me with his accompanying and encourage.

I give my deeply grateful thanks to my best partners and friends, Dr. Baiyao Xu,

Acknowledgements

Dr. Yanbin Cui, Dr. Yuanhui Song, Mr. Yongpeng Tang, and Mr. Lijiao Hu. When I met difficulties in my research or in my daily life, they have been always living together with me with encourage and accompanying. We have built a precious friendship.

I would like to thank Mr. Masahiro Amano, Ms. Yuka Iwasaki, Mr. Hiromasa Teshima, Mr. Kazuma Ichioka, Mr. Keita Uchida and Mr. Kohei Kojima for their help and cooperation. I would like to thank all the members of Ju Lab.

Many thanks also give to those who have contribution to this study.

I would like to acknowledge Chinese Scholarship Council (CSC) for supporting my research and daily life in Japan.

Lastly, I would like to thank my parents, for their endless love, encouragement and understanding throughout the period of my PhD study.

Peng Wang

Nagoya Univeristy

November, 2013